REPORT DOCUMENTATION PAGE

AFRL-SR-AR-TR-02-

0321

1. REPORT DATE (DD-MM-YYYY)	2. REPORT TYPE	3. DATES COVERED (From - To)
09/03/02	Final Technical	10/01/98 - 03/31/02

4. TITLE AND SUBTITLE
The Effectiveness of Actuators Used in Active Flow Controls:
Numerical Simulations, Analysis and Experiments

5a. CONTRACT NUMBER

5b. GRANT NUMBER
F49620-99-1-0015

5c. PROGRAM ELEMENT NUMBER

6. AUTHOR(S)
Dr. Hermann Fasel and Dr. Israel J. Wygnanksi (University of Arizona)
Dr. Michael Gaster (Queen Mary and Westfield College – London, UK

5d. PROJECT NUMBER

5e. TASK NUMBER

5f. WORK UNIT NUMBER

7. PERFORMING ORGANIZATION NAME(S) AND ADDRESS(ES)

Department of Aerospace and   Tucson, AZ 85721
Mechanical Engineering
The College of Engineering
and Mines
The University of Arizona

8. PERFORMING ORGANIZATION REPORT NUMBER

9. SPONSORING / MONITORING AGENCY NAME(S) AND ADDRESS(ES)
AFOSR/NA
801 N. Randolph St, Suite 732
Arlington, VA 22203-1977

10. SPONSOR/MONITOR'S ACRONYM(S)

11. SPONSOR/MONITOR'S REPORT NUMBER(S)

12. DISTRIBUTION / AVAILABILITY STATEMENT

Approved for Public Release - Distribution is Unlimite

20021008 011

13. SUPPLEMENTARY NOTES

14. ABSTRACT

Acquiring the ability to effectively modify and control the behavior of fluid flow continues to be a pervasive and important aspiration in many areas of engineering. The present research continues to advance the technology of various schemes that employ the use of wall-mounted actuators for active flow control. Any design in which fluid-flow characteristics are important (aircraft, turbomachinery, ships, etc.) stands to benefit from this new technology of manipulating the flow behavior by time dependent forcing. Research completed to date promises reduced cost, complexity, and weight along with significant improvement in design performance. A summary of this research indicates however, that the details of the disturbance excitation process have still not been completely explored, and hence an understanding of the important parameters in actuator design is currently unavailable to the engineer. Only with this knowledge will it be possible to design devices for specific tasks that are efficient and effective in their performance.

Our program of research examines boundary value periodic point source excitations of laminar boundary layers, and considers how some more complex actuators might be modeled numerically. The study is carried out in three parts: i. linear theory, ii. wind tunnel measurements, iii. full Navier-Stokes modeling.

15. SUBJECT TERMS

16. SECURITY CLASSIFICATION OF:			17. LIMITATION OF ABSTRACT	18. NUMBER OF PAGES	19a. NAME OF RESPONSIBLE PERSON
			UNLIMITED	108	Hermann Fasel
a. REPORT UNCLASSIFIED	b. ABSTRACT UNCLASSIFIED	c. THIS PAGE UNCLASSIFIED			19b. TELEPHONE NUMBER (include area code) (520) 621-2771

THE EFFECTIVENESS OF ACTUATORS USED IN ACTIVE FLOW CONTROL: NUMERICAL SIMULATIONS, ANALYSIS, AND EXPERIMENTS

Final Report

by

Hermann F. Fasel and **Israel J. Wygnanski**

Department of Aerospace and Mechanical Engineering
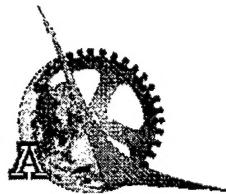
The University of Arizona

Tucson, AZ 85721

Michael Gaster

Department of Engineering

Queen Mary and Westfield College

London, UK

Submitted to

The Air Force Office of Scientific Research

May 2002

2

Abstract

Acquiring the ability to effectively modify and control the behavior of fluid flow continues to be a pervasive and important aspiration in many areas of engineering. The present research continues to advance the technology of various schemes that employ the use of wall-mounted actuators for active flow control. Any design in which fluid-flow characteristics are important (aircraft, turbomachinery, ships, etc.) stands to benefit from this new technology of manipulating the flow behavior by time dependent forcing. Research completed to date promises reduced cost, complexity, and weight along with significant improvement in design performance. A summary of this research indicates however, that the details of the disturbance excitation process have still not been completely explored, and hence an understanding of the important parameters in actuator design is currently unavailable to the engineer. Only with this knowledge will it be possible to design devices for specific tasks that are efficient and effective in their performance.

Our programme of research examines boundary value periodic point source excitations of laminar boundary layers, and considers how some more complex actuators might be modeled numerically. The study is carried out in three parts: i. linear theory, ii. wind tunnel measurements, iii. full Navier-Stokes modeling.

Contents

1 Introduction

Acquiring the ability to effectively modify and control the behavior of fluid flow continues to be a pervasive and important aspiration in many areas of mechanical and aerospace engineering. The present research continues to advance the technology of various schemes that employ the use of wall-mounted actuators for active flow control. Potential applications include the use of periodic injection of momentum (blowing and suction with or without the addition of mass) to delay flow separation from airfoil lifting surfaces, application to diffusers for thrust augmentation and vectoring in high-performance military aircraft, and alleviating the effects of dynamic stall in helicopter rotors that limit flight speeds and maneuverability. Any design in which fluid-flow characteristics are important (aircraft, turbomachinery, ships, rockets, etc.) stands to benefit from this new technology of manipulating the flow behavior by time dependent forcing. Research completed to date promises reduced cost, complexity, and weight along with significant improvement in design performance. A summary of this research indicates however, that the details of the disturbance excitation process have still not been completely explored, and hence an understanding of the important parameters in actuator design is currently unavailable to the engineer. Only with this knowledge will it be possible to design devices for specific tasks that are efficient and effective in their performance.

Our programme of research examines boundary value periodic point source excitations of laminar boundary layers, and considers how some more complex actuators might be modeled numerically. The study is carried out in three parts.

1. Linear theory is used to examine a wide range of boundary layers having different pressure gradients and Reynolds numbers subjected to various periodic point boundary values. The linear model used is relatively cheap and many different flow situations can be explored. The method of analysis is amenable to further simplification where only the asymptotic solutions from various exci-

tations are found from the source receptivities. The receptivities are evaluated for a range of different flow parameters.

2. Wind tunnel measurements have been carried out to validate the linear code so that it can be used to study the responses to excitations over a wide range of parameters. The experimental work is time consuming and it is only sensible to use it to show that the simpler numerical codes give reliable predictions. Here the validation has been made for the case of zero pressure-gradient boundary layers and at only one Reynolds number. It is difficult in the experiment to modify the setup to change the Reynolds numbers significantly and major effort is required to introduce a pressure gradient. There was no reason to suppose that the linear theory, once validated on the zero pressure gradient flow at one Reynolds number, would not be capable of describing the disturbance flow fields in a wide range of different mean flows. The behavior of the flows to large amplitude excitations, that cannot be predicted by a linear model can, of course, also be explored experimentally.

3. Full Navier-Stokes modeling can provide solutions to both linear and nonlinear excitations, but the cost is high. DNS calculations have been carried out to validate the linear code. An immersed boundary technique is introduced for the simulation of flow control actuators which can not be modeled by boundary values alone.

1.1   Theoretical Investigations

Actuators were modeled by various types of boundary values imposed at the wall. Often point excitations have been used in applications and the linear analysis used here studies the resulting flow fields created. The solutions from a point source can be extended to cover other more complex types of excitation. The most popular actuators are oscillating jets aligned in various directions to the boundary wall. Periodic bumps on the surface have also been used and this form of excitation can be modeled by the

linear theory provided that the bump is sufficiently shallow. Other forms of exciters, such as flaps, that have been used in experiments cannot be represented properly by boundary values and are outside the scope of this theory. In the following analysis the usual Cartesian axes x, y, and z are used in the direction of the free-stream, normal to the surface of the plate and in the span wise directions. Mean boundary layer velocities U, V, and W and perturbations u, v, and w are used with the perturbation vorticity components ζ_x, ζ_y, and ζ_z.

1.1.1 Boundary Conditions

It is convenient to apply the velocity boundary conditions on the plane $y = 0$. For the jets this is straightforward, but the shallow bump requires some expansion of the solution close to the boundary.

Unsteady Jets A normal jet at a point can be modeled by making the normal velocity component zero everywhere on the wall except at the excitation point.

$$v(x,0) = v_0\, e^{-i\omega t}\, dx\, dz \tag{1}$$

$$u(x,0) = 0 \tag{2}$$

An angled jet may be represented by

$$v(x,0) = v_0 \cos(\theta) e^{-i\omega t}\, dx\, dz \tag{3}$$

$$u(x,0) = v_0 \sin(\theta) e^{-i\omega t}\, dx\, dz \tag{4}$$

where v_0 is the velocity along the jet pipe aligned at θ to the boundary wall. A similar expression can be written down for a jet aligned in the spanwise direction

Shallow Bumps The required boundary values on the wall can be found by expansion about the wall. The bump geometry is defined by $h(x,z)$, which is assumed to be small and smooth. For shallow bumps therefore we obtain

$$u(x,0) = -\frac{\partial U}{\partial y} h(x,z) e^{-i\omega t} + \mathcal{O}(h^2) \tag{5}$$

$$v(x,0) = -i\omega h(x,z) e^{-i\omega t} + \mathcal{O}(h^2) \tag{6}$$

where $h(x, z)$ can be treated as a point excitation $h_0 \, dx \, dz$. Far from the plate the perturbations decay exponentially in all cases.

1.1.2 Equations of Motion

The linearization of the boundary conditions is one of the approximations used. In this analysis it has also been assumed that the perturbation amplitudes of interest are small enough to allow the disturbances equations to be linearized throughout the flow field. This approach has been established as a good approximation for much of the region of wave growth leading to turbulence, as it is found that only in the last stages of growth do the non-linear terms become important. This approximation seems, therefore, to be especially suitable for the excitation phase of the transition process. Solutions of the linearized perturbation equations of motion subjected to the boundary conditions (1) through (6) are sought. These equations are of partial differential form and their complete solution is likely to be time consuming. In this work solutions close to the source are of most interest and the further approximation is made that the mean flow can be treated as a parallel flow independent of stream wise location. This parallel flow approximation pervades almost all linear stability theory, where it has been found to provide reasonably accurate predictions of the behavior of unstable waves. Although there are schemes for correcting the eigensolutions from the Orr-Sommerfeld equation to account for the slow growth of the boundary layer, these corrections are small and certainly do not alter any understanding of the process of wave growth. Initially at least, the influence of boundary layer growth with downstream distance will be ignored, although at a later stage appropriate corrections could be introduced. With the introduction of these two main approximations, namely linearization and local parallel flow, the perturbation equations separate in the space co-ordinates, enabling Fourier transforms to be taken in the stream wise and spanwise directions. The governing equations are then the Orr-Sommerfeld and Squire equations defining the transform of the velocity perturbations and their deriva-

tives in the directions of the x, y, and z axes. It turned out to be more convenient in this study to re-cast the problem into equations for the three orthogonal velocities and the three vorticity components. The variables in transform space are denoted by the caret symbol ˆ. We obtain the form

$$\hat{u}(\alpha, \beta, \omega, y) = \frac{1}{4\pi^2} \int \int u(x, y, z) e^{i(\alpha x + \beta z - \omega t)} \, dx \, dz \tag{7}$$

etc. for all other variables and their derivatives. The perturbation equations can be reduced to two first order and two second order relationships

$$\hat{u}' = i\alpha\hat{v} - \hat{\zeta}_z \tag{8}$$

$$\hat{v}' = -i\alpha\hat{u} - i\beta\hat{w} \tag{9}$$

$$\hat{\zeta}_z'' = \hat{\zeta}_z p^2 + i\beta\hat{w}R\frac{\partial U}{\partial \eta} - \hat{v}R\frac{\partial^2 U}{\partial \eta^2} \tag{10}$$

$$\hat{\zeta}_y'' = \hat{\zeta}_y p^2 + i\beta\hat{v}R\frac{\partial U}{\partial \eta} \tag{11}$$

where

$$p^2 = \Gamma^2 + i\alpha R \left(U - \frac{\beta}{\alpha} \right) \tag{12}$$

$$\Gamma^2 = \alpha^2 + \beta^2 \tag{13}$$

$$\eta = y\sqrt{\frac{U_\infty}{2\nu x_0}} \tag{14}$$

and the Reynolds number is given by $R = U_\infty \delta^* / \nu$.

This is a sixth-order set of linear ordinary differential equations that can be solved by any number of different schemes. Here it was found convenient to use a shooting method that incorporated a simple way of eliminating the parasitic growth that arises with these *stiff* high Reynolds number equations. The scheme is somewhat similar to that developed by Dr Kaplan some 30 years ago. This form of integration seems particularly suited to the current study involving wall boundary values.

1.1.3 Method of Solution

The equations have six independent solutions, three grow exponentially with the distance from the wall and three decay. The far field quiescent outer conditions requires

all disturbances to decay far from the boundary, forcing the coefficients multiplying the growing solutions to be equated to zero. Then the three remaining roots can be arranged as a single inviscid mode (A) and two viscous ones (B) and (C) as follows:

(A) as $\eta \to \infty$

$$\hat{u} = e^{-\Gamma\eta} \tag{15}$$

$$\hat{v} = i\frac{\Gamma}{\alpha}e^{-\Gamma\eta} \tag{16}$$

$$\hat{w} = \frac{\beta}{\alpha}e^{-\Gamma\eta} \tag{17}$$

and

$$\hat{\zeta}_x = \hat{\zeta}_y = \hat{\zeta}_z = 0 \tag{18}$$

(B)

$$\hat{u} = e^{-p\eta} \tag{19}$$

$$\hat{v} = \frac{i\alpha}{p}e^{-p\eta} \tag{20}$$

$$\hat{w} = 0 \tag{21}$$

$$\hat{\zeta}_x = -\frac{\alpha\beta}{p}e^{-p\eta} \tag{22}$$

$$\hat{\zeta}_y = i\beta e^{-p\eta} \tag{23}$$

$$\hat{\zeta}_z = -\left(\frac{\alpha^2}{p} - p\right)e^{-p\eta} \tag{24}$$

(C)

$$\hat{u} = 0 \tag{25}$$

$$\hat{v} = \frac{i\beta}{p}e^{-p\eta} \tag{26}$$

$$\hat{w} = e^{-p\eta} \tag{27}$$

$$\hat{\zeta}_x = \left(p - \frac{\beta^2}{p}\right)e^{-p\eta} \tag{28}$$

$$\hat{\zeta}_y = -i\alpha e^{-p\eta} \tag{29}$$

$$\hat{\zeta}_z = -\frac{\alpha\beta}{p}e^{-p\eta} \tag{30}$$

Equations (8) through (11) were integrated by a 4th order Runge-Kutta scheme from the outer boundary marching towards the wall boundary. There are six fundamental solutions, but because of the outer boundary condition requiring all perturbations to decay, three of the arbitrary constants can immediately be equated to zero. The three remaining roots are evaluated by integration from the outer regions to the wall, where the boundary values can be applied to determine the remaining constants multiplying the individual roots. Unfortunately these three roots will inevitably exhibit parasitic growth as each solution becomes contaminated by the unwanted component arising from the stiffness of the equation set. At the end of each integration step all the solution variables and their derivatives are defined. These can be combined together in any convenient way to remove the parasitic growing solutions, providing new variables for the next integration step. Here it turned out to be convenient to set two velocity components to zero, leaving the remaining velocity component unspecified at this stage. The same combination of roots was then applied to all variables and derivatives needed to continue the integration. The various scaling factors used were also stored. This process of stepwise integration and filtering was continued to the wall where the remaining boundary condition was applied. If the choice of wavenumbers was compatible with an eigenmode of the system the remaining velocity component would then also be zero. An iteration scheme was set-up to vary the wavenumbers or frequency parameter until all the velocity components became zero at the boundary. The eigenfunction could then be readily reconstructed from the previously stored scaling factors. In tests to ascertain the accuracy of the scheme comparisons were made with values from a very accurate Compound Matrix integration scheme. Generally 8 figure agreement was found for the eigenvalues when sufficient integration steps were employed.

1.1.4 Boundary Value Problem

Appropriate boundary conditions defined in (1) through (6) together with the transform relation (7) give the necessary boundary conditions in the variables used in the equations (8) through (11) . It is much more appropriate to split the problem into separate cases for the different wall boundary values. The solution to a general problem with multiple boundary values differing from zero can be re-constructed by an appropriate linear combination of these solutions. The solution form then appears as

$$Q_j = \frac{1}{4\pi^2} \int \int \frac{\hat{Q}_j(\alpha, \beta, \eta)}{\hat{u}(\alpha, \beta, \omega, 0)} e^{i(\alpha x + \beta z - \omega t)} \, d\alpha \, d\beta \qquad (31)$$

where Q_j represents any one of the integration variables or derivatives for the case when the boundary value is applied on u. Similar expressions are used when the boundary value is specified in terms of one of the other velocity components.

1.1.5 Evaluating the Integral

It is convenient first to focus on the somewhat simpler two-dimensional problem with β set to zero. The integrals that have to be evaluated then take the form

$$Q_j(x, y, t) = \frac{1}{2\pi} \int \frac{\hat{Q}_j(\alpha, \eta)}{\hat{u}(\alpha, 0)} e^{i(\alpha x - \omega t)} \, d\alpha \qquad (32)$$

where Q_j represents any one of the integration variables or derivatives. The main difficulty in evaluating the integral arises because the integrand will in general be singular at eigenvalues of the system, but in the boundary layer situation there is only likely to be one unstable mode. There are also branch cuts in the α-plane, but these do not interfere with integration along the real axis. Difficulties associated with the unbounded eigensolution can be eliminated by subtracting the singularity from the integrand that occurs when $\alpha = \alpha^*$ and then treating the singular part of the inversion analytically. The complete solutions is then the summation of the numerically determined regular integral and the wavy part arising from the pole.

Equation (32) then reduces to

$$Q_j(x,y,t) = \frac{1}{2\pi} \int \left[\frac{\hat{Q}_j(\alpha,\eta)}{\hat{u}(\alpha,0)} - \frac{\hat{Q}_j(\alpha^*,\eta)}{(\alpha-\alpha^*)\partial\hat{u}(\alpha^*,0)/\partial\alpha} \right] e^{i(\alpha x - \omega t)} \, d\alpha \qquad (33)$$

This approach is especially useful as it separates out the near-field solution and the far-field eigensolution. The appropriate eigensolutions for weakly non-parallel flows can be computed without too much difficulty and used to replace this term. In this way it should be possible to construct solutions that are valid over the whole of the physical plane. The second term in the above equation provides the magnitude of the response, or the *receptivity*, of the boundary layer to boundary perturbations.

The flow disturbances created by any three-dimensional source can be constructed from a series of two-dimensional solutions obtained for different spanwise wavenumbers. The solution in physical space is then formed by taking the Fourier transform in spanwise wavenumber. For each boundary value calculations of the 6 variables were made covering a range of grid points over the three physical co-ordinates. These may be plotted out in various ways to show particular features. It turns out that experimental measurements of any other quantity than the stream wise velocity are very difficult to make. Mostly, therefore, only the u component was stored.

1.2   Experimental Investigations

The experiments discussed here were carried out in the 3ft square low-turbulence wind-tunnel at Queen Mary College. This tunnel is of conventional closed circuit design with a contraction ratio of around 7:1. The settling chamber is fitted with a honeycomb followed by four screens in order to provide a very low intensity of turbulence at the entry to the working section of below 0.01% between 2Hz and 2kHz. Although the turbulence intensity increases downstream the level remains acceptably low over the length of the centrally mounted flat plate. The experiments measurements were made in the boundary layer that formed on the 10mm thick aluminum plate. The 1.5 m long plate was fitted with a wooden leading edge of elliptic form and trailing edge flaps that could be set to make the flow over the front

700mm close to zero pressure gradient. Circular inset discs of 210 mm diameter could be fitted into the plate containing the different exciter jets at 500 mm from the leading edge.

The tunnel was fitted with a computer controlled three-dimensional hot-wire traverse. The computer was set up to monitor the temperature, atmospheric pressure, flow speed, the hot-wire signal and it also controlled the D/A that created the excitation source signal, the A/D converters and filters and the tunnel speed. To improve the ability to measure quite small fluctuations by the hot-wire data collection was synchronized with the excitation. Ensemble averaging of the hot-wire signal over long records effectively reduced the influence of noise and enabled measurements to be made at amplitudes well below the background level of the wind tunnel. Because of the long records required the data collection process could take many hours, or even days. However, once set-up on the computer, the tunnel could be left to collect data unattended overnight or sometimes over a weekend.

The periodic excitation was provided by a piston working in a cylinder driven by an electro-mechanical vibrator. Measurement of the piston movement was by an induction system capable of resolving 2 microns displacement. Various piston sizes were used to cater for a range of mass flows. The output was coupled to the jets on the insert disk by a flexible pipe of 100 mm. The exciter assembly was mounted off the reverse side of the plate on tensioned wires to reduce the amount of vibration transmitted to the plate.

1.3 Direct Numerical Simulations

The full three-dimensional incompressible Navier-Stokes equations are used to predict the velocity fields produced by actuators of various types. The computations are made using Direct Numerical Simulation where a discretized version of the Navier-Stokes equations is solved using a computer. The code used in the present investigation was originally written by Meitz and Fasel (2000), and has been appropriately modified

for the present investigations to model flow control actuators of various shapes.

1.3.1 Governing Equations

The incompressible Navier-Stokes equations are given as

$$\nabla \cdot \mathbf{u} = 0 \tag{34}$$

$$\frac{\partial \mathbf{u}}{\partial t} + \mathbf{u} \cdot \nabla \mathbf{u} = \mathbf{F} - \nabla p + \frac{1}{Re} \nabla^2 \mathbf{u} \tag{35}$$

These equations have been non-dimensionalized with the free-stream velocity, U_∞, and a reference length L

$$x = \frac{x^*}{L} \quad , \quad y = \frac{y^*}{L} \quad , \quad z = \frac{z^*}{L} \quad , \quad t = \frac{t^*}{L/U_\infty} \quad , \tag{36}$$

$$u = \frac{u^*}{U_\infty} \quad , \quad v = \frac{v^*}{U_\infty} \quad , \quad w = \frac{w^*}{U_\infty} \tag{37}$$

The global Reynolds number Re is defined as $U_\infty L/\nu$. Taking the curl of the Navier-Stokes equations eliminates the pressure term, and results in the vorticity transport equation

$$\frac{\partial \boldsymbol{\omega}}{\partial t} + \mathbf{u} \cdot \nabla \boldsymbol{\omega} = -\nabla \times \mathbf{F} + \boldsymbol{\omega} \cdot \nabla \mathbf{u} + \frac{1}{Re} \nabla^2 \boldsymbol{\omega} \tag{38}$$

where the vorticity $\boldsymbol{\omega}$ is defined as

$$\boldsymbol{\omega} = -\nabla \times \mathbf{u} \tag{39}$$

or in Cartesian components

$$\omega_x = \frac{\partial v}{\partial z} - \frac{\partial w}{\partial y} \tag{40}$$

$$\omega_y = \frac{\partial w}{\partial x} - \frac{\partial u}{\partial z} \tag{41}$$

$$\omega_z = \frac{\partial u}{\partial y} - \frac{\partial v}{\partial x} \tag{42}$$

where u, v, and w are the velocity components in the stream wise (x), normal (y), and spanwise (z) directions, respectively. Using the fact that both the velocity and the

vorticity vectors are solenoidal, equation (38) yields three equations for the stream wise (ω_x), normal (ω_y), and spanwise (ω_z) components of the vorticity

$$\frac{\partial \omega_x}{\partial t} = -\frac{\partial a}{\partial y} + \frac{\partial c}{\partial z} + \frac{1}{Re}\nabla^2 \omega_x + f_x \tag{43}$$

$$\frac{\partial \omega_y}{\partial t} = \frac{\partial a}{\partial x} - \frac{\partial b}{\partial z} + \frac{1}{Re}\nabla^2 \omega_y + f_y \tag{44}$$

$$\frac{\partial \omega_z}{\partial t} = -\frac{\partial c}{\partial x} + \frac{\partial b}{\partial y} + \frac{1}{Re}\nabla^2 \omega_z + f_z \tag{45}$$

where f_x, f_y, and f_z are the components of $-\nabla \times \mathbf{F}$, and the nonlinear terms are

$$a = v\,\omega_x - u\,\omega_y + v_B\,\omega_x - u_B\,\omega_y \tag{46}$$

$$b = w\,\omega_y - v\,\omega_z - v_B\,\omega_z - v\,\omega_{z\,B} \tag{47}$$

$$c = u\,\omega_z - w\,\omega_x + u_B\,\omega_z + u\,\omega_{z\,B} \tag{48}$$

Equations (43) through (48) have been written in disturbance flow formulation, where a total flow variable is split into a steady, two-dimensional base flow, and an unsteady disturbance

$$u_T(x, y, z, t) = u_B(x, y) + u(x, y, z, t) \tag{49}$$

$$v_T(x, y, z, t) = v_B(x, y) + v(x, y, z, t) \tag{50}$$

$$w_T(x, y, z, t) = w(x, y, z, t) \tag{51}$$

$$\omega_{xT}(x, y, z, t) = \omega_x(x, y, z, t) \tag{52}$$

$$\omega_{yT}(x, y, z, t) = \omega_y(x, y, z, t) \tag{53}$$

$$\omega_{zT}(x, y, z, t) = \omega_{zB}(x, y) + \omega_z(x, y, z, t) \tag{54}$$

Using the definition of vorticity, equations (40) through (42), and the continuity equation (34), one can obtain three equations for the velocity components

$$\nabla^2 v = \frac{\partial \omega_x}{\partial z} - \frac{\partial \omega_z}{\partial x} \tag{55}$$

$$\frac{\partial^2 w}{\partial x^2} + \frac{\partial^2 w}{\partial z^2} = \frac{\partial \omega_y}{\partial x} - \frac{\partial^2 v}{\partial y \partial z} \tag{56}$$

$$\frac{\partial^2 u}{\partial x^2} + \frac{\partial^2 u}{\partial z^2} = -\frac{\partial \omega_y}{\partial z} - \frac{\partial^2 v}{\partial x \partial y} \tag{57}$$

The flow is assumed to be periodic in the spanwise (z) direction, and each variable is expanded as a Fourier series. For example

$$u(x,y,z,t) = U_0(x,y,t) \; + \; \sum_{k=1}^{K} U_k(x,y,t)\cos(\gamma_k z)$$

$$+ \; \sum_{k=K+1}^{2K} U_k(x,y,t)\sin(\gamma_k z) \tag{58}$$

$$\omega_x(x,y,z,t) = \Omega_{x0}(x,y,t) \; + \; \sum_{k=1}^{K} \Omega_{xk}(x,y,t)\sin(\gamma_k z)$$

$$+ \; \sum_{k=K+1}^{2K} \Omega_{xk}(x,y,t)\cos(\gamma_k z) \tag{59}$$

where

$$\gamma_k = \begin{cases} \dfrac{2\pi k}{\lambda_z} & : \quad 1 \le k \le K \\[3mm] -\dfrac{2\pi(k-K)}{\lambda_z} & : \quad K+1 \le k \le 2K \end{cases} \tag{60}$$

Substituting the appropriate expansions into the vorticity transport equations (43), (44), (45) and the velocity equations (55), (56), (57) yields the governing equations in Fourier space, the vorticity transport equations

$$\frac{\partial \Omega_{xk}}{\partial t} = -\frac{\partial A_k}{\partial y} - \gamma_k C_k + \frac{1}{Re}\nabla_k^2 \Omega_{xk} + F_{xk} \tag{61}$$

$$\frac{\partial \Omega_{yk}}{\partial t} = \frac{\partial A_k}{\partial x} + \gamma_k B_k + \frac{1}{Re}\nabla_k^2 \Omega_{yk} + F_{yk} \tag{62}$$

$$\frac{\partial \Omega_{zk}}{\partial t} = -\frac{\partial C_k}{\partial x} + \frac{\partial B_k}{\partial y} + \frac{1}{Re}\nabla_k^2 \Omega_{zk} + F_{zk} \tag{63}$$

and the velocity equations

$$\nabla_k^2 V_k = \gamma_k \Omega_{xk} - \frac{\partial \Omega_{zk}}{\partial x} \tag{64}$$

$$\frac{\partial^2 W_k}{\partial x^2} - \gamma_k^2 W_k = \frac{\partial \Omega_{yk}}{\partial x} + \gamma_k \frac{\partial V_k}{\partial y} \tag{65}$$

$$\frac{\partial^2 U_k}{\partial x^2} - \gamma_k^2 U_k = -\gamma_k \Omega_{yk} - \frac{\partial^2 V_k}{\partial x \partial y} \tag{66}$$

where the Laplacian operator is defined as

$$\nabla_k^2 = \frac{\partial^2}{\partial x^2} + \frac{\partial^2}{\partial y^2} - \gamma_k^2 \tag{67}$$

In the present approach, the vorticity values at the wall are not computed from the vorticity transport equations (61), (62), and (63). For consistency, they are instead computed from the following equations

$$\frac{\partial^2 \Omega_{xk}}{\partial x^2} - \gamma_k^2 \Omega_{xk} = -\frac{\partial^2 \Omega_{yk}}{\partial x \partial y} - \gamma_k \nabla_k^2 V_k \tag{68}$$

$$\Omega_{yk} = \frac{\partial W_k}{\partial x} + \gamma_k U_k \tag{69}$$

$$\frac{\partial \Omega_{zk}}{\partial x} = \gamma_k \Omega_{xk} - \nabla_k^2 V_k \tag{70}$$

The right hand side of equation (68) can be computed, and with inflow and outflow boundary conditions specified, Ω_{xk} can be determined. Because the values of w and u are known at the wall, Ω_{yk} can be computed from equation (69). Finally, the right hand side of equation (70) is known, and Ω_{zk} can be computed by integrating from the inflow.

The governing equations are solved using a fourth-order accurate compact difference scheme in space (see Lele (1992), Meitz and Fasel (2000)), with an explicit fourth-order Runge-Kutta method for time advancement.

1.3.2 Modeling Flow Control Actuators using the Immersed Boundary Method

Theoretical Aspects The immersed boundary method is a numerical method for solving boundary-value and initial/boundary-value problems on irregular domains. Irregular domains contain boundaries that do not conform "nicely" (e.g., rectangular boundaries in Cartesian coordinates) to the coordinate system being used. The method promises to do this more easily, generally, accurately and efficiently than has been possible up to now using standard methods employing body-fitted or unstructured grids.

With regard to figure 1, one would typically like to solve a PDE defined on the open region Ω^+ with boundary conditions on $\partial\Omega_o$, the outer boundary, and $\partial\Omega_i$, the immersed boundary. The solution in the region Ω^- (which is the complement

of $\Omega^+ \cup \partial\Omega_o \cup \partial\Omega_i$) may or may not be of interest. For example, if one would like to simulate the interaction of a thin, elastic membrane submerged in and filled with a fluid, then the governing equations both inside (in Ω^-) and outside (in Ω^+) of the membrane would have to be solved. Upon approaching the limit of an infinitely rigid shell, however, only the solution outside of the membrane would likely be of importance. In either case, the immersed boundary $\partial\Omega_i$ represents a singularity if one considers that, say the governing partial differential field equations, apply throughout the entire domain enclosed by $\partial\Omega_o$; field variables and/or their derivatives will be discontinuous across the immersed boundary.

In the immersed boundary method, a forcing term $\mathbf{F}(\mathbf{x}, t)$ is added to the right hand side of the momentum equation (35) to represent this singularity. The volume force $\mathbf{F}(\mathbf{x}, t)$ is to be determined such that the no-slip condition can be enforced on a given body defined by its bounding surface S. This volume force will cause the fluid velocity to assume the local surface-velocity at each point on the body. Let

$$\mathbf{x} = \mathbf{X}(r, s, t) \tag{71}$$

be a Lagrangian, parametric representation of the body surface S. We can define another function $\mathbf{f}(r, s, t)$ such that

$$\mathbf{F}(\mathbf{x}, t) = \int_S \mathbf{f}(r, s, t)\, \delta(\mathbf{x} - \mathbf{X}(r, s, t))\, dr\, ds \tag{72}$$

where $\delta(\mathbf{x})$ is the Dirac δ-function. The field $\mathbf{F}$ given by equation (72) is not an ordinary function, but a distribution which is zero everywhere except on the body surface. Integrating both sides of equation (72) over an arbitrary region R

$$\int_{\mathbf{x} \in R} \mathbf{F}(\mathbf{x}, t)\, d\mathbf{x} = \int_{X(r,s,t) \in R} \mathbf{f}(r, s, t)\, dr\, ds \tag{73}$$

since

$$\int_{\mathbf{x} \in R} \delta(\mathbf{x} - \mathbf{X}(r, s, t))\, d\mathbf{x} = \begin{cases} 1 & \mathbf{X}(r, s, t) \in R \\ 0 & \text{otherwise} \end{cases} \tag{74}$$

which shows that equation (72) makes sense.

The formulation represented by equation (72) is such that the surface S appears as a linear superposition of the correct forces. Another interesting feature of this formulation is that two distinct regions can be identified for closed surfaces: the space inside S, and the space outside S. The flow produced inside a closed surface will not be of any immediate interest, and is simply a by-product of the method.

Numerical Implementation Denote by $\mathbf{f}(\mathbf{x}_s, t)$ and elemental volume force at a point $\mathbf{x}_s$ on the surface S. The task of determining $\mathbf{f}(\mathbf{x}_s, t)$ still remains to be discussed. In their paper, Goldstein et. al. (1993) suggest a type of feedback loop

$$\mathbf{f}(\mathbf{x}_s, t) = \alpha \int_0^t \mathbf{u}(\mathbf{x}_s, \tilde{t}) \, d\tilde{t} + \beta \, \mathbf{u}(\mathbf{x}_s, t) \tag{75}$$

where α and β are negative constants. One can see how the force defined in equation (75) will eventually bring the flow to rest at the point $\mathbf{x}_s$. Assuming $\mathbf{u}$ to be, say, positive along one of the Cartesian axes, the force will act in the opposite direction, causing the fluid particle to slow down and eventually stop, assuming that the flow has a steady-state solution. At this time, $\mathbf{u} = 0$, and $\mathbf{f}$ no longer changes with time. For unsteady flows, one can understand the behavior of the formulation given by equation (75) in the following heuristic way. With an approximate form of the momentum equation taken as

$$\rho \frac{d\mathbf{u}(\mathbf{x}_s, t)}{dt} \approx \mathbf{f}(\mathbf{x}_s, t) = \alpha \int_0^t \mathbf{u}(\mathbf{x}_s, \tilde{t}) \, d\tilde{t} + \beta \, \mathbf{u}(\mathbf{x}_s, t) \tag{76}$$

one can see that the behavior is approximately that of a damped harmonic oscillator with mass $\approx \rho \, d\mathbf{x}^3$, spring constant α, and viscous damping β.

In earlier studies, Viecelli (Viecelli (1969), Viecelli (1971)) introduces an iterative method to model immersed moving surfaces. Using the MAC, or Marker and Cell, method for solving the time-dependent, incompressible flow equations, the pressure in boundary cells, i.e. those near a moving wall, are determined by the following relaxation equation (Viecelli's equation (9), Viecelli (1971))

$$P_{k,l}^{i+1} = P_{k,l}^i - \frac{\Delta \tau}{\delta} \left(\left[(\mathbf{V}_p^{n+1})^i - \mathbf{V}_b(\mathbf{r}, t) \right] \cdot \mathbf{n} \right)_{k,l} \tag{77}$$

where $\mathbf{V}_p^{n+1}$ is the computed velocity, $\mathbf{V}_b(\mathbf{r}, t)$ is the required velocity, $\mathbf{n}$ is a unit vector normal to the surface, δ is the mesh width, and $\Delta\tau$ is a relaxation parameter. In this formulation, the pressure is adjusted within the iteration loop until convergence is achieved, at which point the velocities obtained match those prescribed, within a given tolerance.

The present approach to determining $\mathbf{f}(\mathbf{x}_s, t)$ is a mixture of the two methods described above. Equation (72) is discretized as

$$\mathbf{F}(\mathbf{x}, t) = \sum_s \mathbf{h}_s(t)\delta(\mathbf{x} - \mathbf{x}_s(t)) \tag{78}$$

where $\mathbf{x}_s(t)$ is one member of the finite set of points selected as a discrete representation of the no-slip surface S. The value of $\mathbf{h}_s(t)$ is determined iteratively during the course of the calculation

$$\mathbf{h}_s^{i+1}(t^n) = \mathbf{h}_s^i(t^n) - \beta\left[\mathbf{V}_s(t^{n+1}) - \mathbf{V}_{bs}(t^{n+1})\right] \tag{79}$$

where $\mathbf{V}_s(t^{n+1})$ is the velocity computed at point $\mathbf{x}_s$, $\mathbf{V}_{bs}(t^{n+1})$ is the required velocity at this same point, and β is a relaxation factor. The computed velocity of points not coinciding with the computational grid were obtained by interpolation using a second-order polynomial. The delta function was approximated by a Gaussian function

$$\delta(\mathbf{x} - \mathbf{x}_s(t)) = \frac{1}{\pi\sigma_x\sigma_y\sigma_z}\exp\left[-\left(\left(\frac{x - x_s(t)}{\sigma_x}\right)^2 + \left(\frac{y - y_s(t)}{\sigma_y}\right)^2 + \left(\frac{z - z_s(t)}{\sigma_z}\right)^2\right)\right] \tag{80}$$

Additional information regarding our implementation of the immersed boundary technique can be found in von Terzi et. al (2001).

2 Validation

It is of course necessary to validate the computational scheme before using it in anger to explore the effects of Reynolds number, Pressure gradient, excitation frequency etc. This can be accomplished by comparison with full DNS as well as by comparison with experimental measurements. First, we will discuss the experimental validation.

2.1 Validation of Theoretical Approach

2.1.1 The normal Jet

Although experiments were carried out at a number of different frequencies we will only report the measurements obtained at the frequency of 96 Hz as the other values showed very similar results. The level of excitation was adjusted and the resulting perturbations were measured through the boundary layer at some downstream station. By noting how the perturbation divided by the excitation behaved it was possible to determine a level that produced linear response. A periodic jet velocity of amplitude 0.1 m/s of the free-stream, averaged across a 2mm normal jet, was found to be below this threshold and was used with a mean tunnel speed of 10 m/s. The flow along the center-line of the wedge- shaped zone containing the stream wise perturbations was mapped out. Figure 2.2.1.1 shows the in-phase and out-of-phase components plotted on the x–y plane. The initial zone close to the jet is dominated by the near field, but by about 100mm downstream of the source the disturbance pattern has formed into a progressing wave-train. On these plots, and all those in section 2.1, the contours are drawn at levels equal to the square root of ten, with the level at the decades shown in thick lines. The lowest level contour is drawn at an amplitude of 0.001% of the free-stream value. The figure also shows the predicted oscillations obtained by the linear theory for the same conditions that were used in the experiment. There seems little purpose in showing vast numbers of very similar plots obtained at different frequencies as they all compared very favorably with predictions. The spanwise development is shown on figure 2.2.1.2 for traverses on the z–y plane taken at 100mm from the source. The upper plots contain the theory whilst the lower ones show the predictions for the in-phase and modulus. In this comparison an arbitrary phase was included in the theoretical calculations because, as can be seen in the previous plot the phases do not match very closely.

2.1.2 Inclined Jets

An insert disk was fabricated with a set of obliquely inclined jet exit holes. They were inclined at 30 degrees to the boundary pointing upstream, downstream and in the spanwise direction. The jet pipes were kept at 2mm diameter, but this meant that the elliptic exit hole was 2mm by 4mm and hence had double the area of the circular jet hole. The inactive holes were blocked with tape. A series of traverses similar to those obtained for the normal jet were made with the jets pointing upstream and downstream. The resulting plots were only slightly different from those shown above for normal jet orientations because the receptivity to the u boundary value is very small compared with that created by a v excitation as will be shown in the section 5. The upstream/downstream pictures showed negligible differences to that of the normal jet. The spanwise traverses indicated that the forward jet created a slightly larger perturbation than the downstream one. This is somewhat counter intuitive, but this behavior was confirmed by the linear theory. It does not seem worthwhile showing all the plots created as they show little that is new or unexpected. It should be noted that although the normal component of the jet was halved by the angle of inclination the area of the jet was increased by two and the resultant excitation in terms of mass flux remained unchanged. Jets inclined along the span were also investigated. Again the effect of the boundary value is weak and the result on the stream wise velocity component was negligible. The excitation from the spanwise component is an odd function of the z coordinate and can be expected to have zero influence on the flow along the center-line which is controlled solely by the normal component of the jet. This was confirmed by experimental measurement. Again it does not seem worth showing a measurement indistinguishable from that of the normal jet. The transverse pictures do show some weak asymmetry and this is shown together with predictions on figure 2.2.2.

2.1.3   Jet Size

A series of normal jets of 1mm, 2mm and 4mm diameter were investigated. The mass flow was reduced from the levels used previously to make sure that the higher jet speed arising in the small jet case did not cause any unwanted nonlinear behavior. The mass flows were slightly different from one another, but the measurements have been linearly scaled to compensate for these small differences. Figure 2.2.3 shows three contour plots of the stream wise disturbance fluctuation on the z-y plane at 100mm downstream of the source. Because of the lower excitation level an extra contour at 0.000316% is included. The patterns for the two smallest jets are virtually identical to one another, but that of the wider 4mm jet is different. The wider jet orifice will naturally create a slight spread in pattern, but the observed differences confirm that the mechanics of generation depend on the exit mass flow.

2.2   Validating the Immersed Boundary Method

Several tests were performed to validate the immersed boundary method as a suitable tool for actuator simulations. The first test was to see how well the method could produce a zero pressure-gradient, flat-plate boundary layer when a flat plate was immersed in the computational domain. The setup is shown in figure 2. The flat plate is located well inside the true, body-fitted, computational domain, and is simulated as an immersed boundary. That is, we imagine a the lower wall of a standard rectangular cartesian domain being moved upward, parallel to itself, into the computational domain. The solution at points below the immersed wall is still computed, but does not influence the solution above the immersed wall.

As a first step, the undisturbed base flow is computed. Figures 3 through 6 compare the steady profiles obtained using a standard body-fitted code (solid line), and those obtained from the immersed boundary simulation (symbols). A small deviation near the immersed wall can be seen in the zoom-in plots, but overall, excellent agreement with the body-fitted results is achieved indicating that the immersed boundary

technique is able to capture mean-flow characteristics quite well.

Flows in which near wall accuracy is important present a much tougher test case for the numerical method. A good example of the is the simulation of Tollmien-Schlichting waves which are produced when disturbances are introduced into the flat plate boundary layer. If the frequency of the disturbance is selected properly, the T-S waves will be unstable with respect to the underlying base flow, and will amplify as they are convected downstream. Obtaining the correct amplification rates is important if flow control simulations are to be carried out with the code. Moreover, many body-fitted codes have difficulties predicting the correct amplification rates.

Growth rates computed over the immersed flat plate are shown in figure 7, where the maximum in the u-disturbance profile is followed. For comparison, the results obtained using the underlying body-fitted code, and the results of standard linear stability theory (using the Orr-Sommerfeld equation) are plotted as well. The results obtained using the immersed boundary method are shown for several different temporal discretizations (non-dimensionalized to form the CFL, or Courant-Friedrichs-Lewey number). A smaller time step than that needed for numerical stability is seen to be required in order to obtain correct amplification rates. The reason for this is the approximate nature of the feed-back mechanism for determining the volume forces discussed above. As the CFL number is reduced, however, the solution appears to converge, and the results obtained are close to those predicted by a standard DNS. The corresponding disturbance velocity distributions (eigenfunctions, when comparing with Orr-Sommerfeld theory) are shown in figures 8 through 11. Good agreement is found.

3 Predictions based on the Linear Model

In the previous section some comparisons between measurement and prediction based on the linear model are shown of measured disturbances downstream of periodic point sources. These pictures show a remarkably consistent correlation and suggest that

the theory can indeed be used to predict the disturbance field. There seems no reason to suppose that the theoretical model cannot be extended to cover boundary layers with pressure gradients and jets of different frequencies. The numerical scheme has been used to explore the downstream disturbances created by various boundary value excitations under a wide range of flow parameters. Instead of using dimensions that naturally enable comparisons with experimental data to be made as was done in the sections discussing validation it is more convenient now to employ non-dimensional units. All lengths are scaled by the displacement thickness at the source, and all velocities by the free-stream.

3.1 Responses to Boundary Conditions

Under one flow condition, zero pressure gradient F-number of 100×10^{-6} and Reynolds number 1000, the disturbance fields has been computed for the three velocity boundary values. In each calculation all the three velocity components as well as the three orthogonal fluctuating vorticities have been stored and are plotted on figure sets 3.1.1(i - vi), 3.1.2(i - vi) and 3.1.3(i - vi) respectively. All excitations are of unit magnitude over a source region equal to the square of the displacement thickness. As in the previous sets of contours the levels are powers of the square root of 10, with the alternate decade contours set in thicker lines. All the perturbations are normalized by the free-stream velocity, and the vorticities also by the displacement thickness. Each set of figures contains three sections of the flow field for that particular excitation and disturbance quantity. When the solution is an even function of the spanwise dimension then the section in the x-y plane has been taken along the center-line, but if this section is a point of symmetry we have taken a slice 25 displacement thickness off the axis. The z-y sections have been plotted as absolute values at appropriate distances downstream. The absolute values are more meaningful here because the picture is not confused by the phase properties that will change over small distances downstream. The horizontal cut has been taken roughly where the perturbations are

largest. Contours are again drawn at decade levels in thick lines and light lines at the square root of 10. The lowest contour is at 0.001 of the free-stream. It turns out that a v excitation creates velocity disturbances downstream that are roughly ten times as large as the values produced by either a u or a w wall perturbation. For this reason it has been necessary to include a decade smaller contour level on figures 3.1.1(i, ii, iii) and 3.1.3(i, ii, iii) that define the velocities created by u and w excitation respectively. In general the contour plots show that the disturbances establish a clear pattern of propagating waves after about 100 displacements thickness downstream. All the disturbances spread out in width downstream at the same rate. A small clearly defined region around the source indicates the upstream extent of the near field. It might be expected that the stream wise vorticity is effectively created by a spanwise wall excitation, w , but it turns out that a normal velocity component excitation is not only more effective in creating velocity fluctuations but as a consequence also creates larger streaming vorticity.

3.2 Influence of Frequency

Although all the physical quantities described in the previous section could be displayed for the three forms of excitation we have here concentrated on the u perturbations created by a normal boundary excitation as this seems to be the most important case. Calculations similar to those of section 3.1 have been carried out at a fixed Reynolds number of 1000 and at zero pressure gradient for different Fnumbers. The patterns shown in figures 3.2(i - vi) are perhaps just what one might expect and mainly reflect the different amplification rates as the frequency is changed. The lowest Fnumber of 25×10^{-6} lies below the lower branch of the neutral loop and so the two-dimensional modes are damped and the patterns plotted on figure 3.2 (i) are dominated by oblique waves that become more important in these circumstances. At frequencies that contain modes above the upper branch everything is again damped and at some distance downstream the disturbances vanish. Apart from the lowest

frequency the solutions upstream of the source are quite similar to one another, but at the low frequency it appears that the near-field zone is enlarged.

3.3 Influence of Pressure Gradient

A set of computations was carried out for an Fnumber of 100×10^{-6} and a Reynolds number of 1000 over a range of Falkner-Skan similarity parameter values. The imposed pressure gradient mainly influences the pattern through the amplification rates that are obtained under the different rates of acceleration. The data is displayed on figure 3.3 (i) to 3.3 (v). What is particularly striking in this set is the close similarity of the solution for all pressure gradients in the region just upstream of the source.

3.4 Influence of Reynolds number

In this part of the investigation the pressure gradient was set to zero and the Fnumbers and Reynolds number varied so that the real frequency, the product of the Reynolds number and the Fnumber was kept constant. The idea behind this was to maintain a roughly constant wavenumber. The patterns shown on figures 3.4(i - v), especially for the x-y cut are all quite similar apart from the obvious effects arising from the variation in amplification rates. Again it appears that the near-field zone in front of the source is unchanged by Reynolds number.

4 Asymptotic Solutions

The previous plots indicated that apart from the region upstream of the source and roughly 50 - 100 displacements thicknesses downstream the responses arise purely from the dominant eigenmodes at each spanwise wavenumber Fourier transformed w.r.t. the z coordinate. Since in the calculation scheme the eigensolutions are separated out from the full numerical Fourier transform in the asymptotic part can be viewed by itself. This is a much simpler and quicker computation. The streamwise perturbation response to the two boundary values in u and v are shown on figures 4.0

(i - ii). These figures may be directly compared with the full solutions on 3.1.2 with identical scalings. The solutions over the downstream zones are well modeled by the asymptotic forms. The u excitation converges to the full solution more rapidly than the flow generated by the v excitation. This is because the v excitation creates a simple potential, or acoustic, near field in addition to the viscous field and the eigensolution common to both. The interference between the algebraic potential solution and the wavy eigensolution gives rise to the rather irregular behavior seen in the x-y plots on figures 4.0(i) and 4.0(ii) for the two excitations respectively.

5 Receptivity

The asymptotic response is dependent on the *receptivity* at the source as well as the amplified *eigenstructure* for that particular mode. There are of course a multitude of possible choices for defining receptivity, but it seems to be sensible to take an integration through the boundary layer to act as a guide to the degree of activity excited. Here we have taken the root of the integral of the square of the flow quantity in question across the boundary layer.

5.1 Raw Receptivity

The receptivities of individual modes provide some guidance as to how the different flow parameters are excited by the three possible boundary values. The receptivity of a flat plate boundary layer at a Reynolds number of 1000 to the three wall excitations are shown on the composite plots 5.1.1, 5.1.2 and 5.1.3. The six plots on each figure show the receptivity as a function of Fnumber and spanwise wavenumber for the various velocity and vorticity components. The neutral loop is also draw to show the region where the value of receptivities important. In some cases the value of the receptivity coefficient increases alarmingly with wavenumber or frequency, but this occurs over regions of the plane that are linked to highly damped eigenvalues that do not contribute to the true asymptotic behavior that is dominated by the region of

maximum amplification. These figures clearly show that the excitation by a normal jet is much more effective than of a tangential one. It is also clear that the largest perturbation velocity is that in the direction of the mean stream.

5.2 Effect of Reynolds number

The receptivity has been evaluated for the u flow field excited by a normal jet for a range of Reynolds numbers at zero pressure gradient, as this appears to be the most important case. The results are shown on figure 5.2 together with the appropriate neutral loop. Although the neutral loop moves as the Reynolds number is changed it would appear that the receptivity coefficients themselves do not change significantly over this range of Reynolds number. The far downstream asymptotic behavior contains the exponentially growing modes of the dominate unstable mode. The relatively weak algebraic influence of the raw receptivity coefficients has, therefore little effect on the amplitude that is dominated by the exponential factors.

5.3 Effect of Pressure Gradient

The Effect of varying the pressure gradient at constant Reynolds number is shown on figure 5.3. Again this set of plots indicates that receptivity in not greatly affected by changes in pressure gradient.

6   Excitation by a Periodic Bump

Small oscillating bumps have also been used to generate disturbances in boundary layers. Provided the bump is shallow the expression in equations (5) and (6) can be used to model the boundary values. Both a normal and a tangential excitation are therefore generated. From the studies of the inclined jets that also introduced an additional boundary value in terms of u it might be anticipated that this term contributes only weakly to the overall solution. But it turned out that the mean flow velocity gradient $\partial U/\partial y$ at the wall is numerically quite large and therefore both

boundary values contribute similarly to the overall downstream solution (see figure 21). In fact the two terms produce partial solutions that are of similar form but of opposite sign so that the overall perturbation created is often weaker than that produced solely by the normal component. A previous experimental investigation using a 2mm pin oscillating through a hole in the insert disk determined detailed measurements of the downstream flow created. It turned out that only quite small amplitudes could be excited if a linear response was to be maintained. The low signal levels created were far more difficult to measure accurately than those generated by an oscillating jet. Nevertheless, some comparisons were made with the theoretical predictions using the linear theory. The predictions were not well reflected by the measurements. At the time this was attributed to difficulties in accurately measuring the pin position and amplitude. After the wind tunnel was moved to Queen Mary College from Cambridge another attempt was made on these measurements. Using much improved measuring instruments and a better control of the flow speed etc. fresh data was collected. Again it has to be reported that the measurements did not match the predictions. These measurements were taken with great care and they indicated that the simple theory was, for some reason, wanting. It has now been established that the linearization of the boundary conditions is only valid for very small amplitudes of the pin. In the experiment this restricted the true linear behavior to amplitude of less than 10 microns. The signals are then very hard to measure. It would appear that for the typical amplitude being used of 50 microns the next term in the expansion for the boundary values is needed. A weakly nonlinear theory can then be established. This part of the work has not yet been completed, but work is still in progress. However, some measurements taken far downstream of an oscillating pin did show a much weaker disturbance level than for the oscillating jet of similar magnitude. Although the linear theory is inadequate for a complete description of the solution we show here a linear modeling of a particular case. Figure 6.0 contains the contour plots of the modulus of the disturbance downstream for the two boundary values. In this

situation, which was chosen especially to illustrate the behavior, the two flow patterns are almost identical. They are also correctly phased to cancel on another, as shown in the composite contour plot. Linear contour levels have been used here to illustrate the behavior more clearly. Other excitation frequencies or Reynolds numbers would create a different patterns with different degrees of cancellation, but clearly there are scenarios that provide for almost perfect annihilation of the asymptotic solution.

7 Nonlinear Effects

Some measurements have been made with excitations that are larger that the levels required for linear response. Three excitation levels were used and the spanwise traverses recorded at 100mm downstream from the source. Figure 7.0.1 shows these contour plots obtained with exit jet velocities of 0.10, 0.27 and 0.93 m/s respectively through a 2mm hole. For comparison, DNS results are shown in figure 29. The contours are plotted at amplitudes of steps square root of 10. The lowest contour level is at 0.001%. The plots for the two smallest excitation amplitudes are reasonably similar to one another while the highest level shows some differences. These types of measurement take a considerable amount of wind tunnel time. So in order to explore a wider range of examples only the central zone of the spanwise traverse was measured at rather coarse steps. The data was then integrated to give a measure of the integrated r.m.s. level. It was found that the restricted zone provided a level equal to over 90% of the value over the while zone. The increased speed of data collection enabled measurements to be made over a range of amplitudes and frequencies for the three excitation holes of 1mm, 2mm and 4mm diameter. Here only the data at 96 Hz will be shown as the other frequencies follow a similar behavior pattern. Figure 7.0.2 shows the integrated r.m.s. levels of the fundamental from the three jets over a range of mass flows. The mass flows are normalized by the free-stream velocity and the jet size in displacement thickness units. The summed data is normalized by the rms intensity as a percentage of the free-stream velocity over an area defined

in terms of the local displacement thickness. The records from the 2mm jet are the most complete and show the breakaway from the linear behavior and the subsequent increase in perturbation amplitudes with excitation level. The response is linear up to a mass flow of around 0.02 while the 1mm jet shows a break away at roughly half this level. Unfortunately there are no large amplitude cases for the 4mm jet. The behavior of the nonlinear component follows a cubic curve very closely for the 2mm case. A plot of the first harmonic component is shown on figure 7.0.3. Here the nonlinear behavior follows an expected quadratic for at low level of excitation and this blend in to a sixth order curve.

8 DNS Results

Using the immersed boundary technique described above, the velocity fields created by several types of actuators were computed. The examples given illustrate the ability of the immersed boundary technique to model the motion of flow control actuators which would otherwise be quite difficult and/or inefficient to carry out using standard methods. Here, a cartesian grid is selected at the beginning and does not change during the course of the calculation. The actuator surface, however, moves through the underlying cartesian grid. Again, the surface of the body is not required to intersect the underlying grid points, and arbitrarily shaped bodies can be modeled.

The first example of a flow control actuator is that of the vibrating ribbon. Following the development of the linear stability theory by Tollmien and Schlichting, experimental investigations were carried out to test the theory. Many of these original experiments, beginning in the early 1940's with those of Shubauer and Skramstad (1943), made use of a vibrating ribbon to excite 2-D boundary-layer oscillations. The ribbon was held under tension across the span of a flat plate, and made to oscillate by running an AC current through the ribbon which was immersed in a magnetic field. This technique was found to be capable of producing the desired 2-D boundary-layer disturbances.

A numerical simulation of a vibrating ribbon is described in this section. The ribbon motion is sinusoidal, and moves perpendicularly to the oncoming boundary layer. Dimensionally, the computational ribbon is 20 mm long (about 1/4 of a T-S wavelength), and is placed at approximately 0.056δ from the wall. All other parameters are as follows:

$$
\begin{aligned}
U_\infty &= 3.0 \text{ m/s} \\
\nu &= 1.5 \times 10^{-5} \text{ m}^2/\text{s} \\
L &= 0.5\text{m} \\
x_1 &= 0.9 \ (R_{\delta_1} = 516) \\
x_2 &= 3.3 \ (R_{\delta_1} = 989) \\
f^* &= 14.3 \text{ Hz}
\end{aligned}
$$

where x_1 is the inflow location, x_2 the outflow, and f the frequency of the vibrating ribbon. The near field disturbance caused by the ribbon is shown in figure 12 after a quasi-steady state has been reached. The flow field appears as one would expect: as the ribbon moves upward (downward), fluid moves inward (outward), under the ribbon; at the top or bottom of the ribbon stroke, a low Reynolds number flow regime exists. Streamwise velocity profiles corresponding to figure 12 are provided in figure 13 to show more detail.

The global behavior of the disturbance created by the ribbon can also be computed. As seen in figures 14 and 15, the frequency of the ribbon is such that amplifying waves are produced over a particular range of downstream Reynolds numbers. The disturbance distributions in the wall normal direction shown in figure 16 again compare well with linear stability theory.

The second example is that of a wall-mounted actuators. The actuator is described by

$$
y(x,t) = \frac{A}{2} \left(1 - \cos(2\pi f t + \phi)\right) \cos^3\left(\frac{\pi(x - x_c)}{w}\right) \quad |x - x_c| \geq w/2 \qquad (81)
$$

where x_c is the coordinate of the center of the actuator, and w is the total width of the actuator. This shape is shown graphically in figure 17.

The actuator is again modeled using the volume forcing technique. The spanwise disturbance-vorticity created by the sinusoidal movement of the wall mounted actuator is shown in figure 18. Shown is a time history of the actuator movement, the actuator at mid-stroke moving upward, the actuator at top stroke and stationary, and finally at mid-stroke moving downward. The global disturbance velocity produced by this motion is shown in figures 19 and 20. As expected, unstable T-S waves are produced which grow exponentially as they are convected downstream.

Results for a three-dimensional piston-type actuator are shown in figures 21 through 27. The piston is embedded in a flat plate over which a zero pressure gradient boundary layer has formed. Figures 21 through 24 depict the velocity field produced by a stationary piston actuator. In figure 21, we plot the streamwise velocity profiles caused by the presence of the actuator, and in the remaining figures, the disturbance velocity fields induced. Results for a sinusoidally moving piston actuator are shown in figures 25 and 26.

The final actuator investigated was a blowing and suction type actuator and was used as a validation case for the theoretical and experimental work discussed in the rest of this report. Physically, this actuator is realized by drilling a hole into the working surface, and placing a loudspeaker, for example, behind the surface to induce mass flow in and out of the hole. Numerically, this is the simplest actuator to model as it can be represented simply by applying a non-zero wall velocity disturbance.

Figure 27 shows the instantaneous streamwise disturbance velocity created by the blowing and suction hole. A characteristic bow-like structure can be seen as the disturbance is convected downstream. For this case, slices of data from the DNS are taken in the x-y and z-y planes and compared with results predicted from the theoretical analysis and from experimental data. The results, shown in figure 28, are in very good agreement, implying that the theoretical model is quite capable of

predicting the flow behavior in both the near and far field of the actuator.

9 Discussion

A linear theory for the disturbances created by wall boundary values has been established. Predictions based on this model have been shown to agree with remarkable detail to a series of measurements from a normal jet. Not only do the contour levels coincide with incredible accuracy, but many of the details of the contours match. Although the confirmation of theory has only been carried out for the case of the normal velocity boundary value and the resulting streamwise disturbance in a zero pressure gradient flow at one Reynolds number there is no reason to suppose that the model does not lend itself to cover other physical situations. The only disagreement appear in matching the phase downstream. This may well be associated with the fact that the theoretical model is for a purely parallel flow, whereas the real flow develops in thickness downstream. The 6 disturbance functions created by the three boundary values are shown for one flow condition. One can see that the patterns have some similarities with one another basically when the resultant is an odd or an even function of the spanwise co-ordinate. The normal velocity component creates disturbances in the flow roughly 10 times larger than that created by either of the other two boundary conditions. The effect of varying the Reynolds numbers, Fnumbers and the pressure gradient are explored for the most important case of a normal velocity excitation on a streamwise velocity disturbance component. The patterns of the contours shown follow roughly what one might expect in so far as the downstream flow is dominated by the amplification rates of the dominate modes. The disturbed zone around the source seems to be remarkably insensitive to the both the imposed pressure gradient and the Reynolds number. But the frequency of excitation does have some influence on the near field, especially at the lowest frequencies where the disturbed region is enlarged. Estimates of the disturbance based solely on the asymptotic eigen- solutions are very similar to those of the full calculation, particularly at distances greater than about 100

displacements thicknesses downstream. The rather unexpected interference patterns seen about 30 - 50 displacement thicknesses downstream, therefore, arise from the interaction between the oblique modes and are not, as one might suppose, from the near field. In most situations it would be sufficient to use the very much cheaper and quicker solutions based on asymptotic behavior. The receptivities of the disturbance quantities to the three boundary values have been calculated. Again it is clear that the normal boundary value component produces the largest disturbances. The plots of receptivity coefficient on the excitation frequency- wavenumber plots show that the actual values change only weakly with Reynolds number or Pressure gradient. There are some weak effects, but we are generally concerned with large amplitude downstream arising from the cumulative amplifications. Estimates of transition position by the n-factor method relies on the fact the receptivity is roughly a constant function of the Reynolds number and pressure gradient. Receptivity certainly plays a very important role in transition, but it appears that the environmental factors can be lumped together in an empirical way because of this insensitivity. Oscillating bumps can only be modeled by the linear boundary condition for very small amplitudes. A weakly nonlinear theoretical approach is being developed to cover larger amplitudes of pin movement. But from some brief experiments that are not reported here it was found that the bump produced much weaker downstream disturbances than would have been expected from the normal jet-like excitation component alone. This turns out to arise because the two parts of the exaction are of opposite sign and can cancel downstream This has been illustrated by a linear calculation for one particular set of parameters. But the result should provide a warning to those using this form of excitation. The nonlinear experiments that show a cubic form for the development of the fundamental with excitation level. This could be a weakly nonlinear amplification taking place that does lead to a cubic behavior, but the amplitudes in the main body of the solution are too small for this behavior. However, the region close to the source does includes regions of the flow with very large disturbances. It seems likely,

therefore, that the observations arise from a nonlinear receptivity mechanism. This could also be expected to follow a cubic form although the theory for this has yet to be formulated.

10   Conclusions

1. A linear theory has been developed to describe the disturbances from various forms of point excitation on the boundary wall.

2. Experimental validation for zero pressure gradient and one Reynolds number has been very satisfactory.

3. The theory has been used to explore the effect of excitation frequency, Reynolds number and pressure gradient.

4. The receptivities, based on the eigenmodes, have been obtained for a variety of flow conditions.

5. It has been shown that an oscillating bump produces two downstream flow fields that can cancel and generate a very weak response.

6. Direct Numerical Simulations have been performed. The calculations agree well with both the theoretical predictions as well as the experimental results. Additionally, an immersed boundary technique has been developed and validated. The technique was used to predict the flow field created by actuators of various geometries.

11   Figures
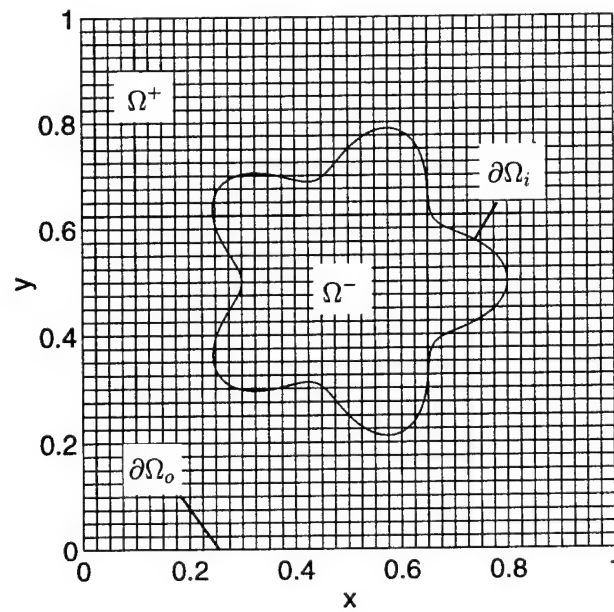
Figure 1: An irregular immersed boundary $\partial\Omega_i$ and computational Cartesian grid.
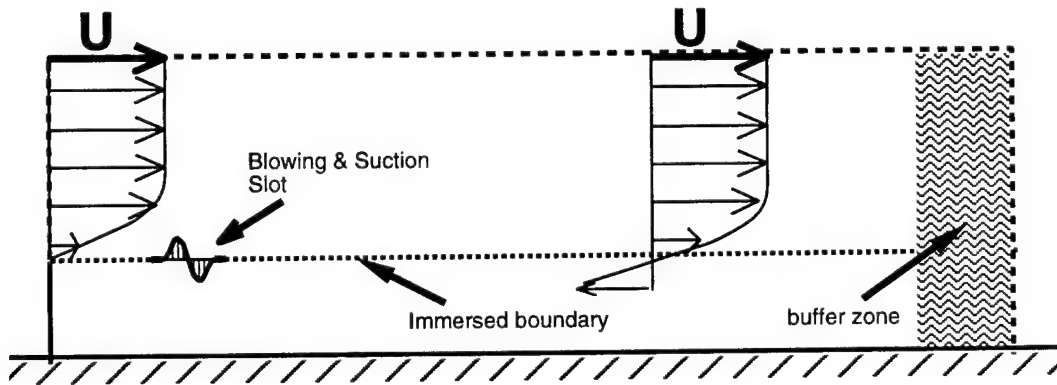
Figure 2: A flat plate immersed in a rectangular computational domain.
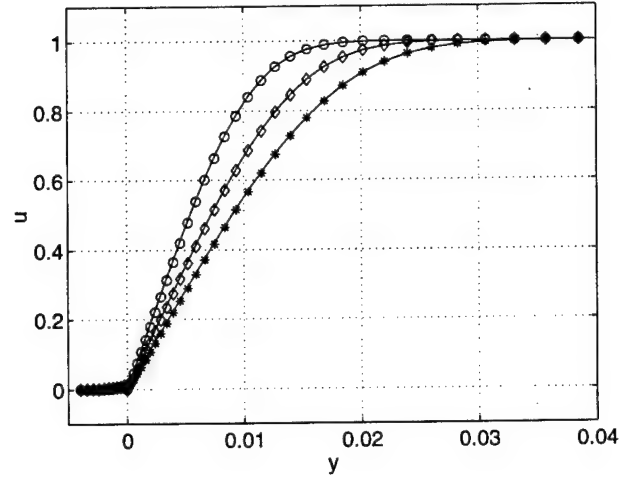
Figure 3: Comparison of u-velocity boundary layers at several downstream locations: $x = 1.213$ $(R_{\delta_1} = 600)$ (○), $x = 2.158$ $(R_{\delta_1} = 800)$ (◇), and $x = 3.375$ $(R_{\delta_1} = 1000)$ (∗). Symbols indicate values computed using a virtual wall located at $y = 0$.
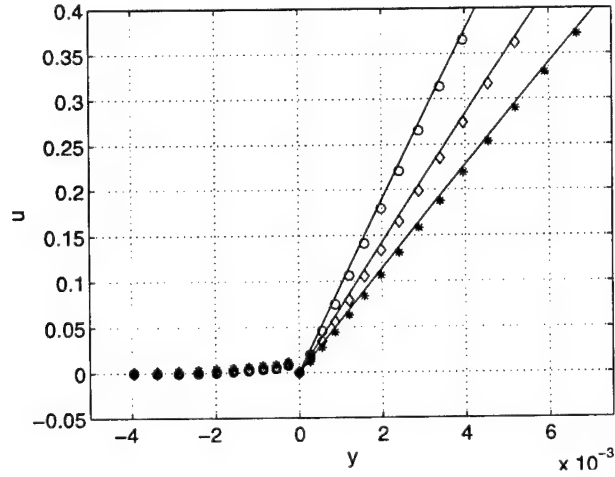
Figure 4: Zoom-in comparison of u-velocity boundary layers at several downstream locations: $x = 1.213$ $(R_{\delta_1} = 600)$ (○), $x = 2.158$ $(R_{\delta_1} = 800)$ (◇), and $x = 3.375$ $(R_{\delta_1} = 1000)$ (∗). Symbols indicate values computed using a virtual wall located at $y = 0$.

41
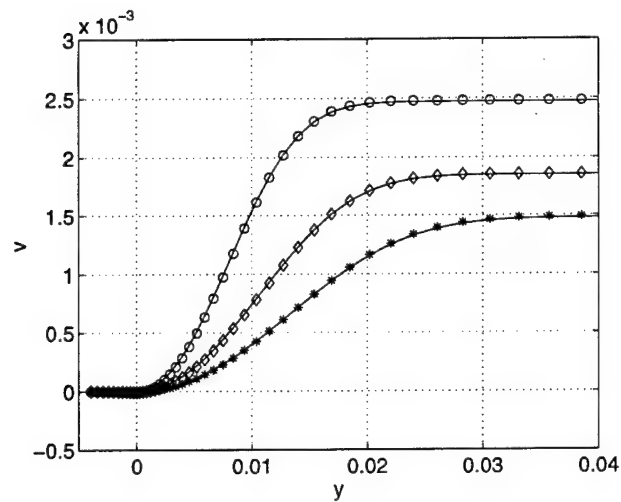
Figure 5: Comparison of v-velocity boundary layers at several downstream locations: $x = 1.213$ $(R_{\delta_1} = 600)$ (o), $x = 2.158$ $(R_{\delta_1} = 800)$ (◇), and $x = 3.375$ $(R_{\delta_1} = 1000)$ (∗). Symbols indicate values computed using a virtual wall located at $y = 0$.
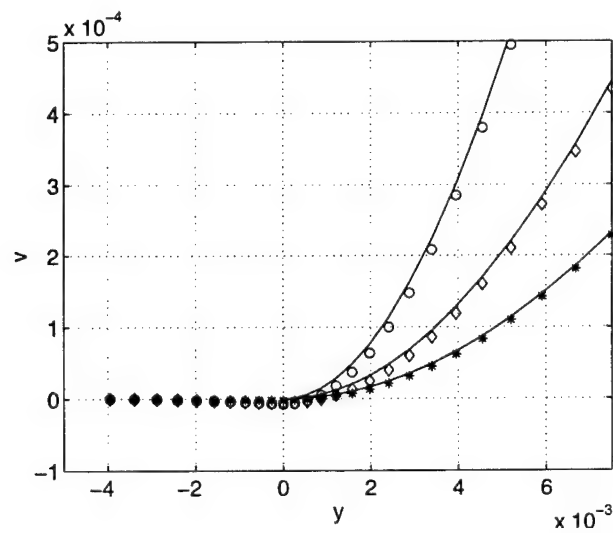
Figure 6: Zoom-in comparison of v-velocity boundary layers at several downstream locations: $x = 1.213$ $(R_{\delta_1} = 600)$ (o), $x = 2.158$ $(R_{\delta_1} = 800)$ (◇), and $x = 3.375$ $(R_{\delta_1} = 1000)$ (∗). Symbols indicate values computed using a virtual wall located at $y = 0$.
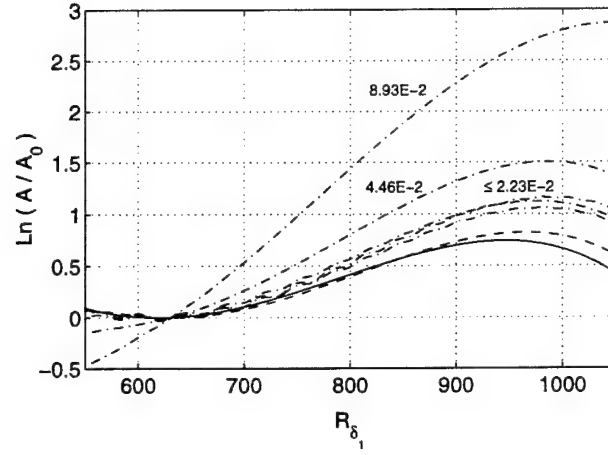
Figure 7: Comparison of growth rates of 2-D TS-waves over a virtual wall at $y = 0$ for various CFL numbers $(- \cdot -)$, compared with a standard DNS $(- - -)$, and with LST $(—)$. Note: CFL=$C\Delta t/\Delta x$, and Δx is held constant.
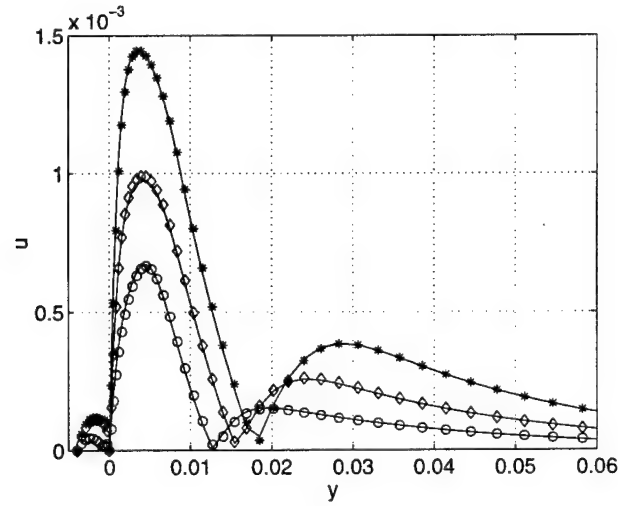
Figure 8: Comparison of u-velocity eigenfunctions at several downstream locations: $x = 1.213$ $(R_{\delta_1} = 600)$ $(\circ)$, $x = 2.158$ $(R_{\delta_1} = 800)$ $(\diamond)$, and $x = 3.375$ $(R_{\delta_1} = 1000)$ $(*)$. Symbols indicate values computed using a virtual wall located at $y = 0$.
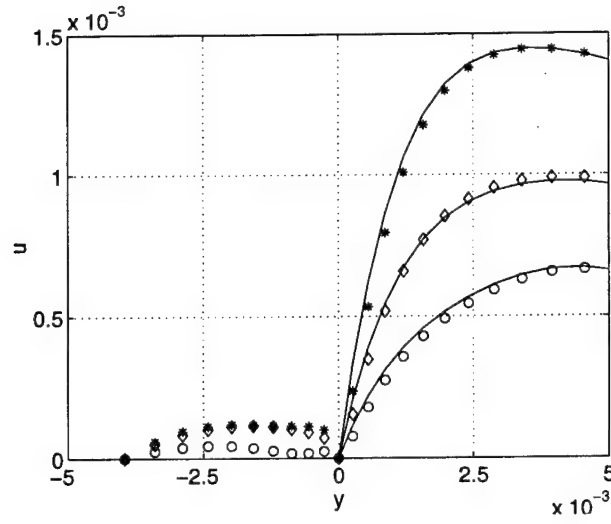
Figure 9: Zoom-in comparison of u-velocity eigenfunctions at several downstream locations: $x = 1.213$ ($R_{\delta_1} = 600$) (o), $x = 2.158$ ($R_{\delta_1} = 800$) ($\diamond$), and $x = 3.375$ ($R_{\delta_1} = 1000$) (*). Symbols indicate values computed using a virtual wall located at $y = 0$.
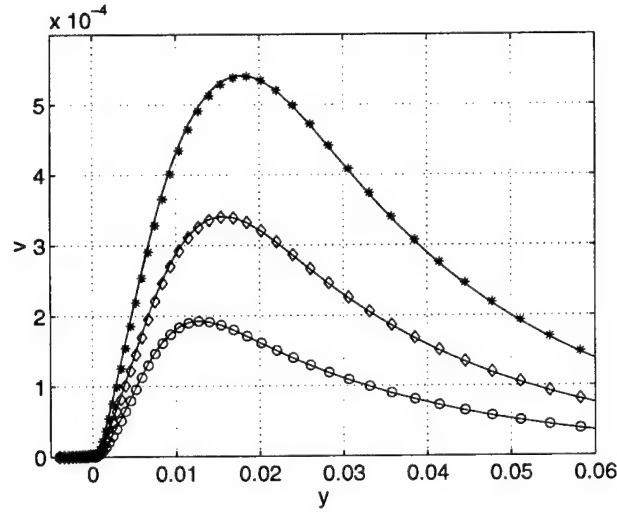
Figure 10: Comparison of v-velocity eigenfunctions at several downstream locations: $x = 1.213$ ($R_{\delta_1} = 600$) (o), $x = 2.158$ ($R_{\delta_1} = 800$) ($\diamond$), and $x = 3.375$ ($R_{\delta_1} = 1000$) (*). Symbols indicate values computed using a virtual wall located at $y = 0$.
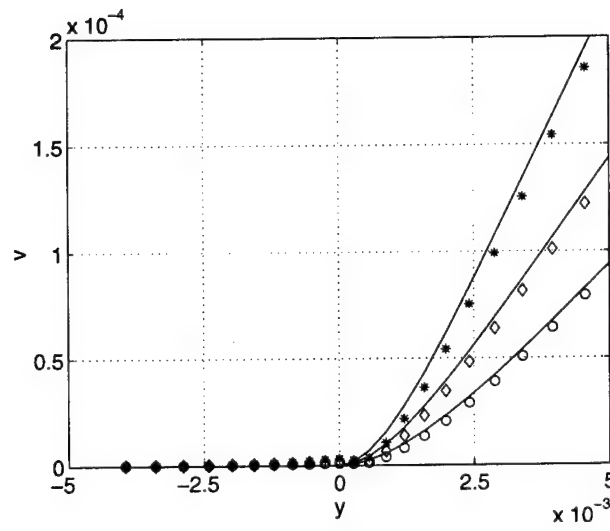
Figure 11: Zoom-in comparison of v-velocity eigenfunctions at several downstream locations: $x = 1.213$ ($R_{\delta_1} = 600$) (○), $x = 2.158$ ($R_{\delta_1} = 800$) (◇), and $x = 3.375$ ($R_{\delta_1} = 1000$) (∗). Symbols indicate values computed using a virtual wall located at $y = 0$.
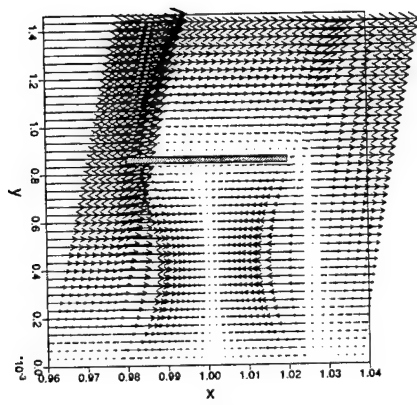
center stroke, moving upward
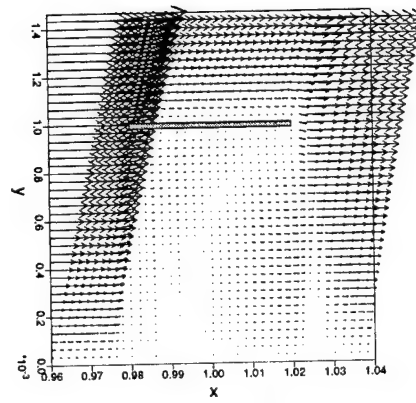
top stroke
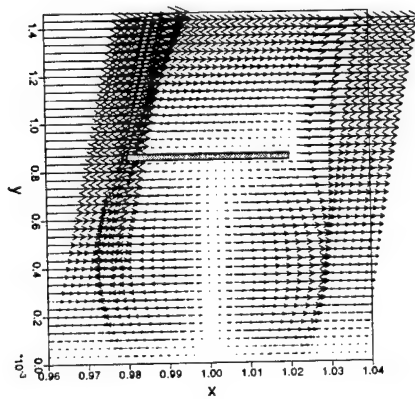
center stroke, moving downward
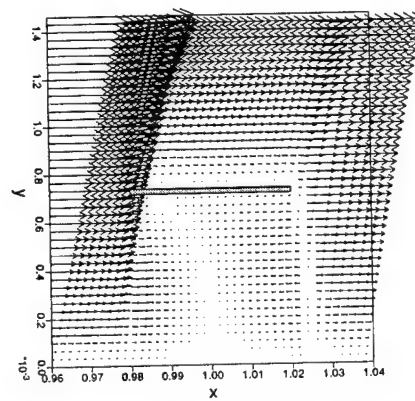
bottom stroke

Figure 12: Sinusoidal motion of a 2-D vibrating ribbon simulated inside the computational domain using volume forces. Total-velocity vector $\mathbf{U}_T = \mathbf{U}_B + \mathbf{U}$.
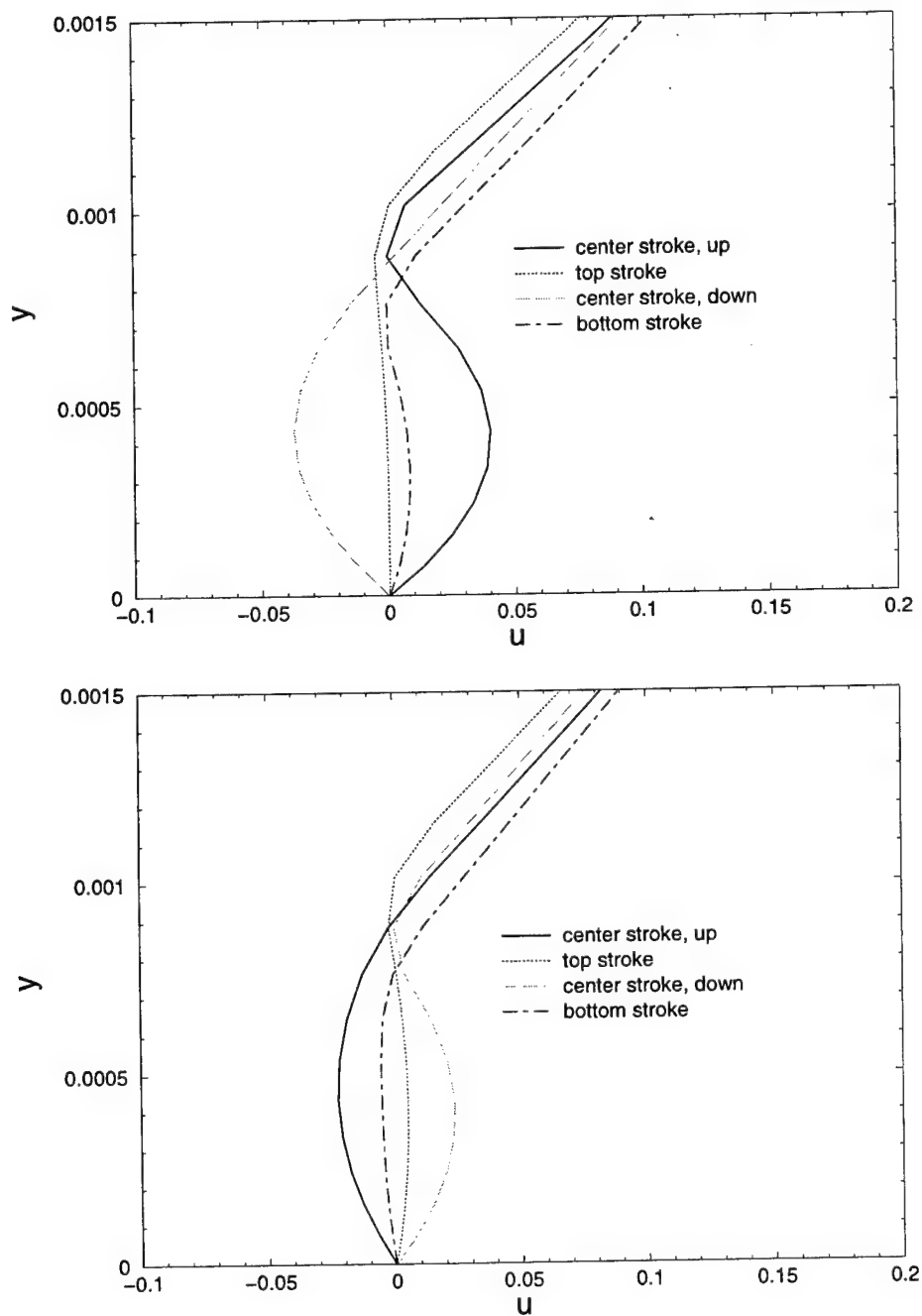
Figure 13: Streamwise velocity profiles u_T near the leading edge of the ribbon (upper graph) and the trailing edge (lower graph).
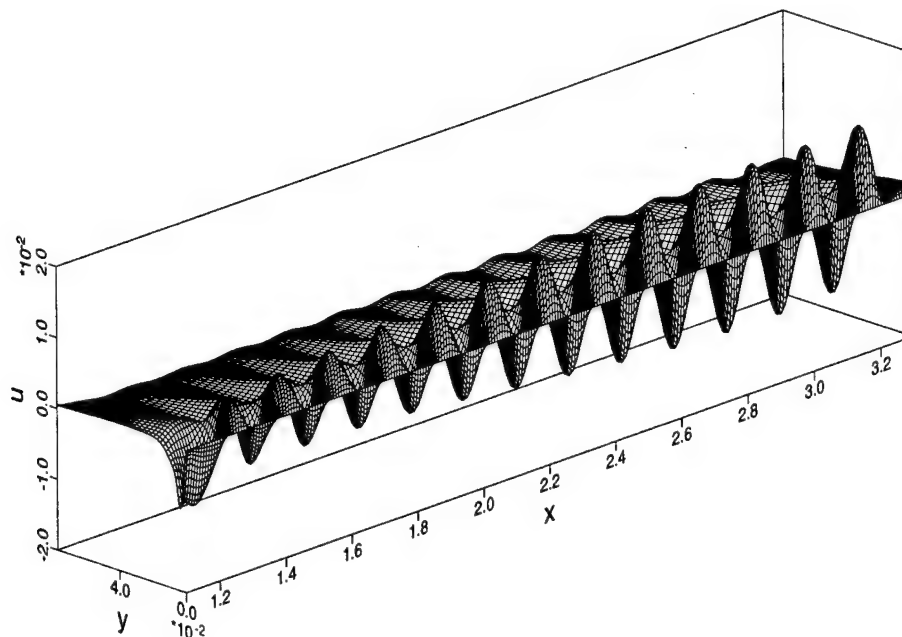
Figure 14: Streamwise disturbance velocity $u(x, y)$ produced by a vibrating ribbon. $U_\infty = 3.0 \ m/s$, $\nu = 1.5 \times 10^{-5}$, $Re_L = 10^5$, $F = 150 \times 10^{-6}$ or $f' = 14.3$ Hz.
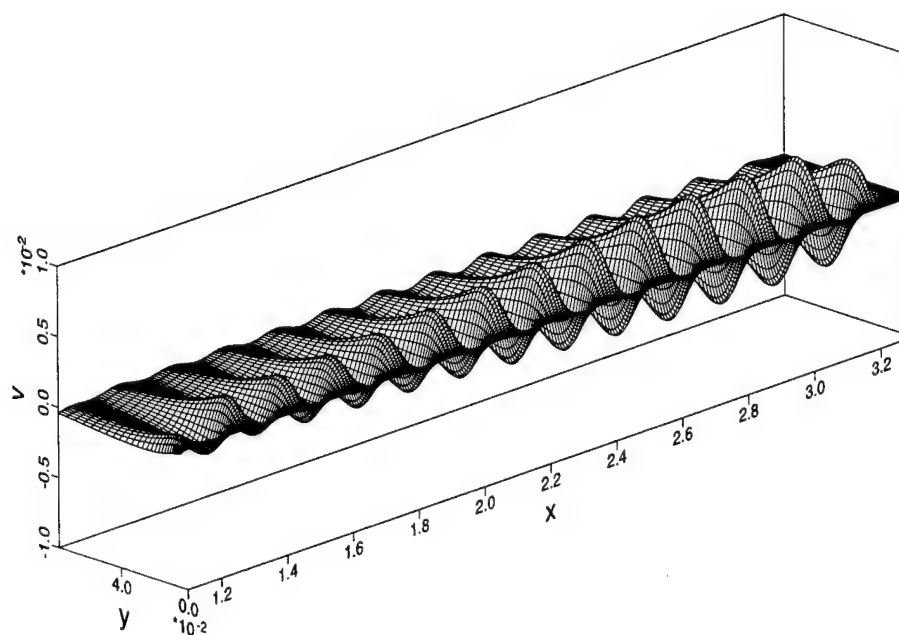
Figure 15: Wall normal disturbance velocity $v(x, y)$ produced by a vibrating ribbon. $U_\infty = 3.0 \ m/s$, $\nu = 1.5 \times 10^{-5}$, $Re_L = 10^5$, $F = 150 \times 10^{-6}$ or $f' = 14.3$ Hz.
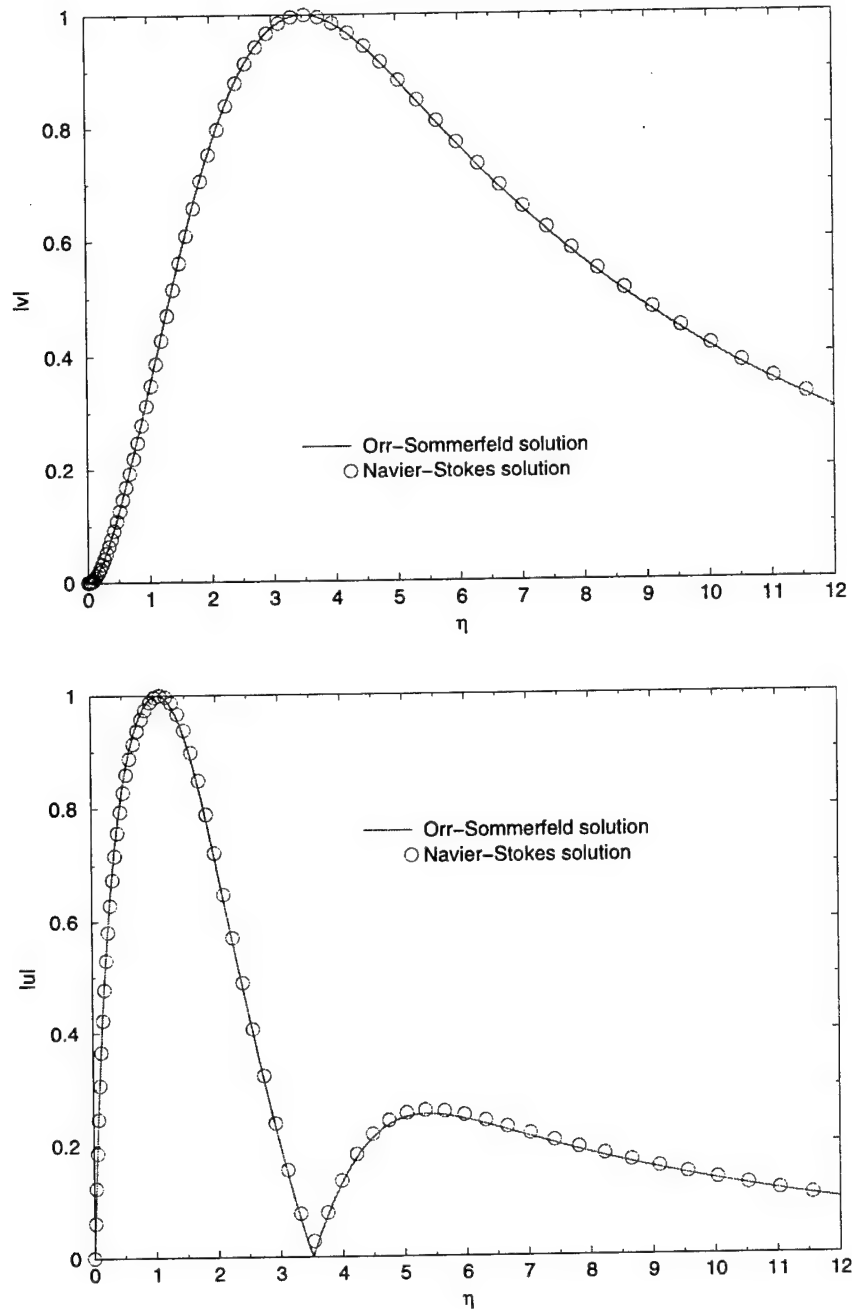
Figure 16: Wall normal v (upper graph) and streamwise u (lower graph) disturbance velocity. Navier-Stokes solution (fundamental) with volume forcing to simulate a vibrating ribbon, $\circ$, compared with Orr-Sommerfeld solution, —. $U_\infty = 3.0 \ m/s$, $\nu = 1.5 \times 10^{-5}$, $Re_L = 10^5$, $F = 150 \times 10^{-6}$ or $f' = 14.3$ Hz or $\omega = \frac{\omega' \delta_1}{U_\infty} = 0.099735$, $R_{\delta_1} = 666.0$, $\alpha = \alpha' \delta_1 = (0.266399, -0.002955)$.
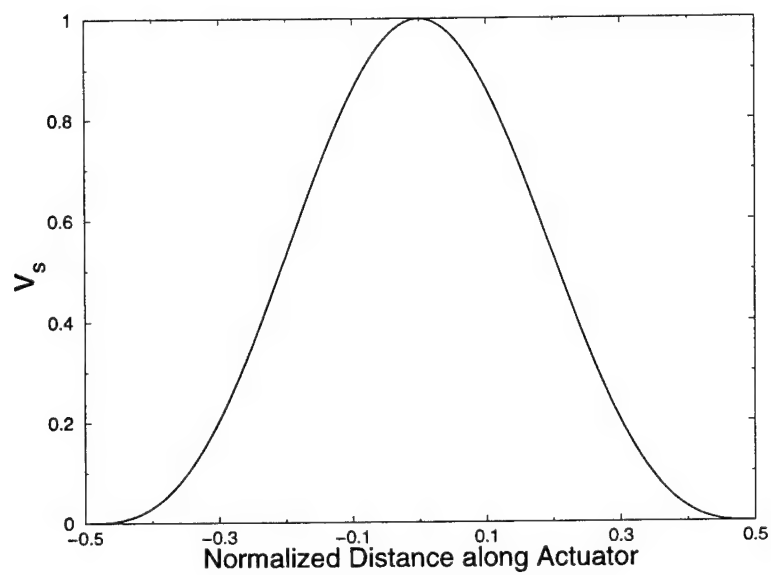
Figure 17: Envelope of wall mounted actuator movement. Curve is given by equation (81).
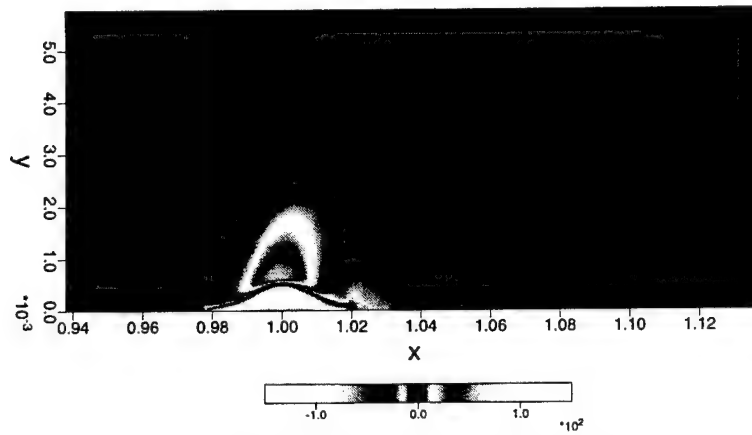
half stroke, moving upward
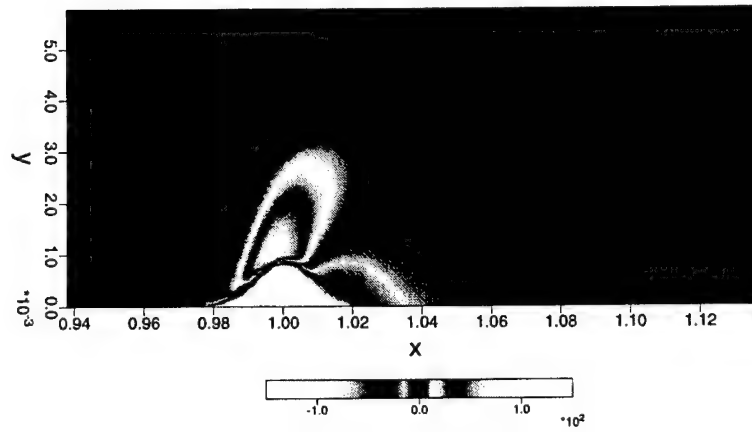
top stroke, stationary
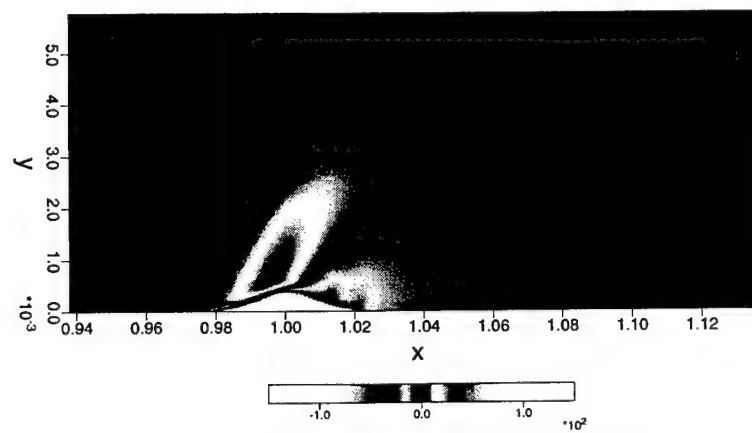
half stroke, moving downward

Figure 18: Disturbance vorticity created by the sinusoidal movement of a wall mounted actuator. Actuator height is 5.6% of boundary layer thickness δ.
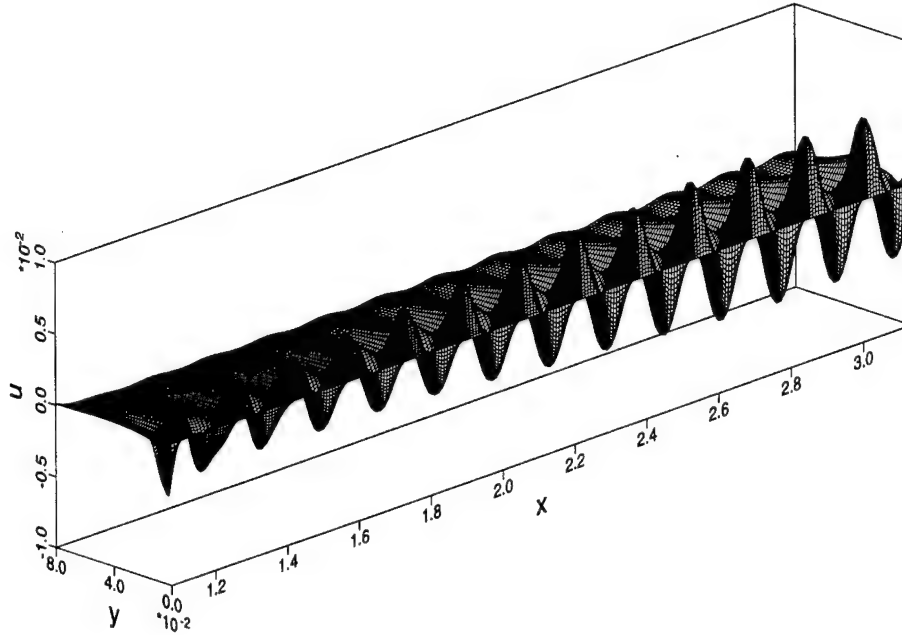
Figure 19: Streamwise disturbance velocity $u(x,y)$ produced by a wall mounted actuator. Actuator described by equation (81). $U_\infty = 3.0\,m/s$, $\nu = 1.5 \times 10^{-5}$, $Re_L = 10^5$, $F = 150 \times 10^{-6}$ or $f' = 14.3$ Hz.
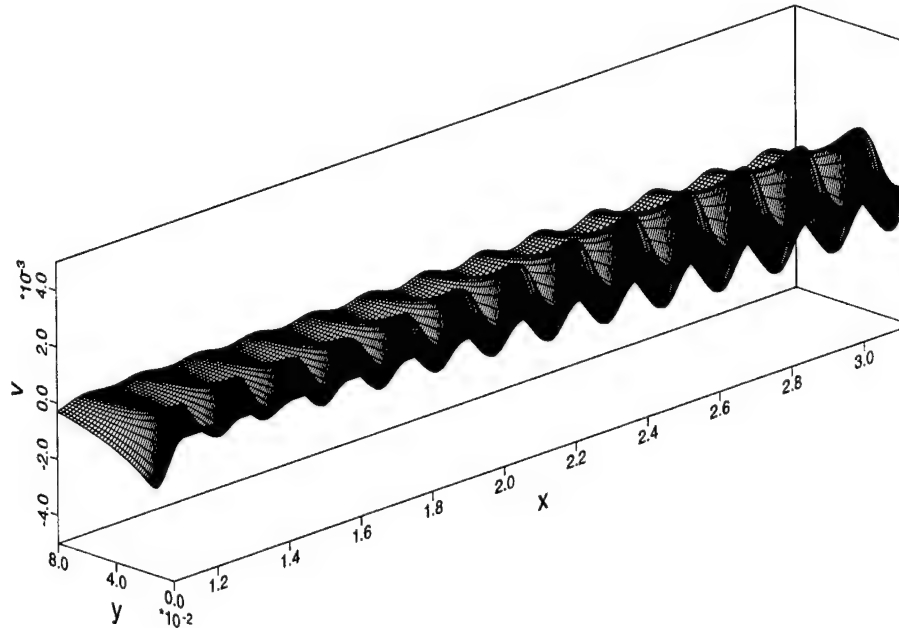
Figure 20: Wall normal disturbance velocity $v(x,y)$ produced by a wall mounted actuator. Actuator described by equation (81). $U_\infty = 3.0\,m/s$, $\nu = 1.5 \times 10^{-5}$, $Re_L = 10^5$, $F = 150 \times 10^{-6}$ or $f' = 14.3$ Hz.
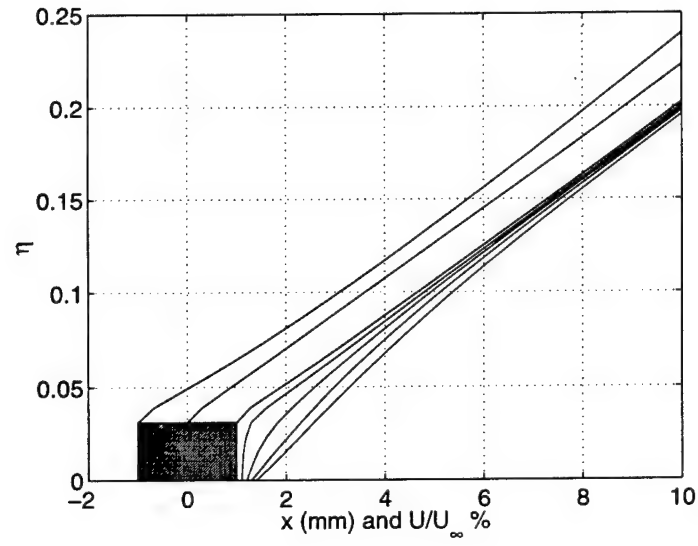
Figure 21: U-velocity profiles at $z = 0$ in vicinity of stationary piston.
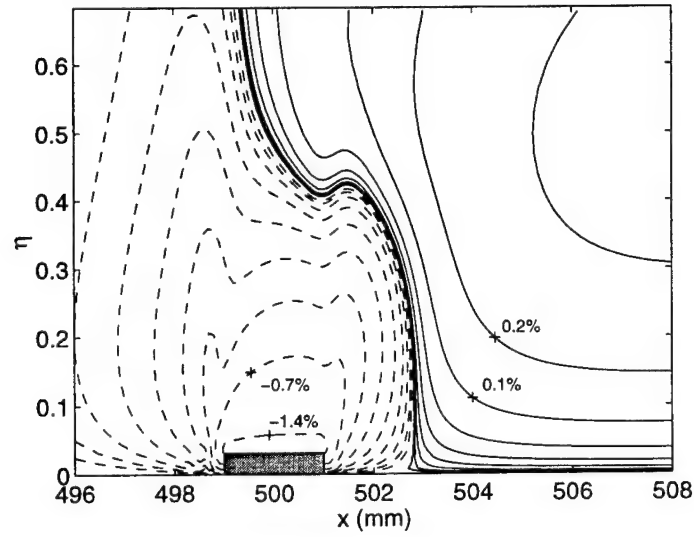
Figure 22: Contours of constant u-disturbance velocity, u/U_∞ %, at $z = 0$ created by a stationary piston actuator.
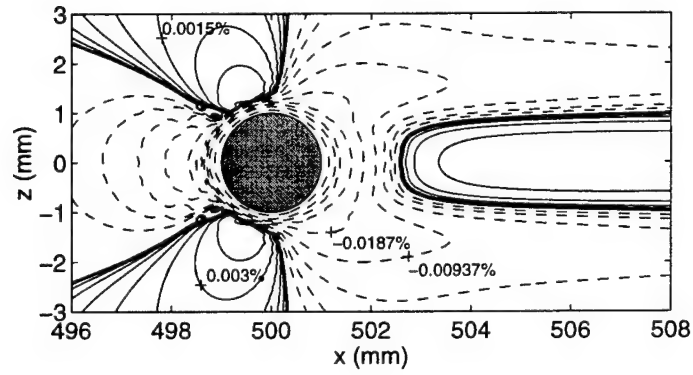
Figure 23: Contours of constant u-disturbance velocity, u/U_∞ %, in plane $y = 22$ μm created by a stationary piston actuator.
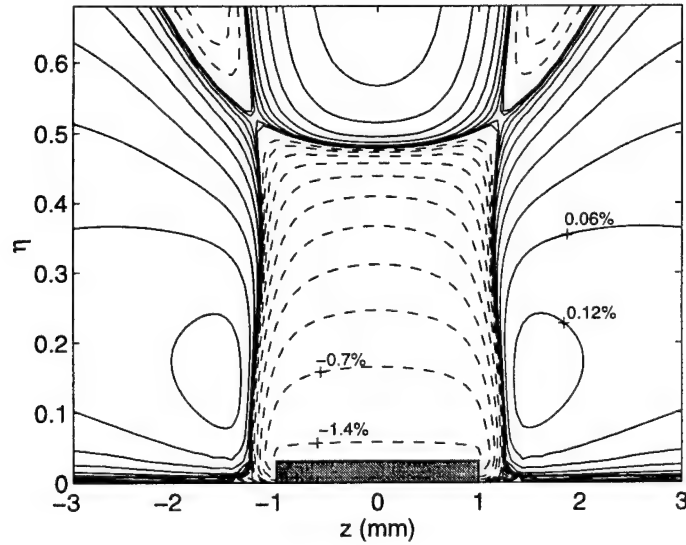
Figure 24: Contours of constant u-disturbance velocity, u/U_∞ %, in plane $x = 500$mm created by a stationary piston actuator.

bottom stroke, moving upward

half stroke, moving upward

top stroke, moving downward

half stroke, moving downward
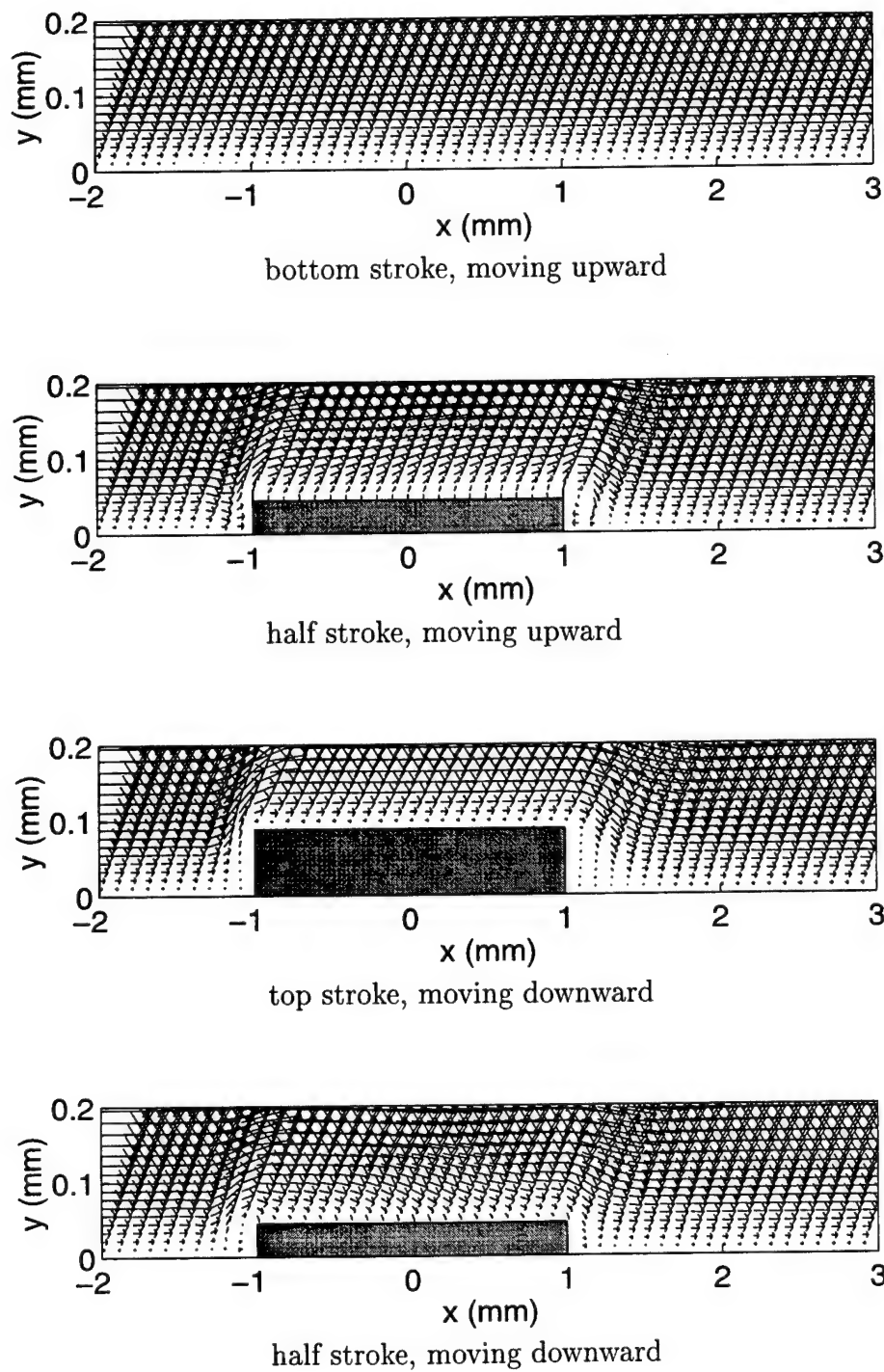
Figure 25: Velocity field created by the sinusoidal motion of a piston actuator. The actuator is flush with the wall at the bottom of its stroke.
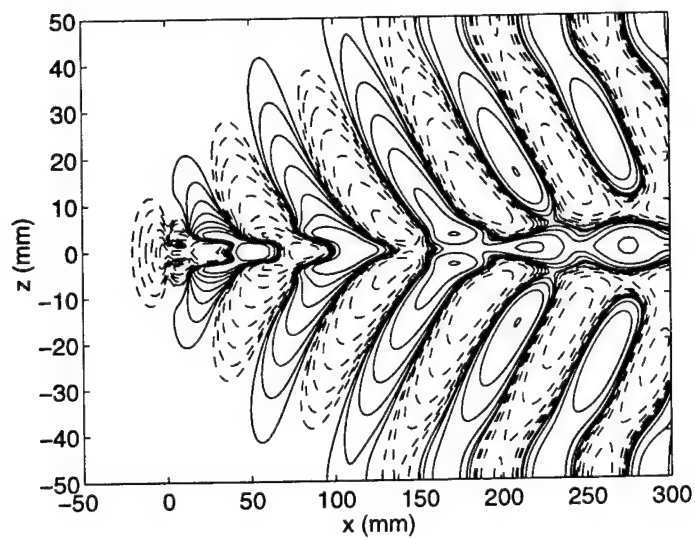
Figure 26: Contours of constant u-disturbance velocity in x-z created by the sinusoidal motion of a piston actuator.
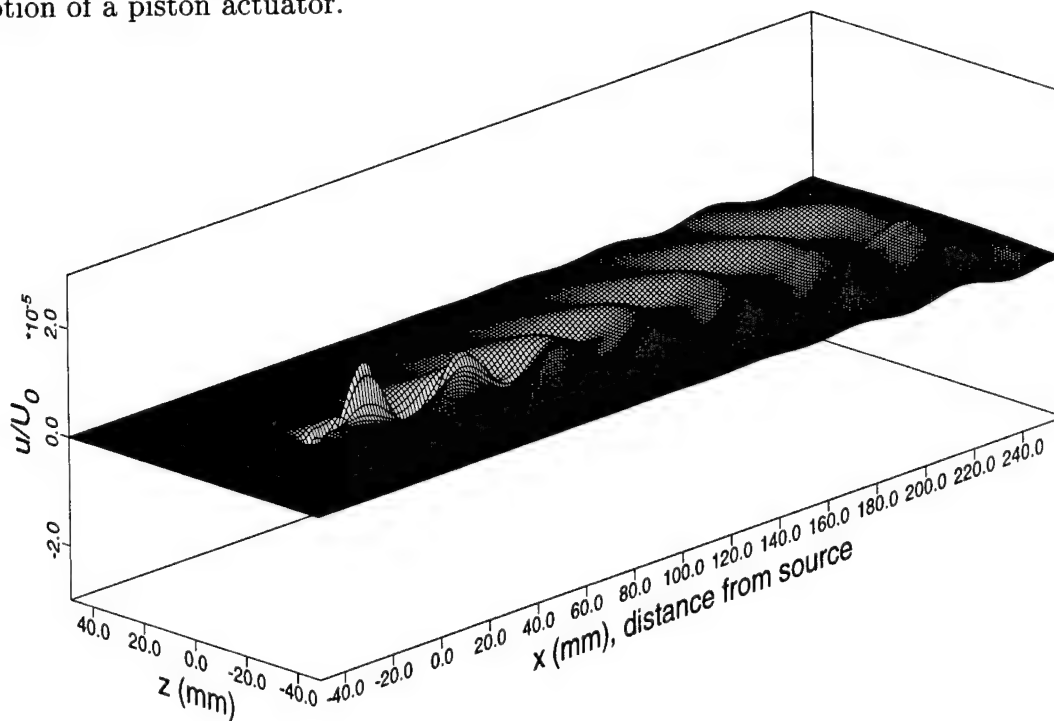
Figure 27: Streamwise disturbance velocity $u(x, z)$ in the z-x plane at $y = 1.49$ mm (35 % of boundary layer thickness at source) created by an oscillating jet normal to the surface.
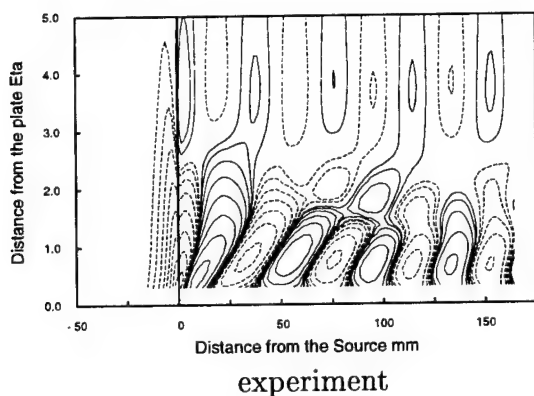
x-y plane at $z = 0$ z-y plane at $x = 100$ mm from source

experiment   experiment

theory   theory

DNS   DNS
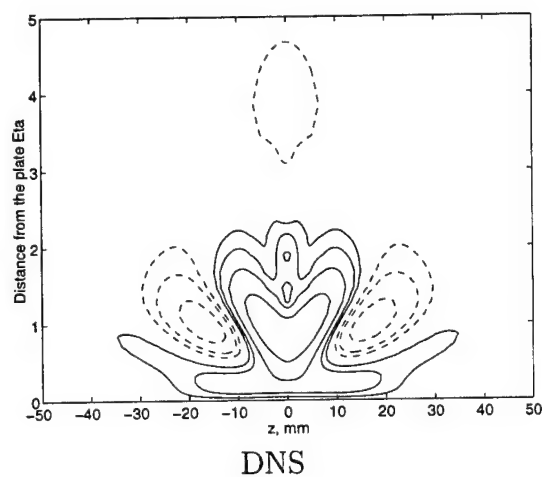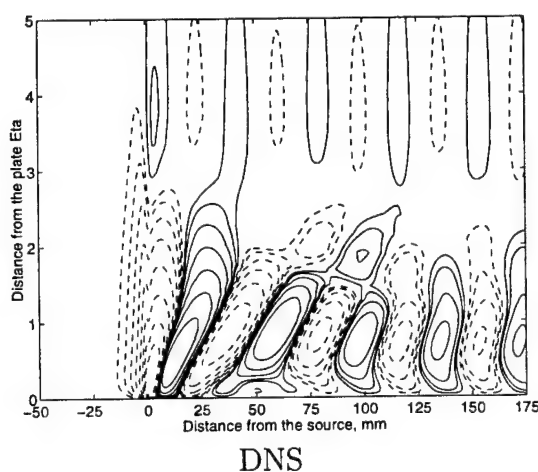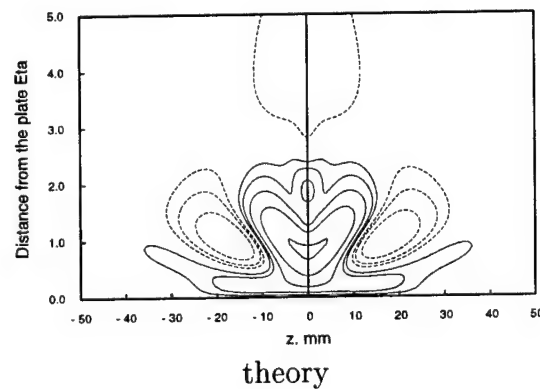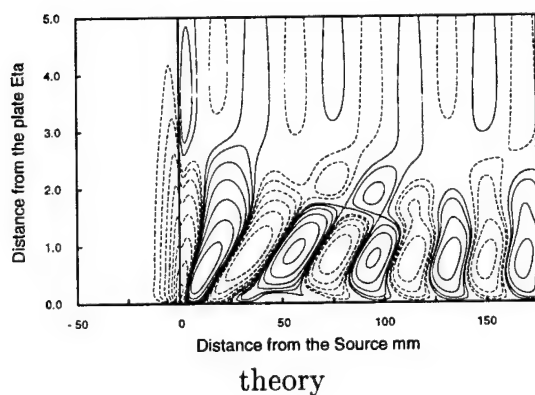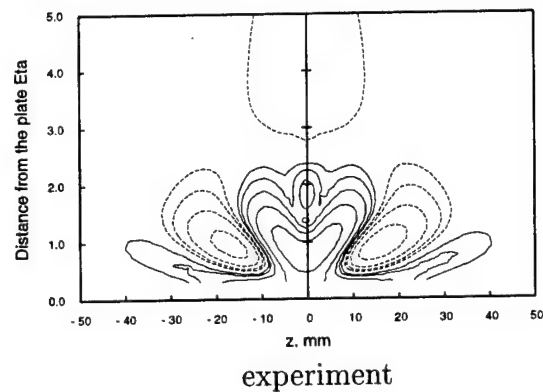
Figure 28: Oscillating jet normal to the surface over which a Blasius boundary layer has formed (U_∞=10m/s, $\nu = 1.4736 \times 10^{-5}$). The jet is located 500 mm from the leading edge of the plate, has a 2 mm diameter, and oscillates at 96 Hz with a mean velocity amplitude of 0.1 m/s. Contours of constant streamwise (u) disturbance velocity are shown in all figures.
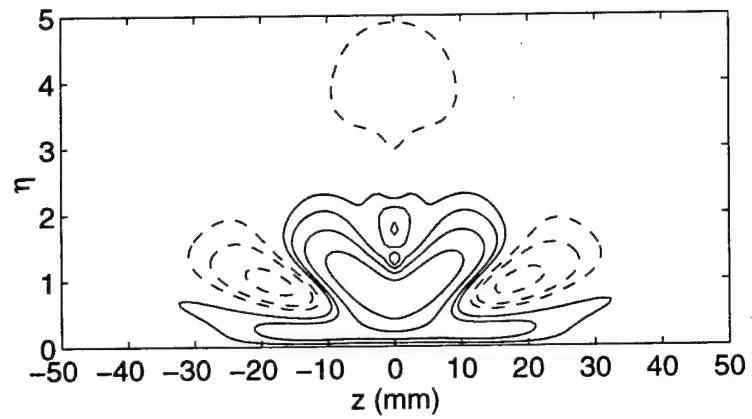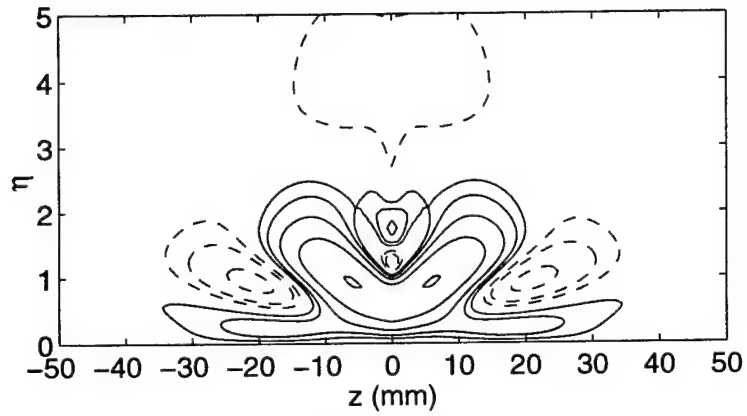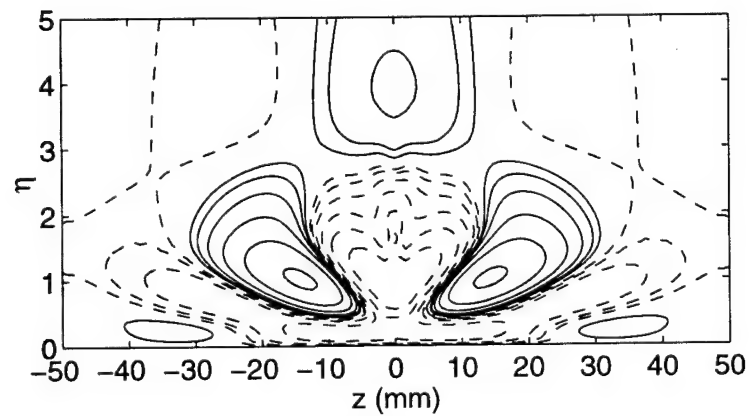
Figure 29: DNS computations for comparison with figure 7.0.1.
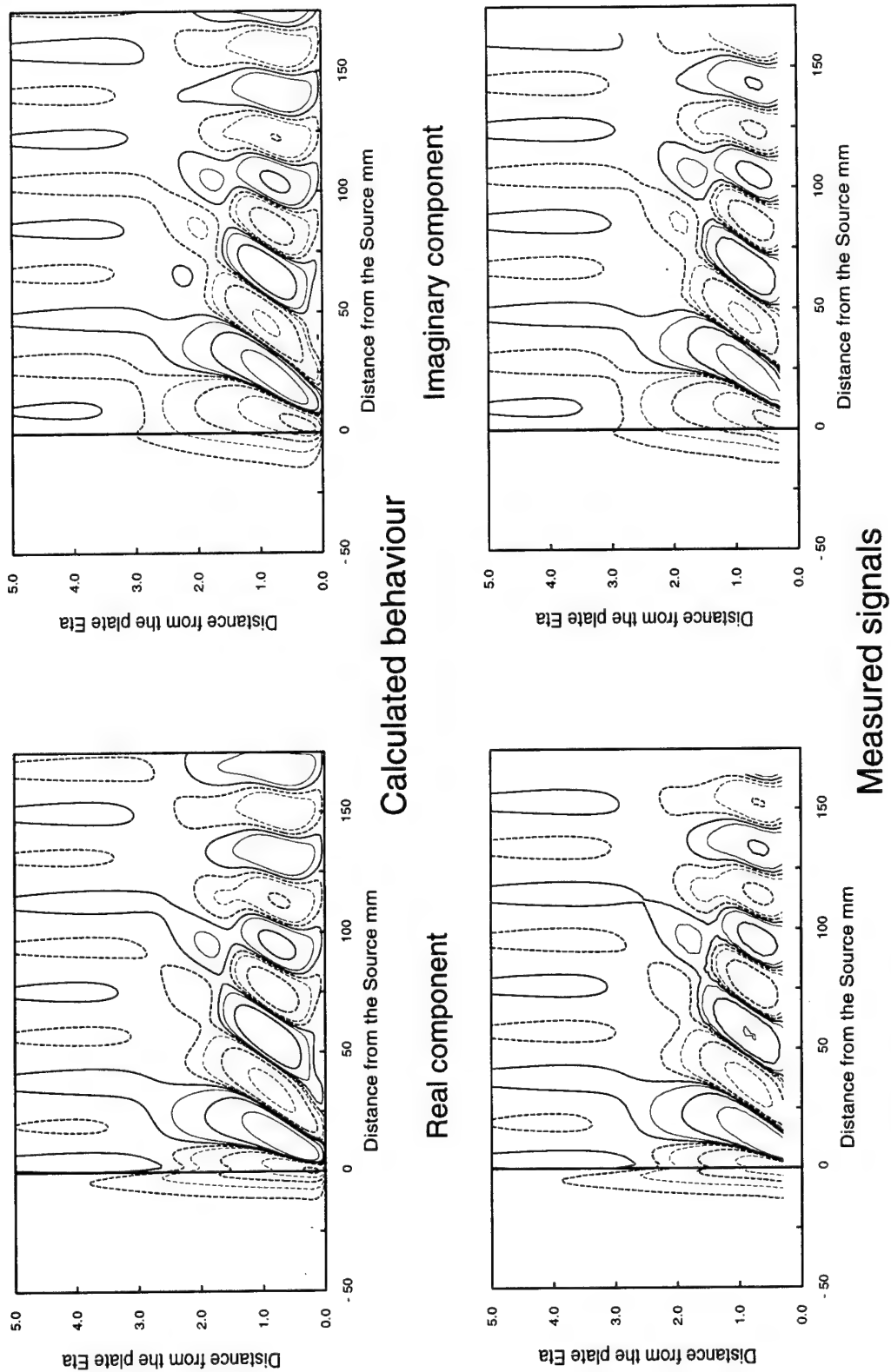
Figure 2.2.1.1 u Perturbation on Z = 0

Calculated behaviour

Modulus

Real component

Measured signals
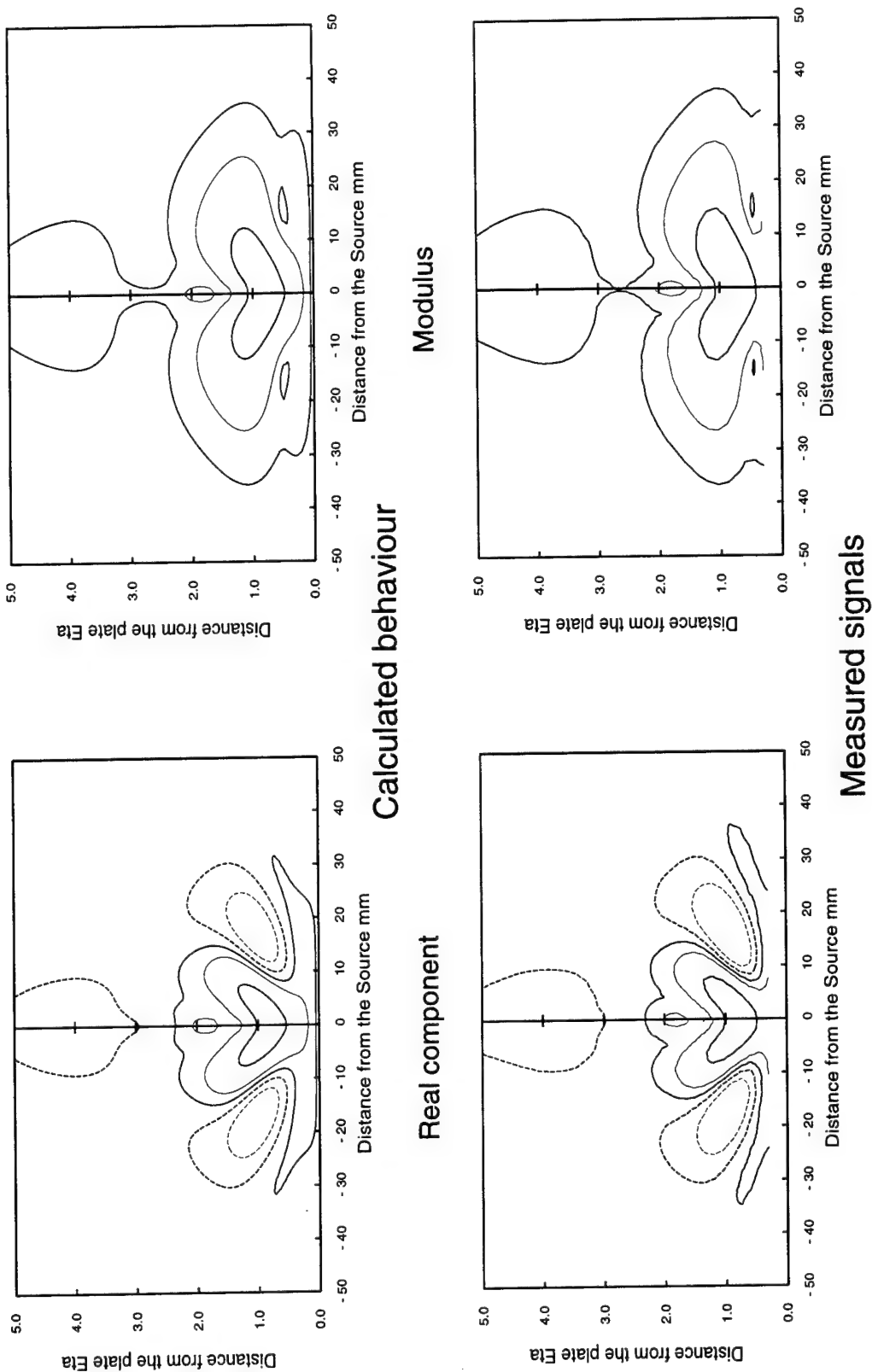
Figure 2.2.1.2 u Perturbation 100 mm from the Source

59

Calculated behaviour

Modulus

Real component

Measured signals
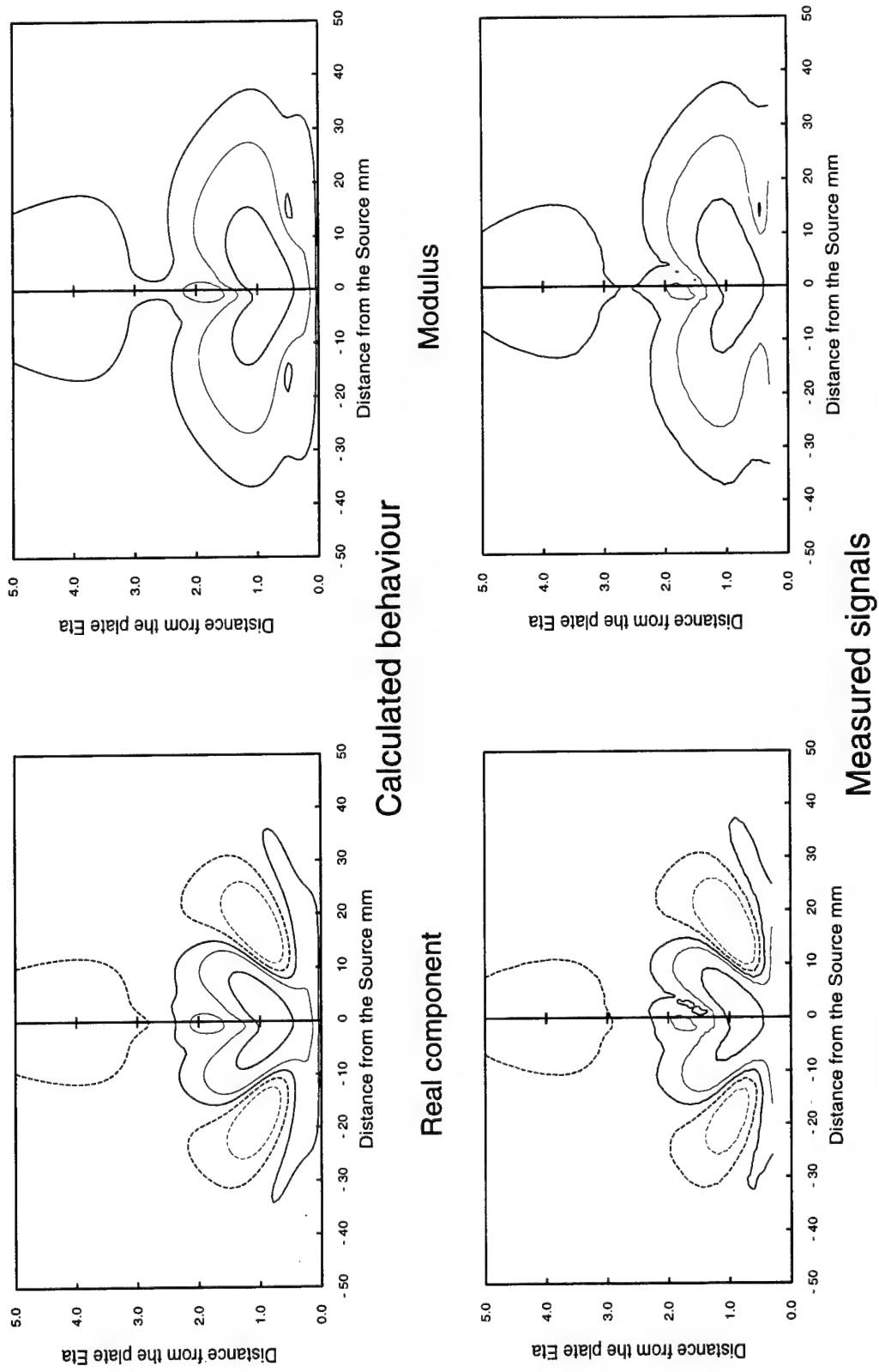
Figure 2.2.2 Jet aligned 30 degrees Spanwise
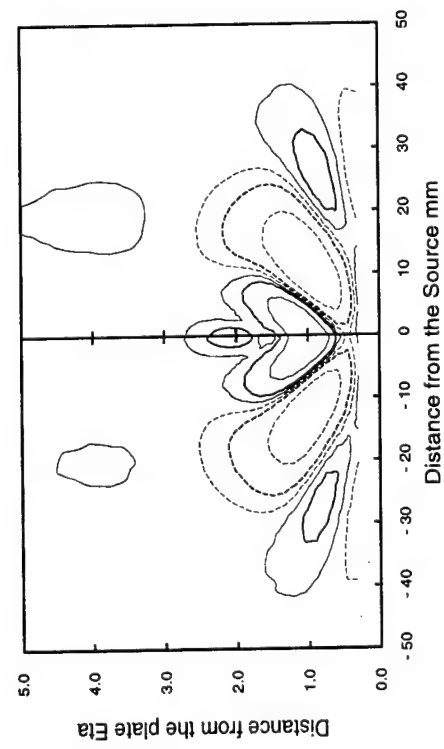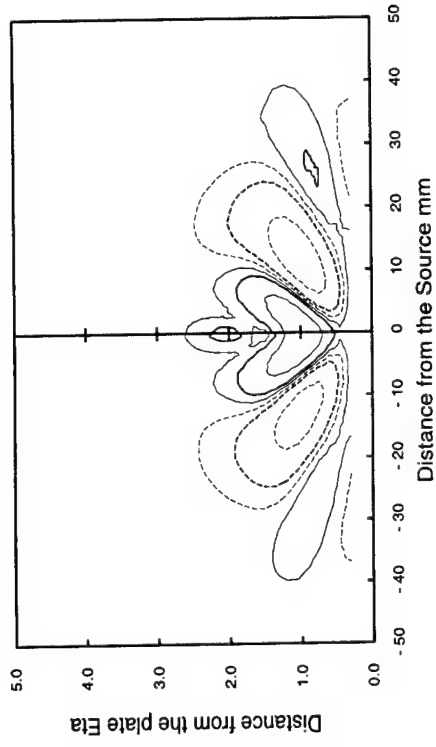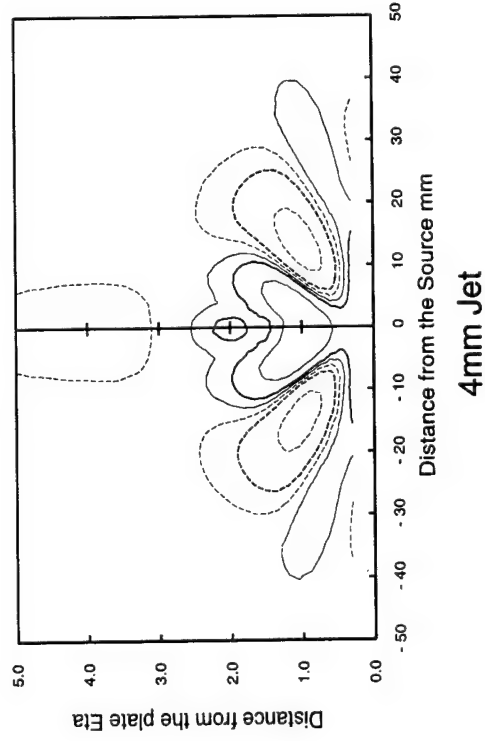
Periodic jets of constant mass flow

Frequency of excitation = 96 Hz

Free-Stream velocity = 10.8 m/s

Spanwise traverse 100mm downstream

Lowest contour at 0.00032% Uinf

Figure 2.2.3 Effect of Jet Diameter

Spanwise slice at X = 200 deltastar

Distance from the plate

Distance from the Centre-line (deltastar)

Center-Line Z = 0

Distance from the plate

Distance from the Source (deltastar)

Slice at Y = 0.5 deltastar

Distance across the span

Distance from the source (deltastar)

Excitation by a periodic u component

Reynolds number (deltastar) = 1000.0

Fnumber = 100E-6

Falkner-Skan parameter = 0.0

Lowest contour 0.0001

Figure 3.1.1(i) Contours of the u perturbation
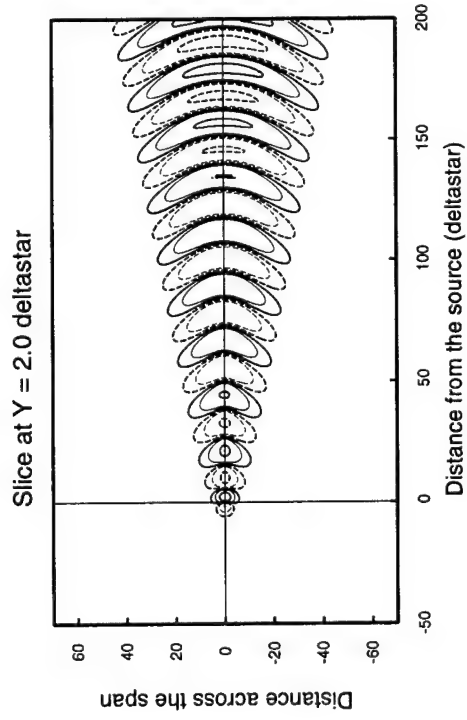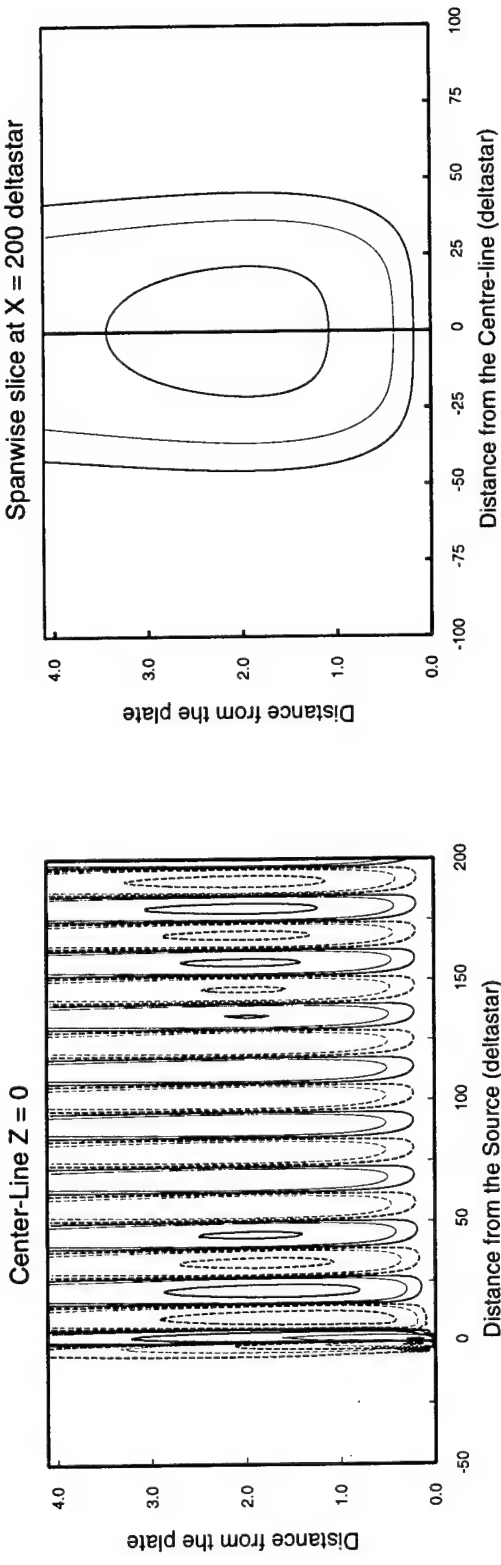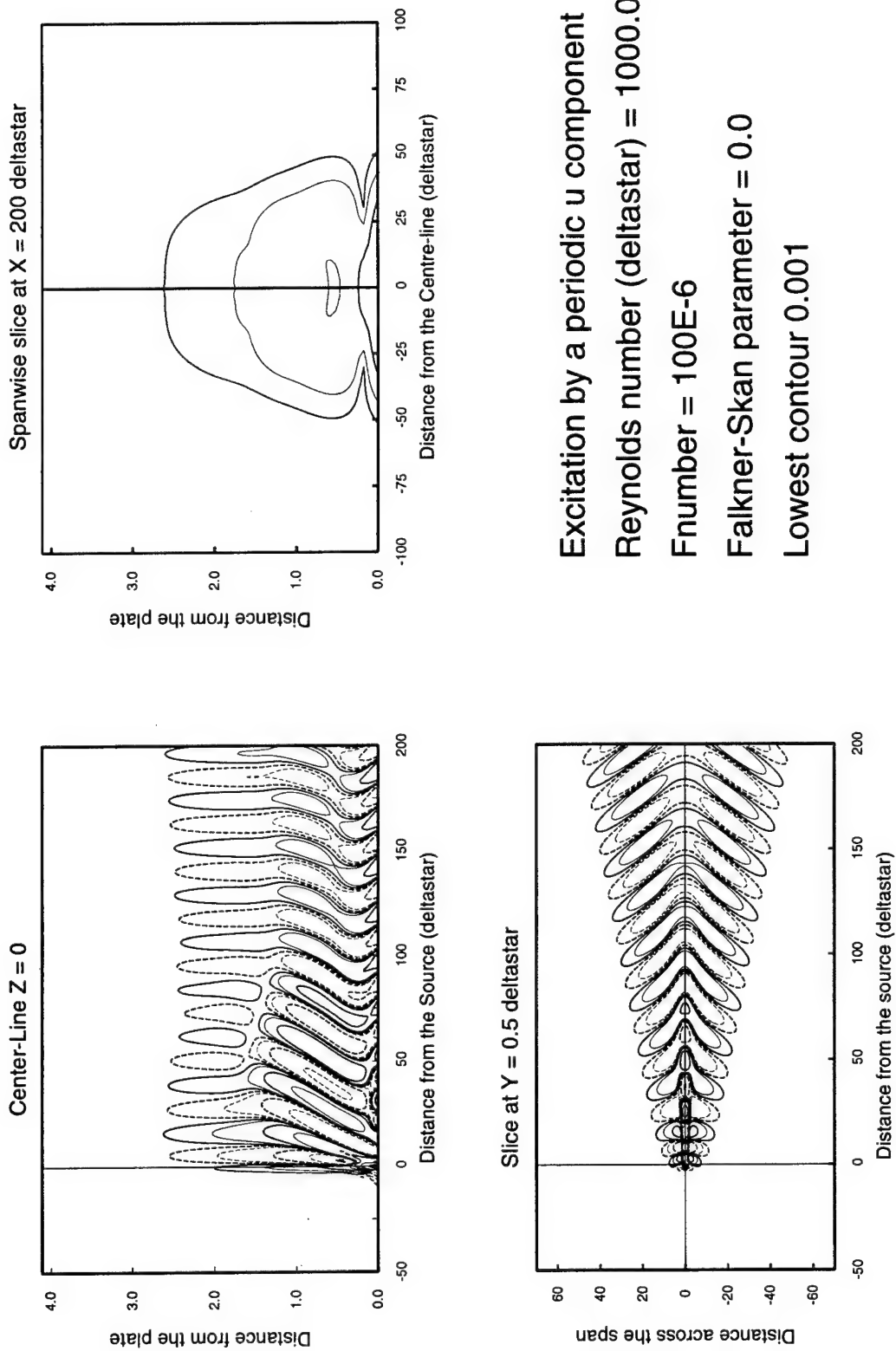
Spanwise slice at X = 200 deltastar

Distance from the plate

Distance from the Centre-line (deltastar)

Center-Line Z = 0

Distance from the plate

Distance from the Source (deltastar)

Slice at Y = 2.0 deltastar

Distance across the span

Distance from the source (deltastar)

Excitation by a periodic u component

Reynolds number (deltastar) = 1000.0

Fnumber = 100E-6

Falkner-Skan parameter = 0.0

Lowest contour 0.0001

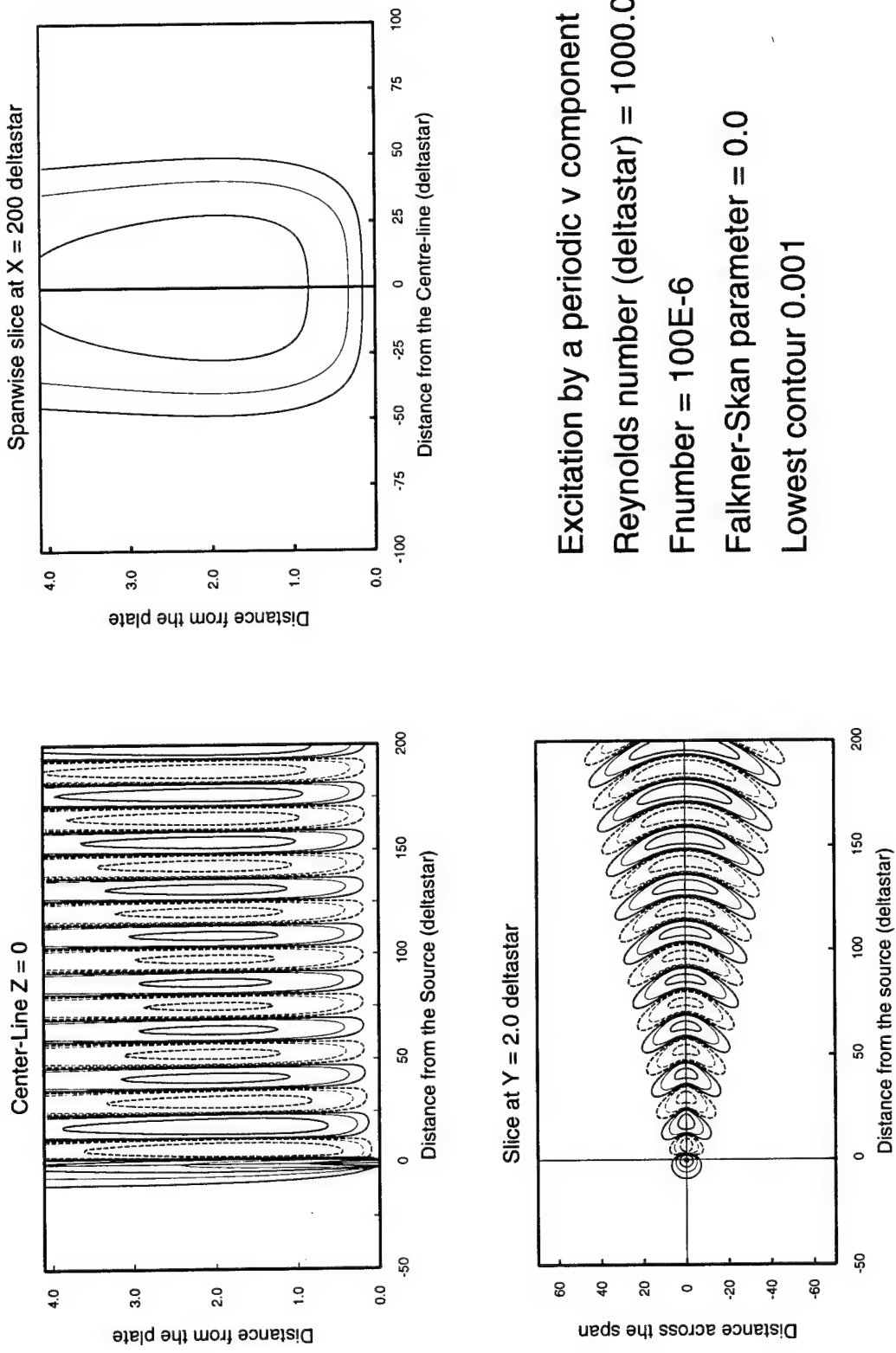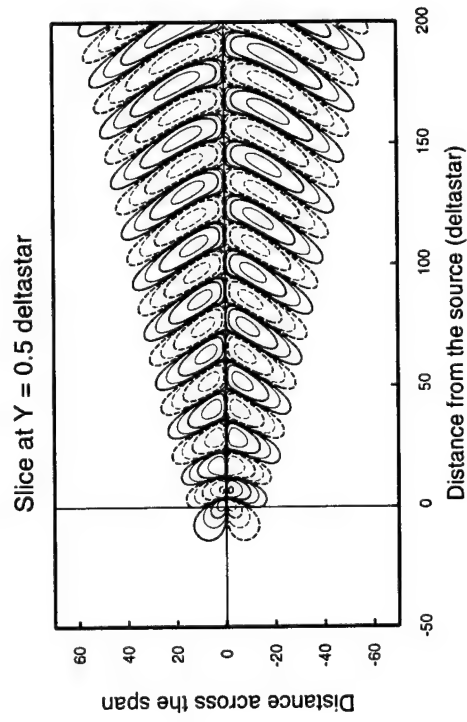Figure 3.1.1(ii) Contours of the v perturbation

Spanwise slice at X = 200 deltastar

Z = 25 deltastar

Slice at Y = 0.5 deltastar

Excitation by a periodic u component

Reynolds number (deltastar) = 1000.0

Fnumber = 100E-6

Falkner-Skan parameter = 0.0

Lowest contour 0.0001
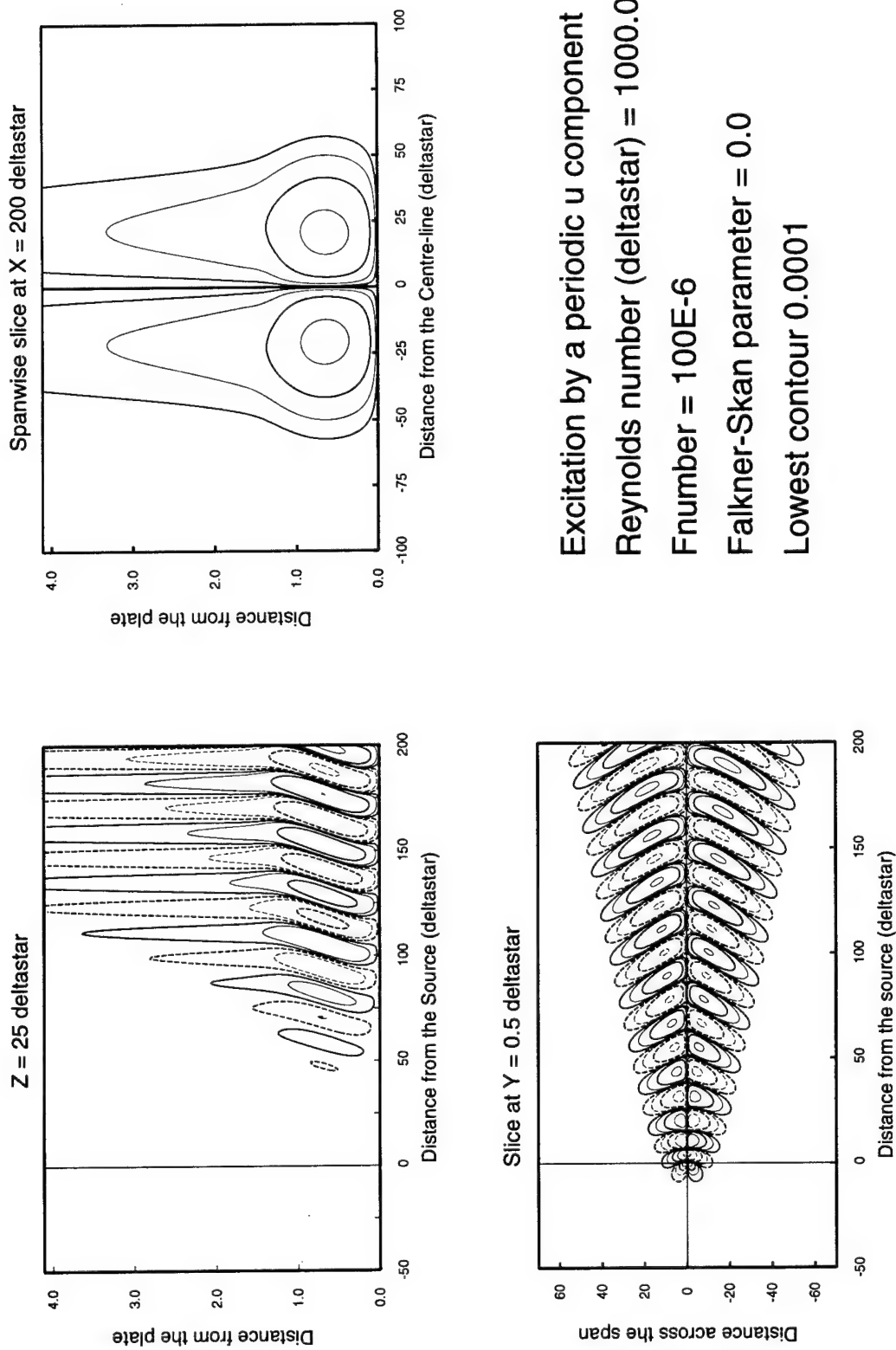
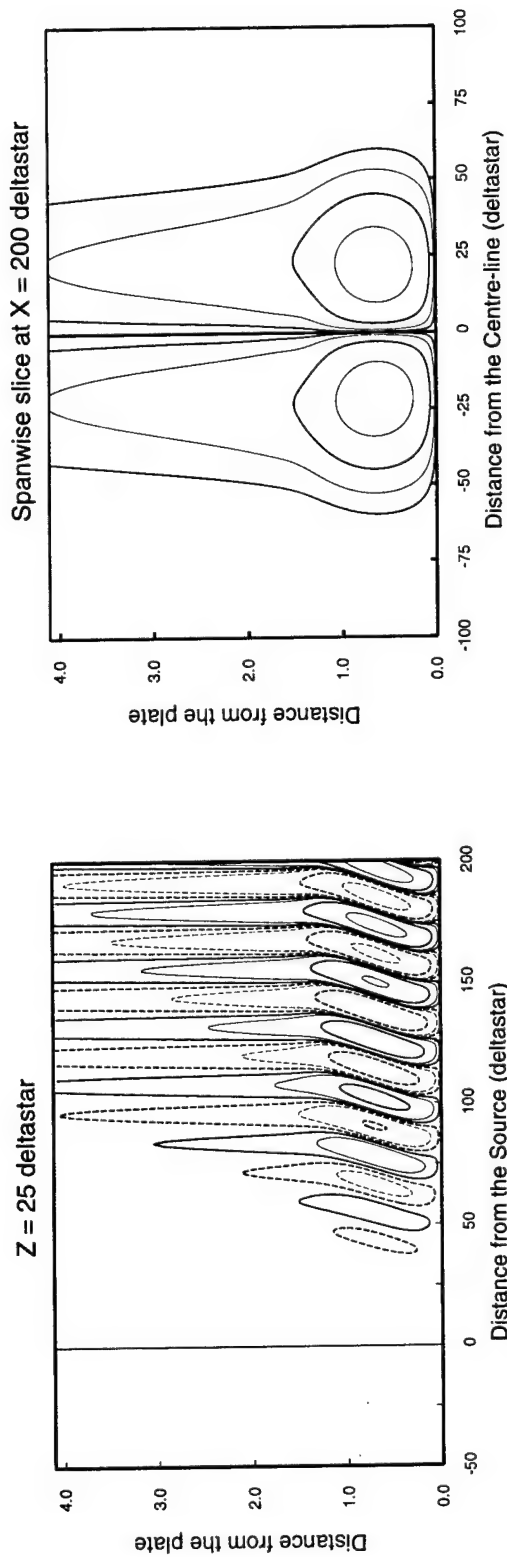Figure 3.1.1(iii) Contours of the w perturbation
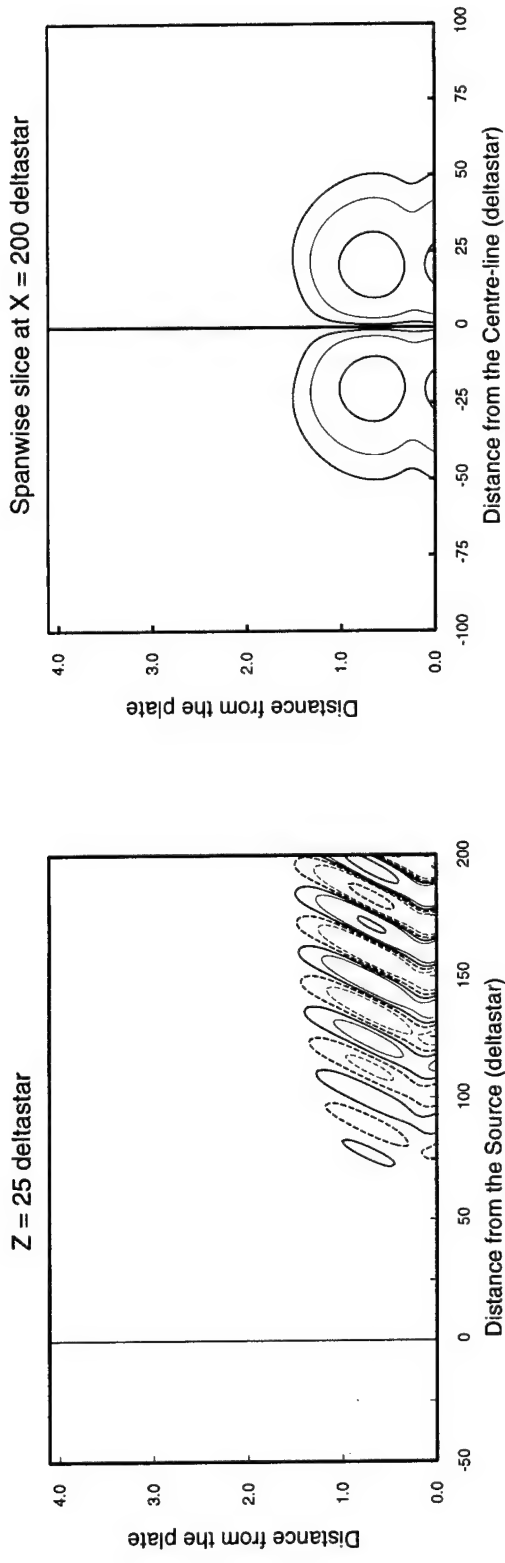
Spanwise slice at X = 200 deltastar

Z = 25 deltastar

Slice at Y = 0.5 deltastar

Excitation by a periodic u component
Reynolds number (deltastar) = 1000.0
Fnumber = 100E-6
Falkner-Skan parameter = 0.0
Lowest contour 0.001

Figure 3.1.1(iv) Contours of Streamwise Vorticity
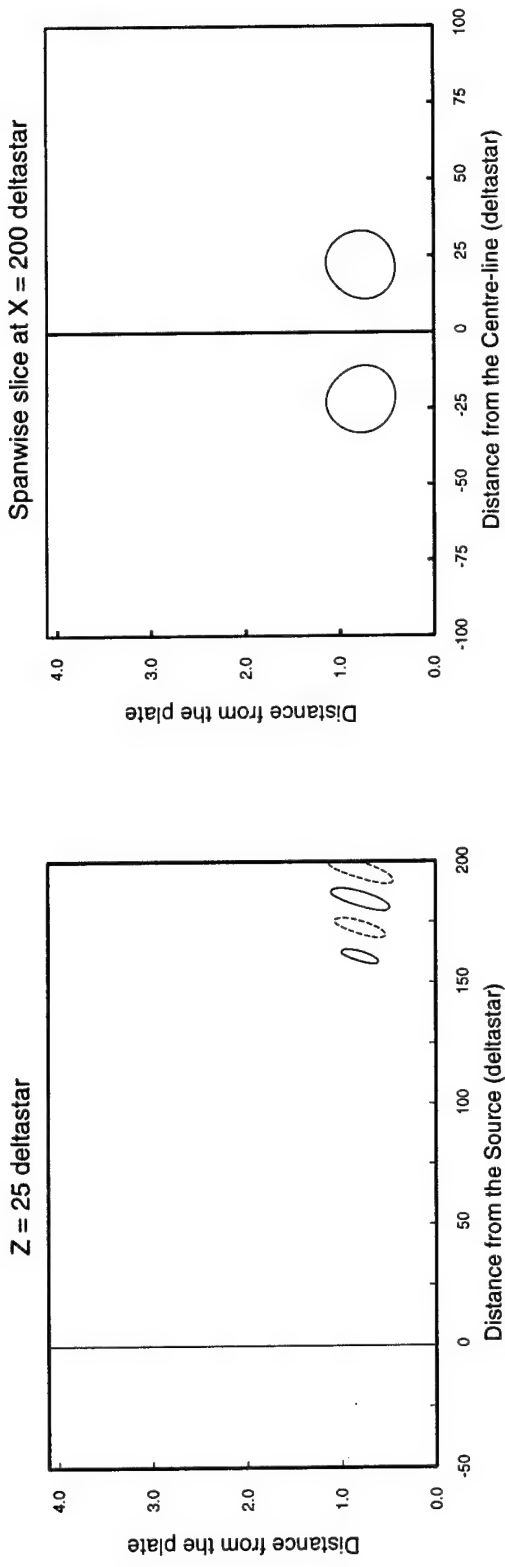
65

Spanwise slice at X = 200 deltastar

Z = 25 deltastar

Slice at Y = 0.5 deltastar

Excitation by a periodic u component

Reynolds number (deltastar) = 1000.0

Fnumber = 100E-6

Falkner-Skan parameter = 0.0
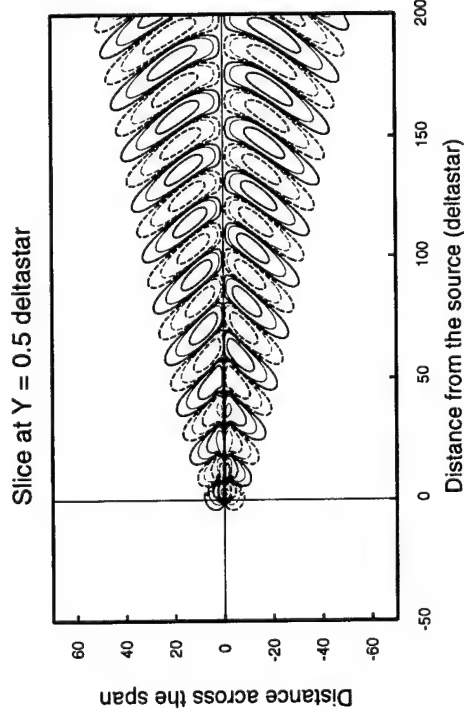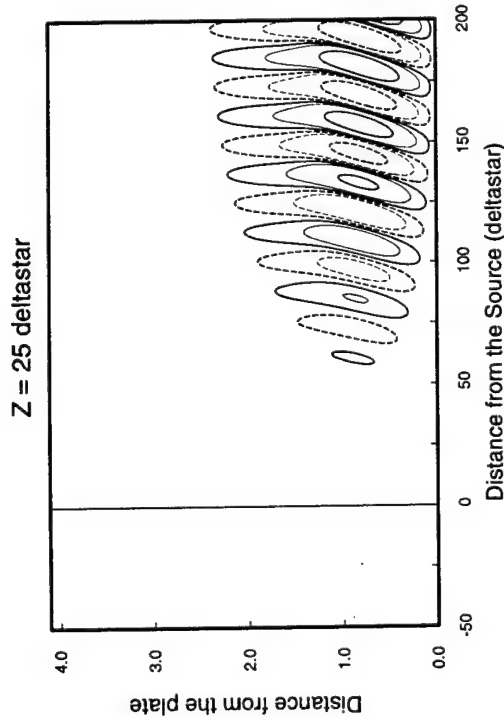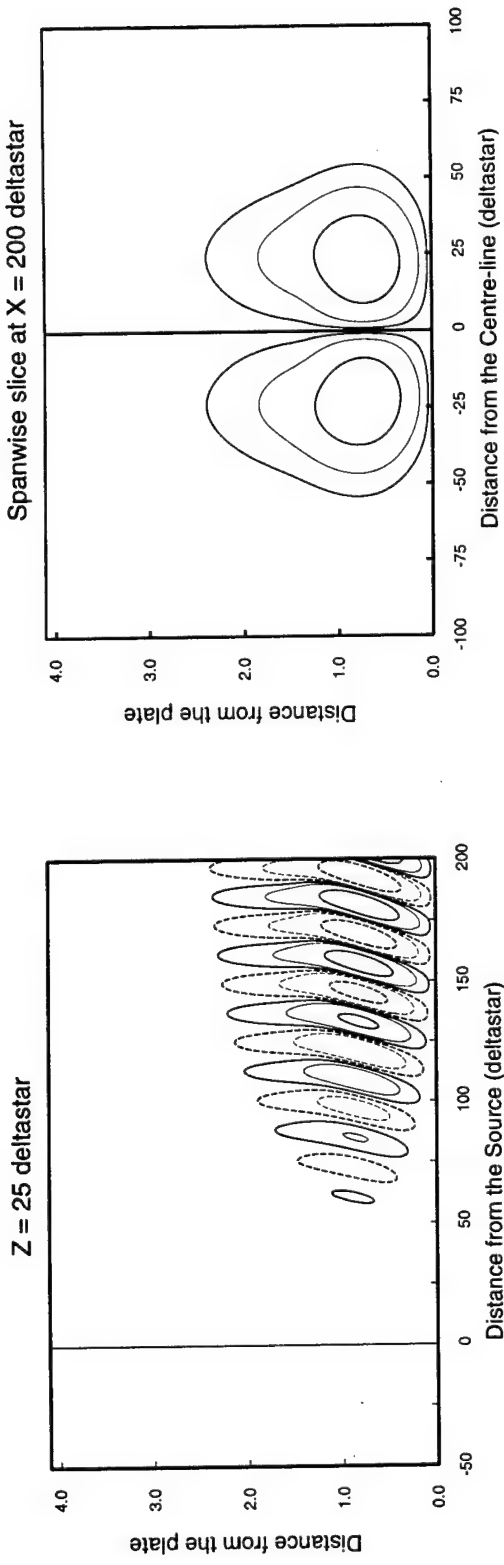
Lowest contour 0.001

Figure 3.1.1(v) Contours of the Normal Vorticity

Spanwise slice at X = 200 deltastar

Distance from the Centre-line (deltastar)

Distance from the plate

Center-Line Z = 0

Distance from the Source (deltastar)

Distance from the plate

Slice at Y = 0.5 deltastar

Distance from the source (deltastar)

Distance across the span

Excitation by a periodic u component

Reynolds number (deltastar) = 1000.0

Fnumber = 100E-6

Falkner-Skan parameter = 0.0

Lowest contour 0.001

Figure 3.1.1(vi) Contours of Spanwise Vorticity
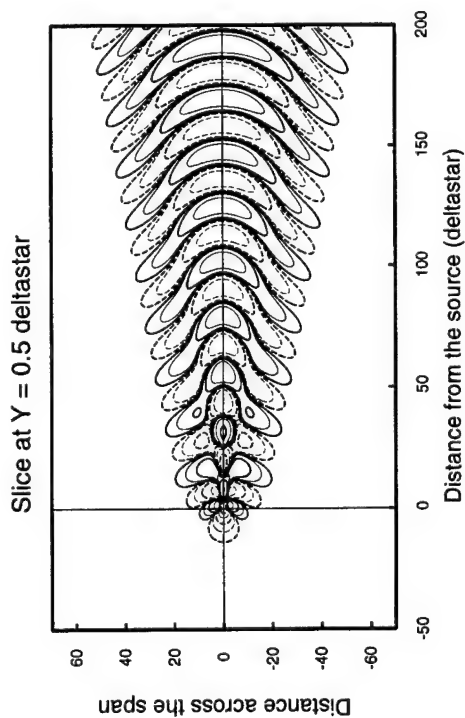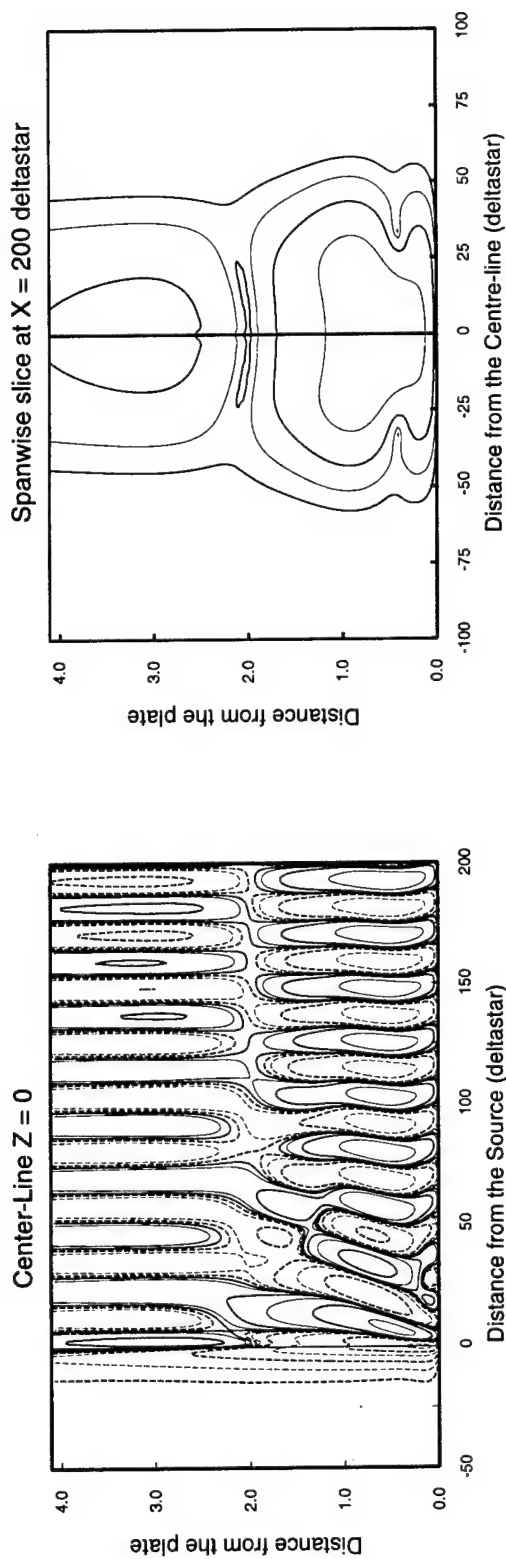
Spanwise slice at X = 200 deltastar

Center-Line Z = 0

Slice at Y = 0.5 deltastar
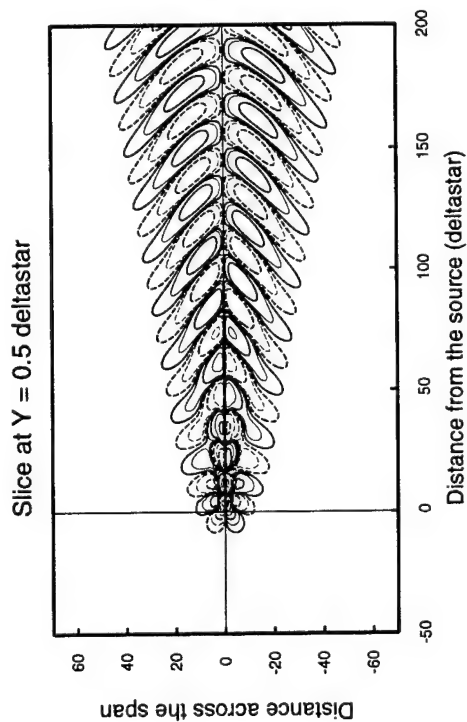
Excitation by a periodic v component

Reynolds number (deltastar) = 1000.0

Fnumber = 100E-6

Falkner-Skan parameter = 0.0

Lowest contour 0.001

Figure 3.1.2(i) Contours of the u perturbation

68

Spanwise slice at X = 200 deltastar
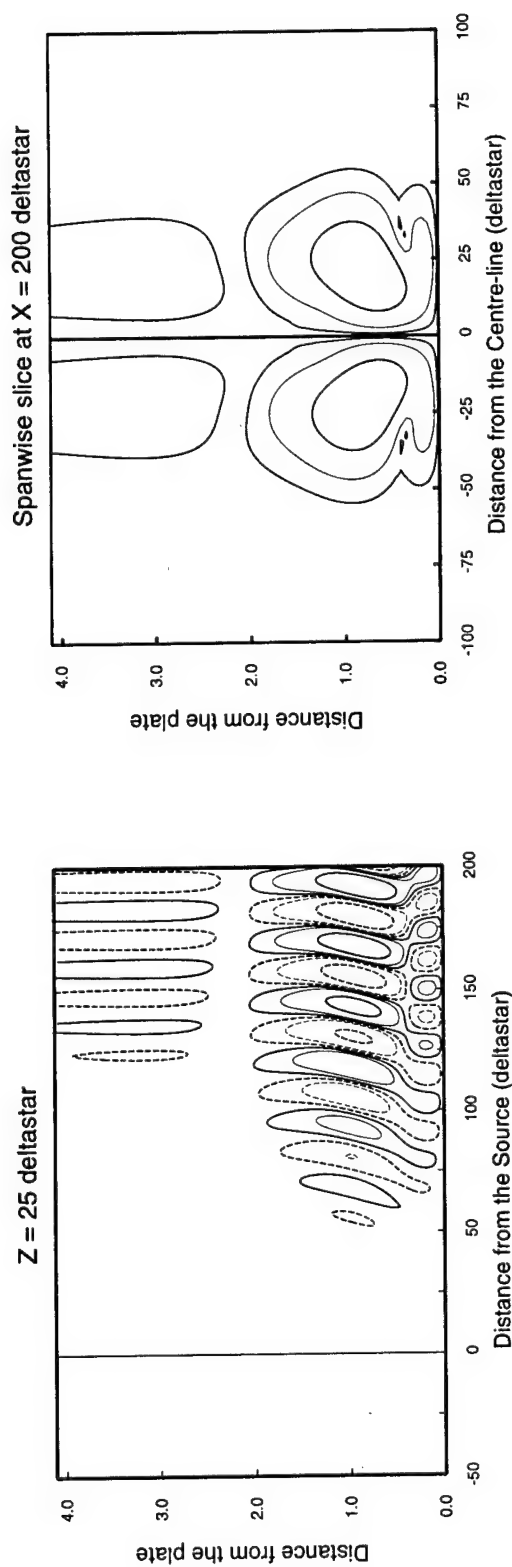
Center-Line Z = 0

Slice at Y = 2.0 deltastar

Excitation by a periodic v component

Reynolds number (deltastar) = 1000.0

Fnumber = 100E-6

Falkner-Skan parameter = 0.0

Lowest contour 0.001

Figure 3.1.2(ii) Contours of the v perturbation

Spanwise slice at X = 200 deltastar

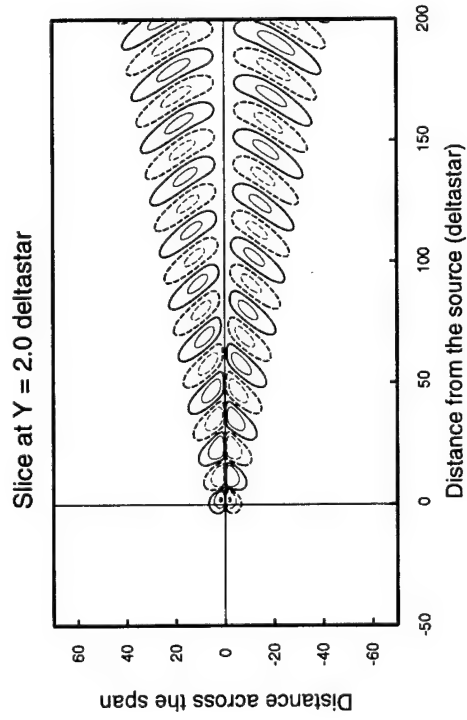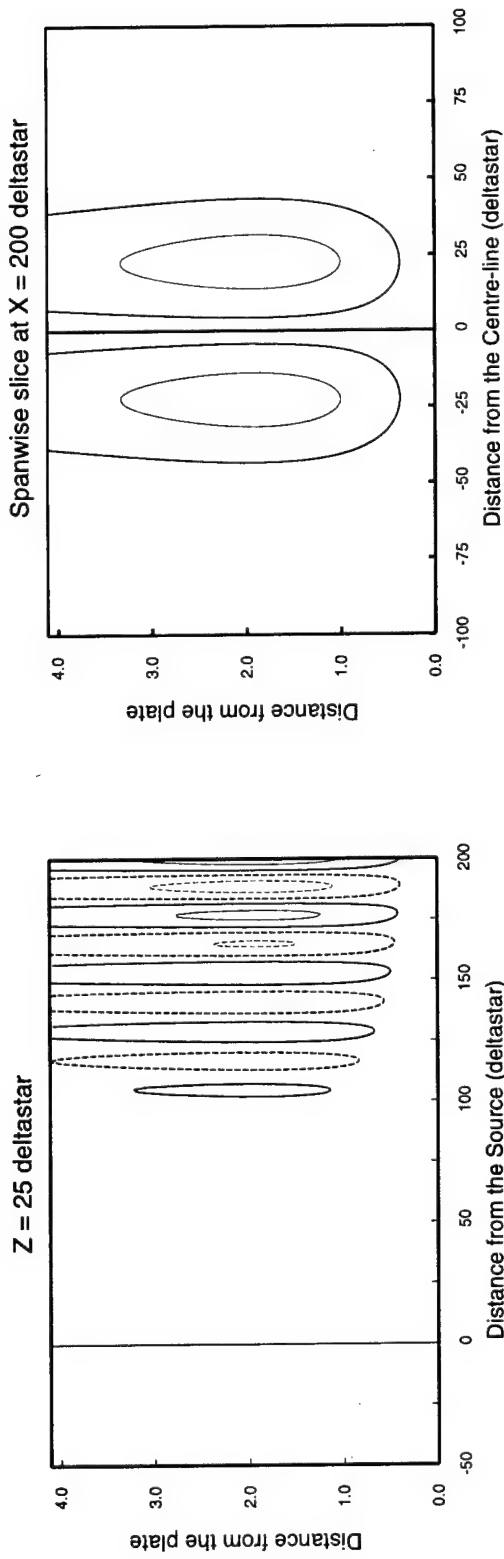Distance from the Centre-line (deltastar)

Distance from the plate

Excitation by a periodic v component

Reynolds number (deltastar) = 1000.0

Fnumber = 100E-6

Falkner-Skan parameter = 0.0

Lowest contour 0.001

Z = 25 deltastar

Distance from the Source (deltastar)

Distance from the plate

Slice at Y = 0.5 deltastar

Distance from the source (deltastar)

Distance across the span

Figure 3.1.2(iii) Contours of the w perturbation

Spanwise slice at X = 200 deltastar
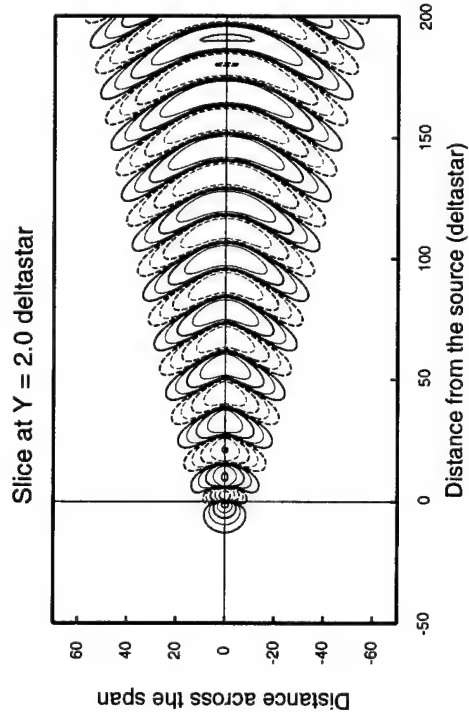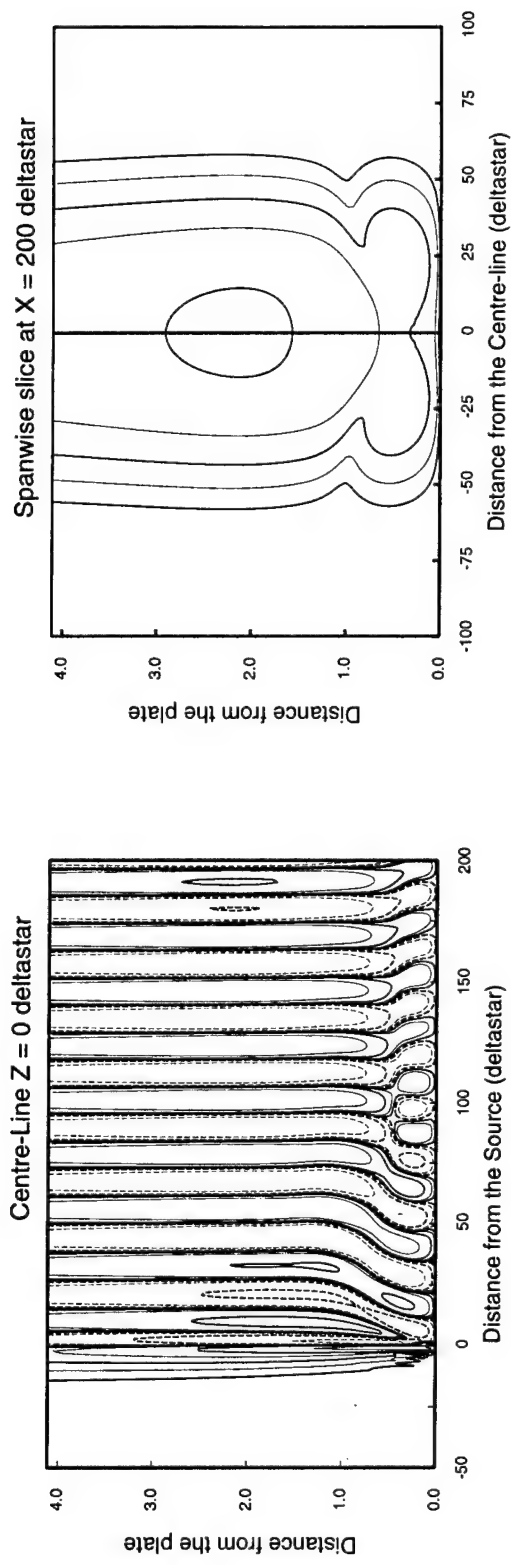
Z = 25 deltastar

Slice at Y = 0.5 deltastar

Excitation by a periodic v component
Reynolds number (deltastar) = 1000.0
Fnumber = 100E-6
Falkner-Skan parameter = 0.0
Lowest contour 0.001
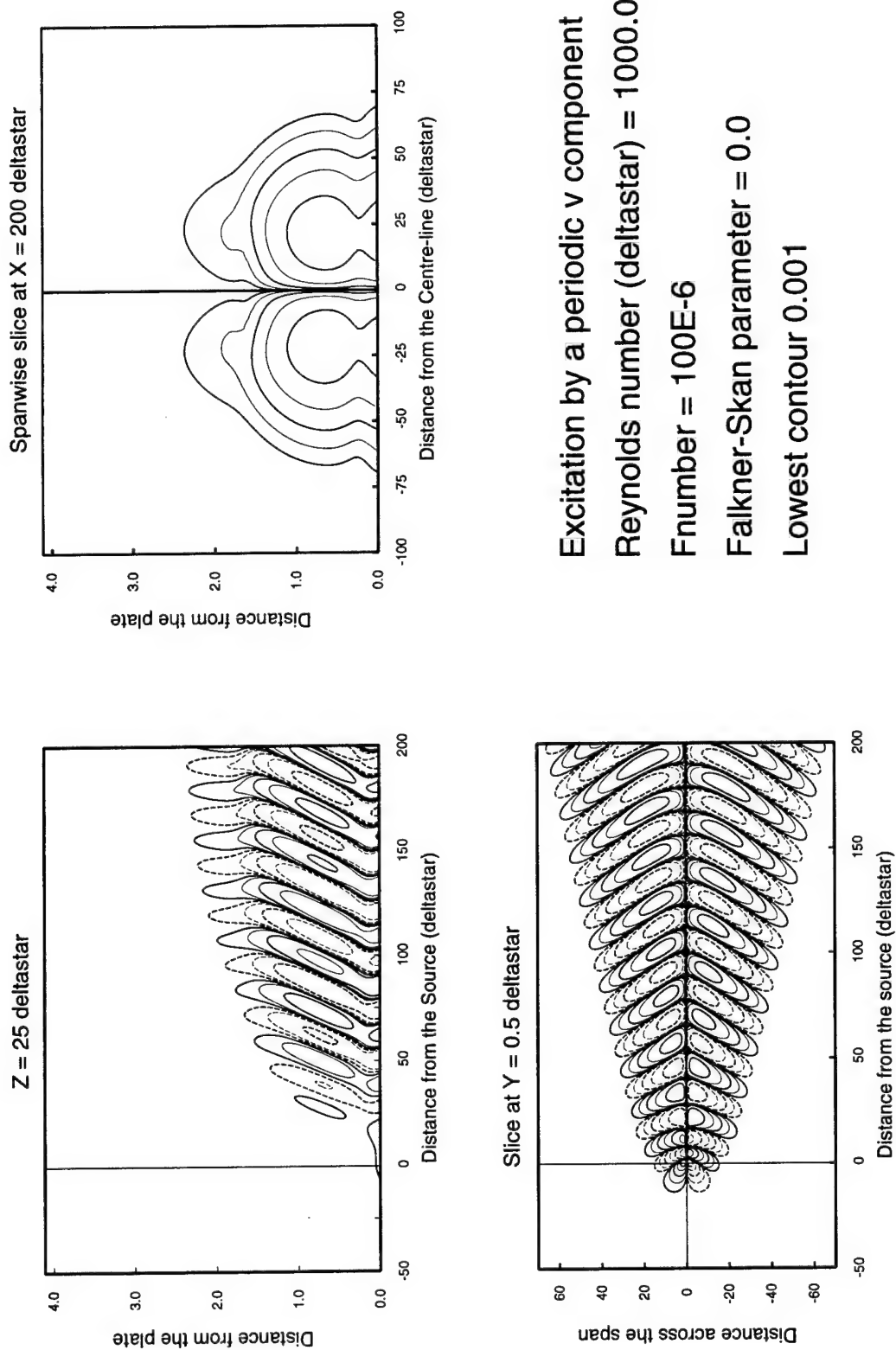
Figure 3.1.2(iv) Contours of Streamwise Vorticity

Spanwise slice at X = 200 deltastar

Z = 25 deltastar

Slice at Y = 0.5 deltastar

Excitation by a periodic v component

Reynolds number (deltastar) = 1000.0

Fnumber = 100E-6

Falkner-Skan parameter = 0.0

Lowest contour 0.001

Figure 3.1.2(v) Contours of Normal Vorticity
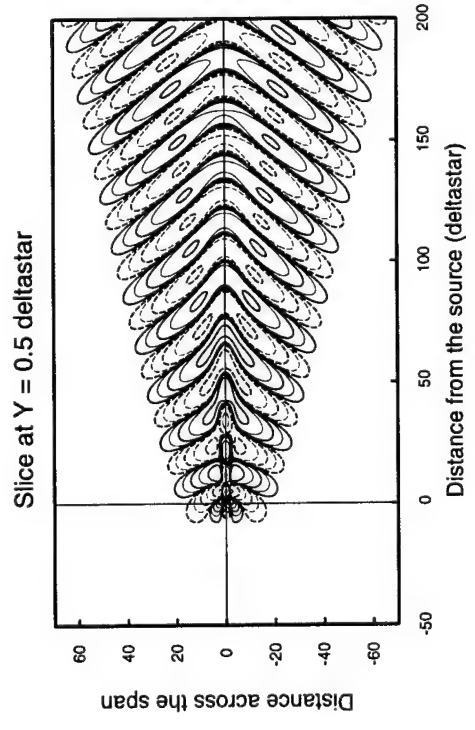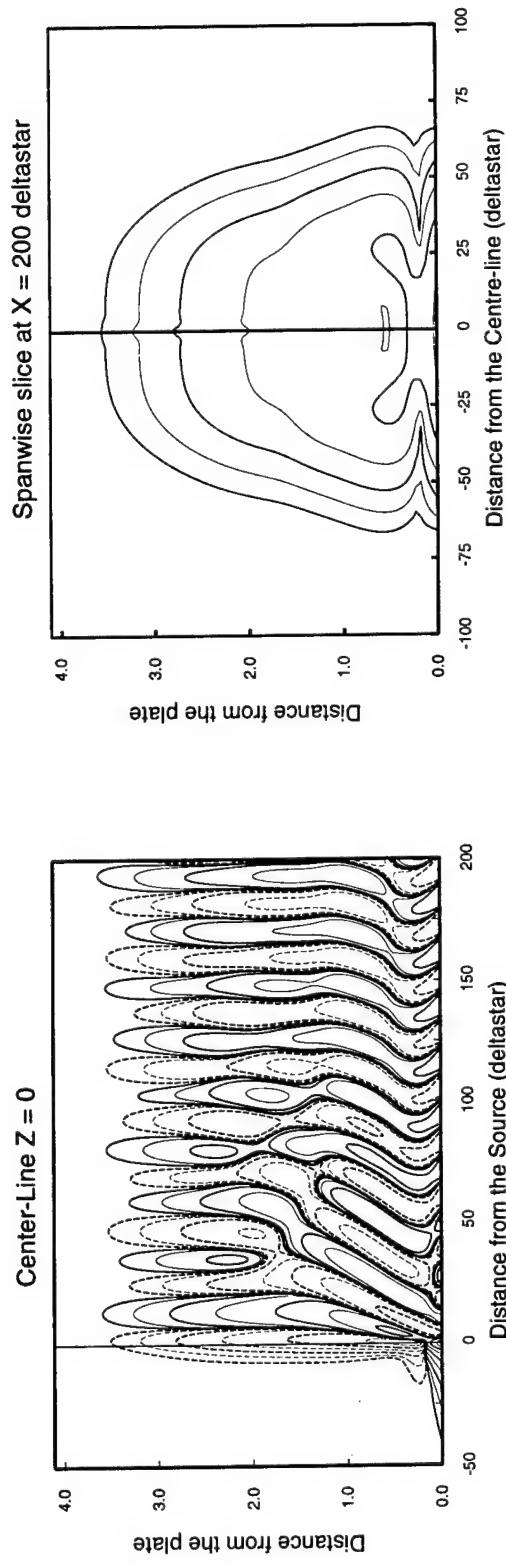
Spanwise slice at X = 200 deltastar

Center-Line Z = 0

Slice at Y = 0.5 deltastar

Excitation by a periodic v component

Reynolds number (deltastar) = 1000.0

Fnumber = 100E-6

Falkner-Skan parameter = 0.0
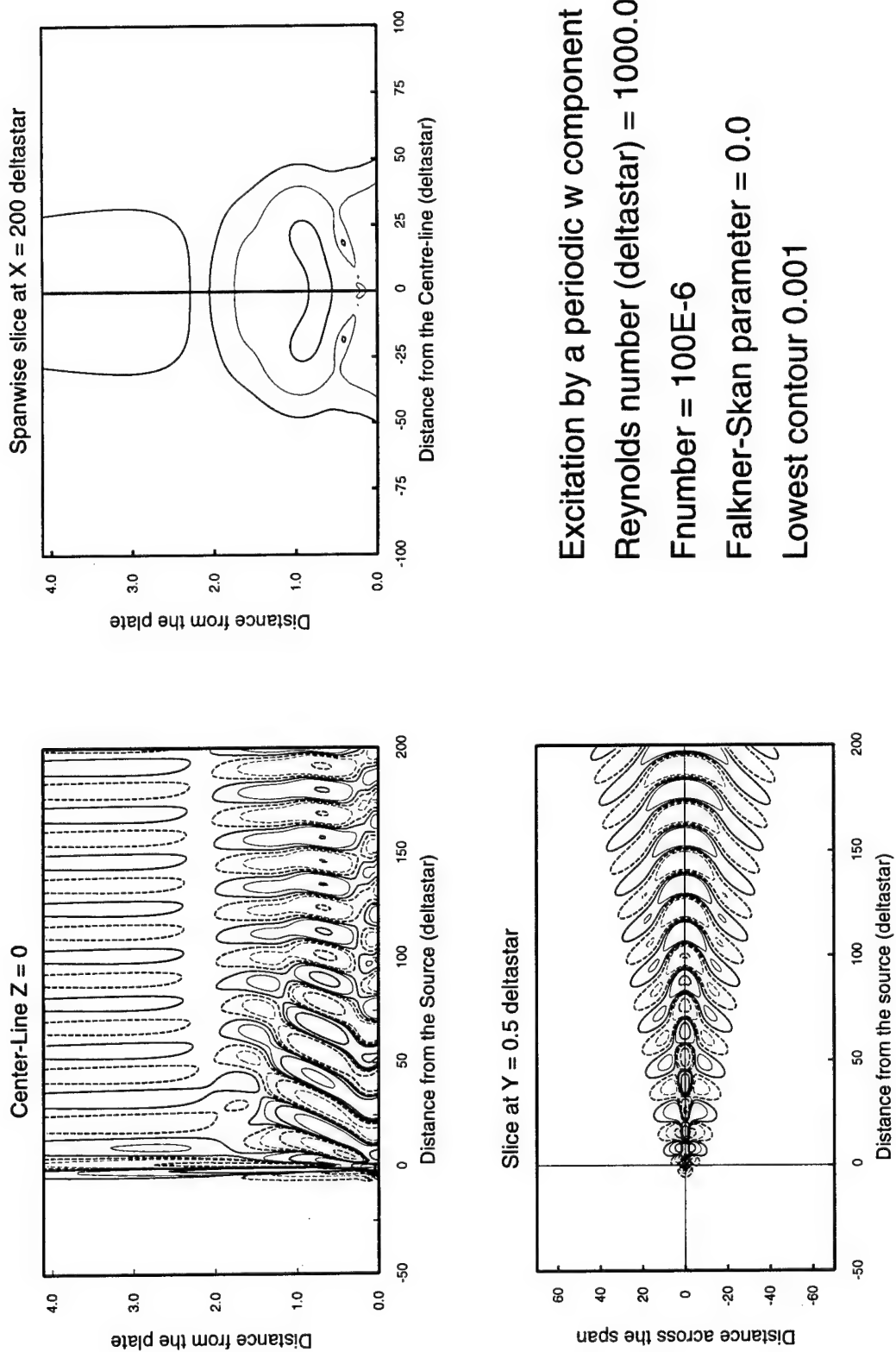
Lowest contour 0.001

Figure 3.1.2(vi) Contours of Spanwise Vorticity

Spanwise slice at X = 200 deltastar

Distance from the plate

Distance from the Centre-line (deltastar)

Z = 25 deltastar

Distance from the plate

Distance from the Source (deltastar)

Slice at Y = 0.5 deltastar

Distance across the span

Distance from the source (deltastar)

Excitation by a periodic w component

Reynolds number (deltastar) = 1000.0

Fnumber = 100E-6

Falkner-Skan parameter = 0.0

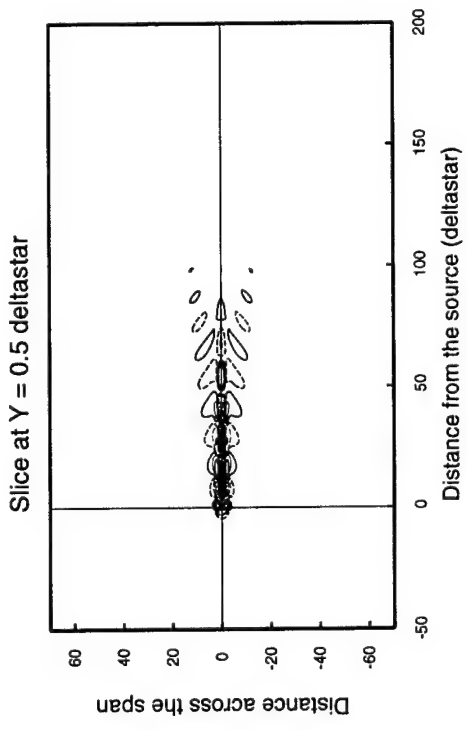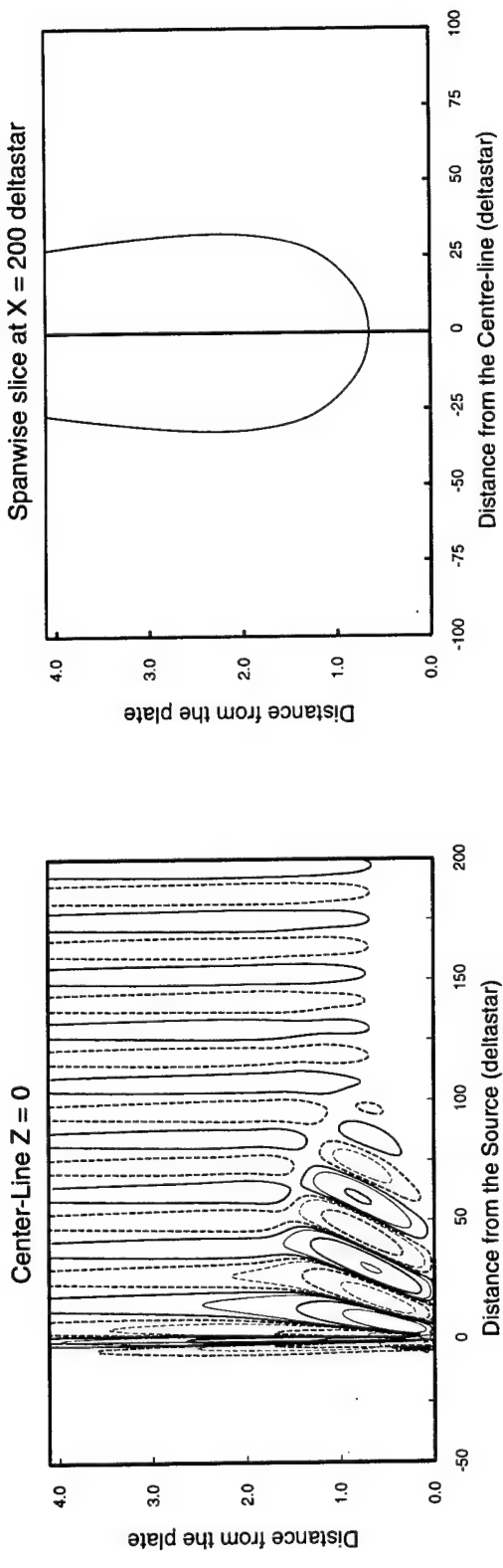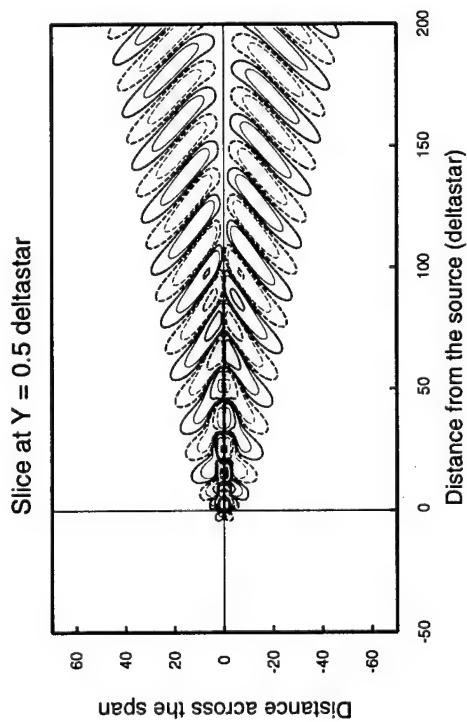Lowest contour 0.0001

Figure 3.1.3(i) Contours of the u perturbation

Spanwise slice at X = 200 deltastar

Distance from the plate

Distance from the Centre-line (deltastar)

Z = 25 deltastar

Distance from the plate

Distance from the Source (deltastar)

Slice at Y = 2.0 deltastar

Distance across the span

Distance from the source (deltastar)

Excitation by a periodic w component

Reynolds number (deltastar) = 1000.0

Fnumber = 100E-6

Falkner-Skan parameter = 0.0

Lowest contour 0.0001

Figure 3.1.3(ii) Contours of the v perturbation

75

Spanwise slice at X = 200 deltastar

Centre-Line Z = 0 deltastar

Slice at Y = 2.0 deltastar

Excitation by a periodic w component

Reynolds number (deltastar) = 1000.0

Fnumber = 100E-6

Falkner-Skan parameter = 0.0

Lowest contour 0.0001

Figure 3.1.3(iii) Contours of the w perturbation

Spanwise slice at X = 200 deltastar

Center-Line Z = 0

Slice at Y = 0.5 deltastar

Excitation by a periodic w component
Reynolds number (deltastar) = 1000.0
Fnumber = 100E-6
Falkner-Skan parameter = 0.0
Lowest contour 0.001

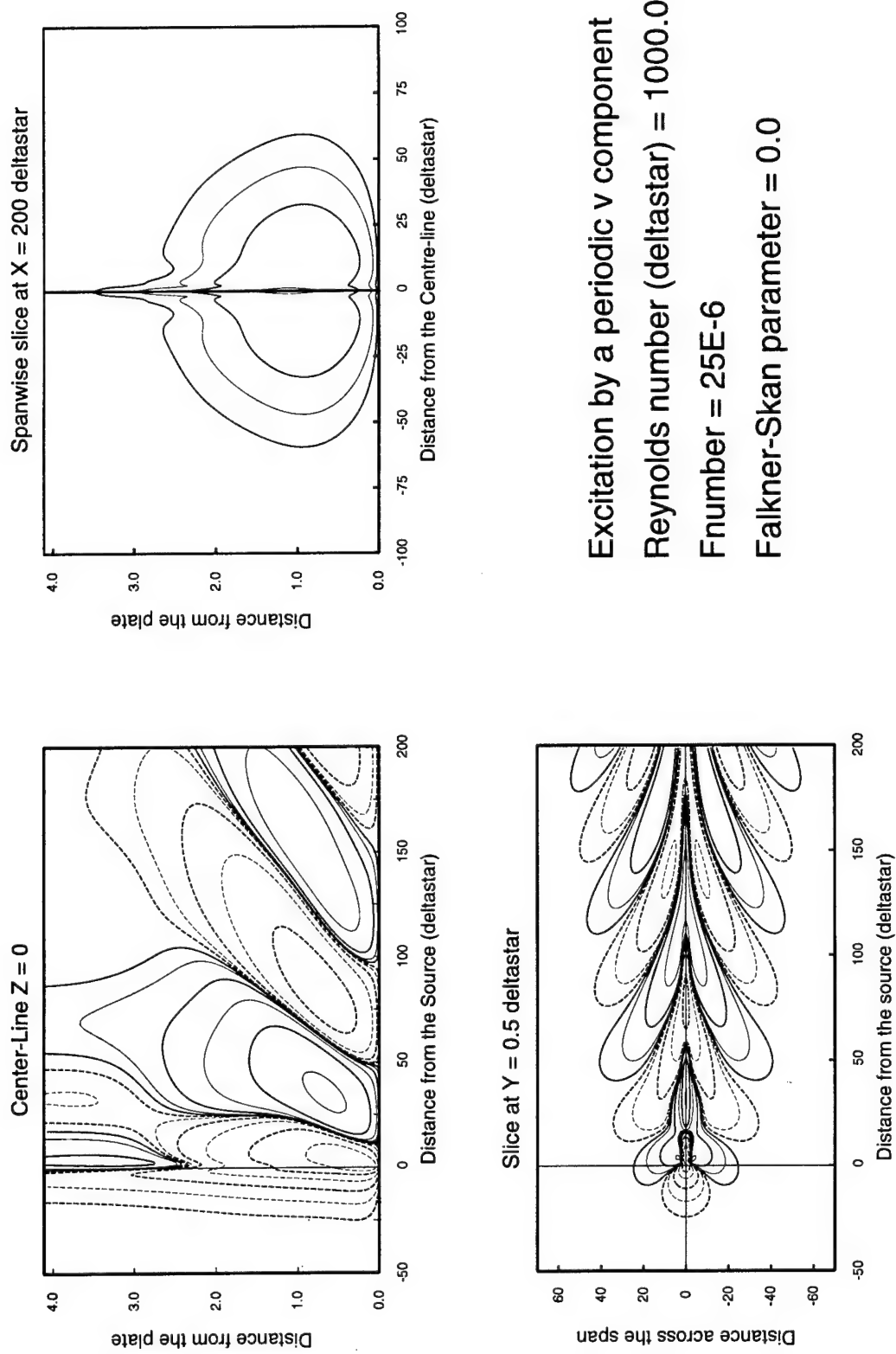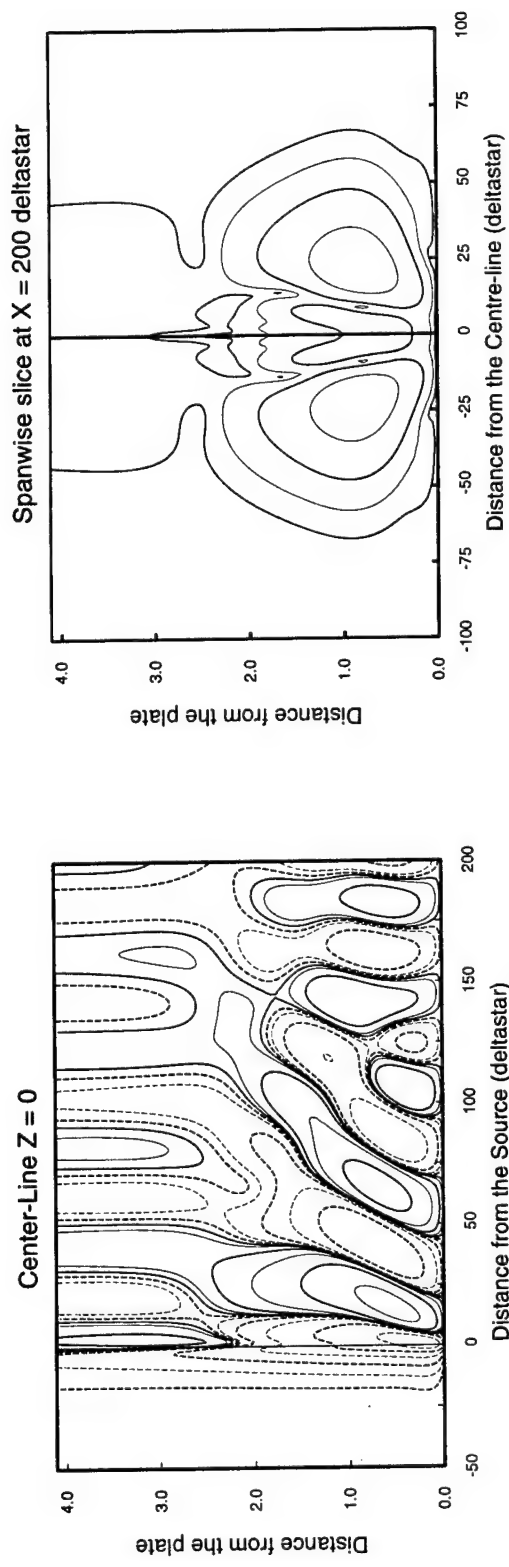Figure 3.1.3(iv) Contours of Streamwise Vorticity

Spanwise slice at X = 200 deltastar

Distance from the plate

Distance from the Centre-line (deltastar)

Center-Line Z = 0

Distance from the plate

Distance from the Source (deltastar)

Slice at Y = 0.5 deltastar

Distance across the span

Distance from the source (deltastar)

Excitation by a periodic w component

Reynolds number (deltastar) = 1000.0

Fnumber = 100E-6

Falkner-Skan parameter = 0.0

Lowest contour 0.001

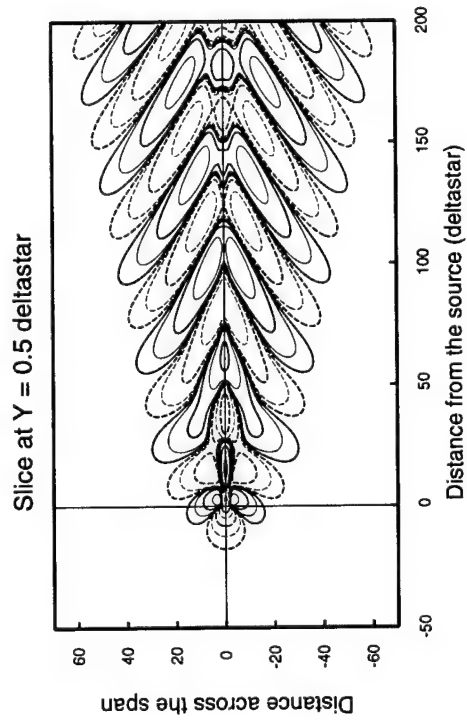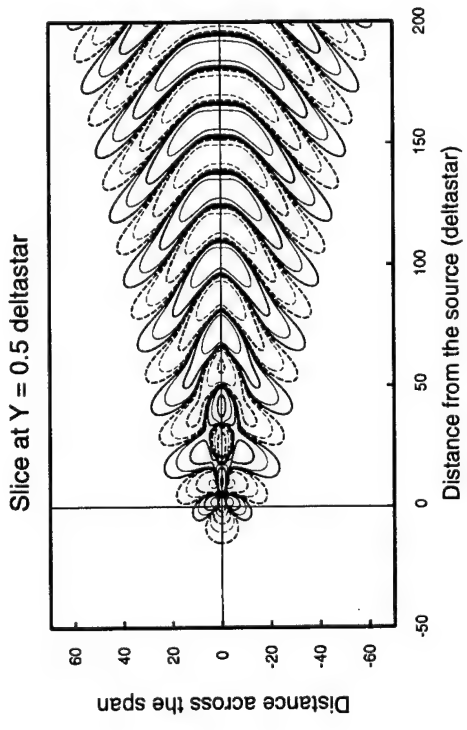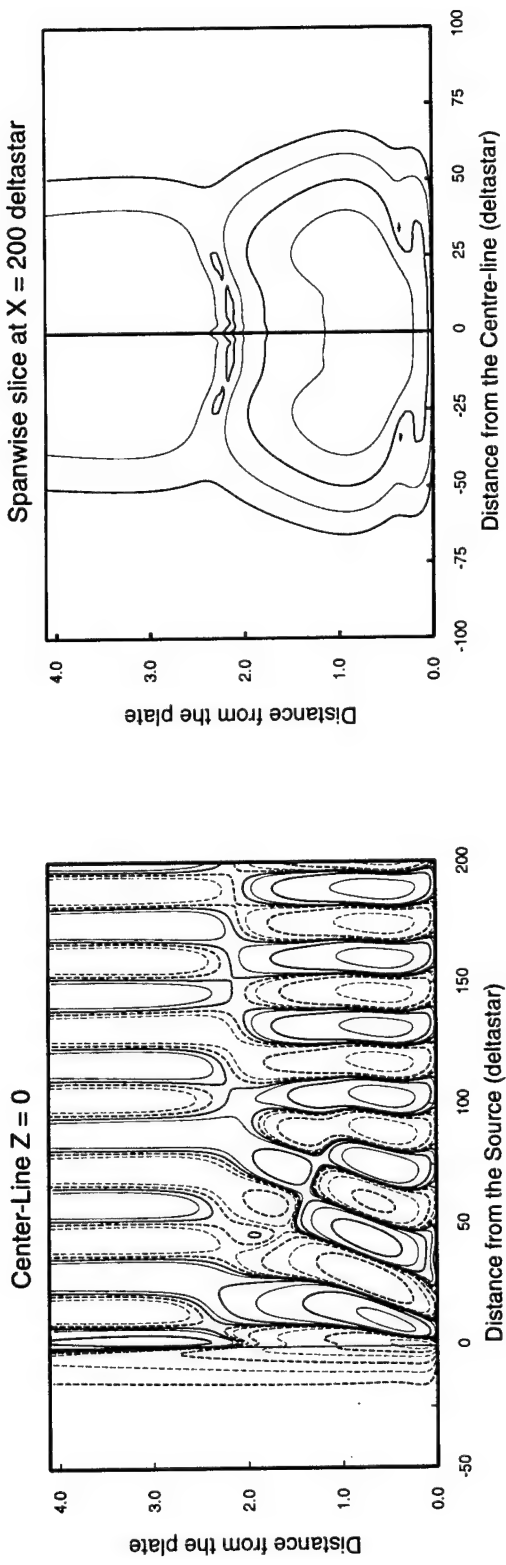Figure 3.1.3(v) Contours of Normal Vorticity
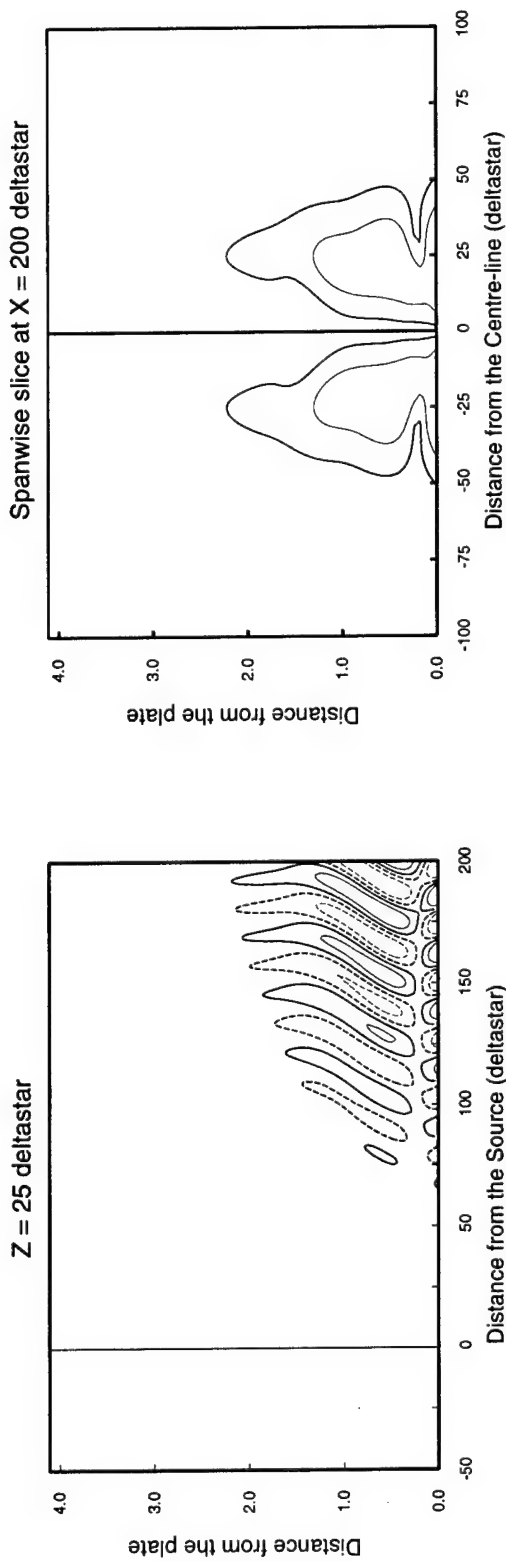
Spanwise slice at X = 200 deltastar

Distance from the Centre-line (deltastar)

Distance from the plate

Excitation by a periodic w component

Reynolds number (deltastar) = 1000.0

Fnumber = 100E-6

Falkner-Skan parameter = 0.0

Lowest contour 0.001

Z = 25 deltastar

Distance from the Source (deltastar)

Distance from the plate

Slice at Y = 0.5 deltastar

Distance from the source (deltastar)

Distance across the span

Figure 3.1.3(vi) Contours of Spnawise Vorticity

Spanwise slice at X = 200 deltastar

Center-Line Z = 0

Slice at Y = 0.5 deltastar

Excitation by a periodic v component

Reynolds number (deltastar) = 1000.0

Fnumber = 25E-6

Falkner-Skan parameter = 0.0

Figure 3.2(i) Influence of Fnumber on Response

80

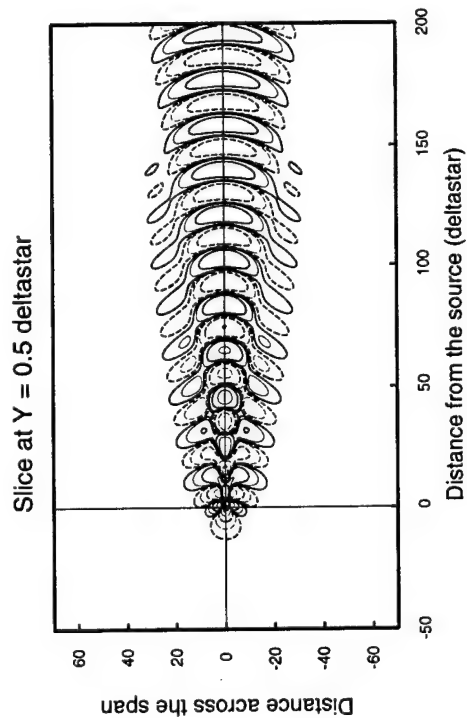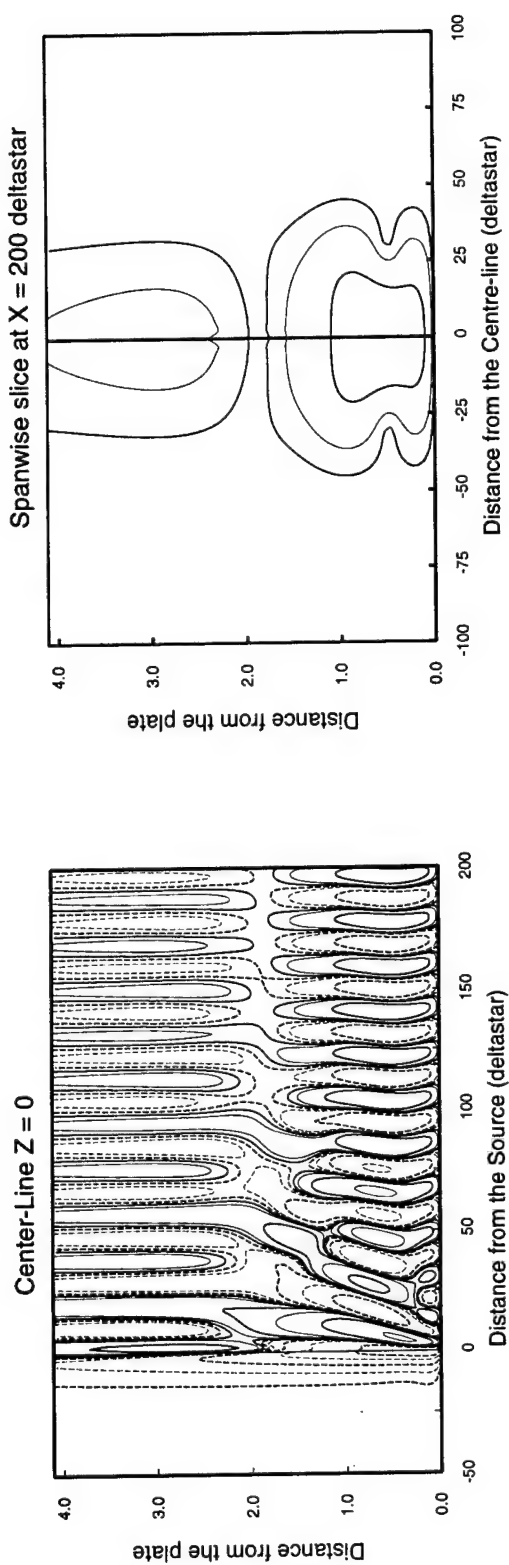Spanwise slice at X = 200 deltastar

Distance from the plate

Distance from the Centre-line (deltastar)

Excitation by a periodic v component

Reynolds number (deltastar) = 1000.0

Fnumber = 50E-6

Falkner-Skan parameter = 0.0

Center-Line Z = 0

Distance from the plate

Distance from the Source (deltastar)

Slice at Y = 0.5 deltastar

Distance across the span

Distance from the source (deltastar)

Figure 3.2(ii) Influence of Fnumber on Response

Spanwise slice at X = 200 deltastar

Center-Line Z = 0
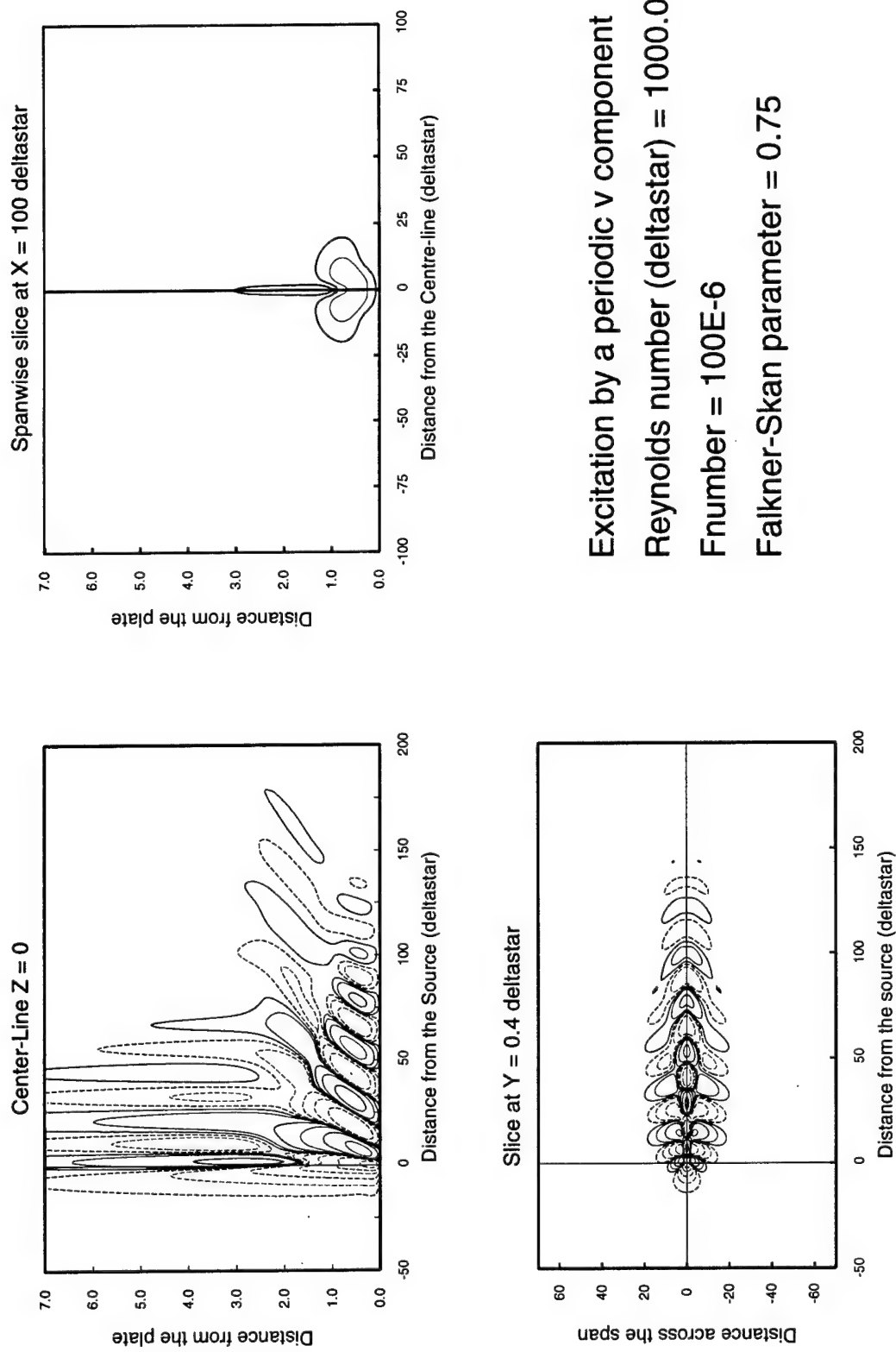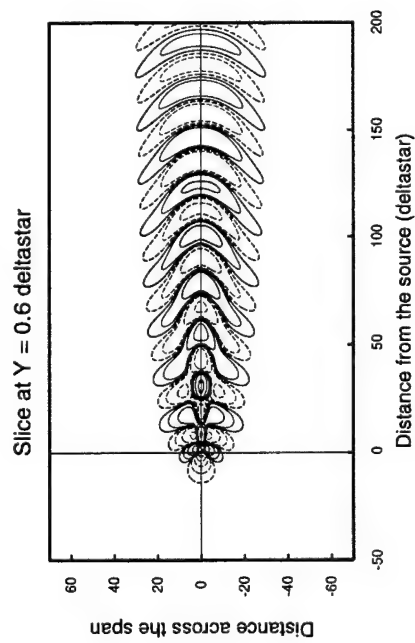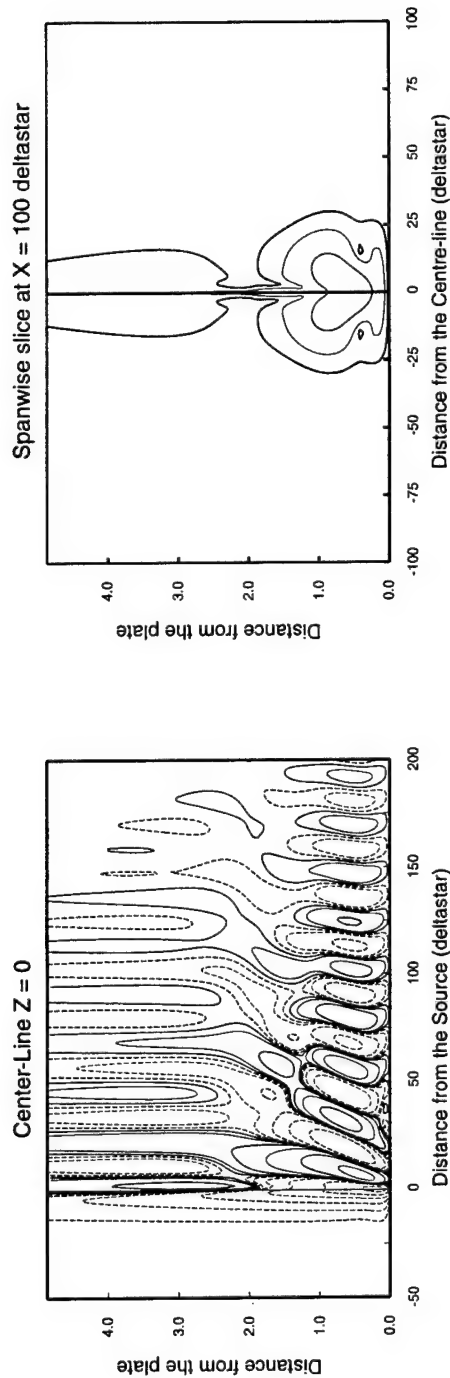
Slice at Y = 0.5 deltastar

Excitation by a periodic v component

Reynolds number (deltastar) = 1000.0

Fnumber = 75E-6

Falkner-Skan parameter = 0.0

Figure 3.2(iii) Influence of Fnumber on Response

82

Spanwise slice at X = 200 deltastar

Excitation by a periodic v component
Reynolds number (deltastar) = 1000.0
Fnumber = 100E-6
Falkner-Skan parameter = 0.0

Center-Line Z = 0

Slice at Y = 0.5 deltastar
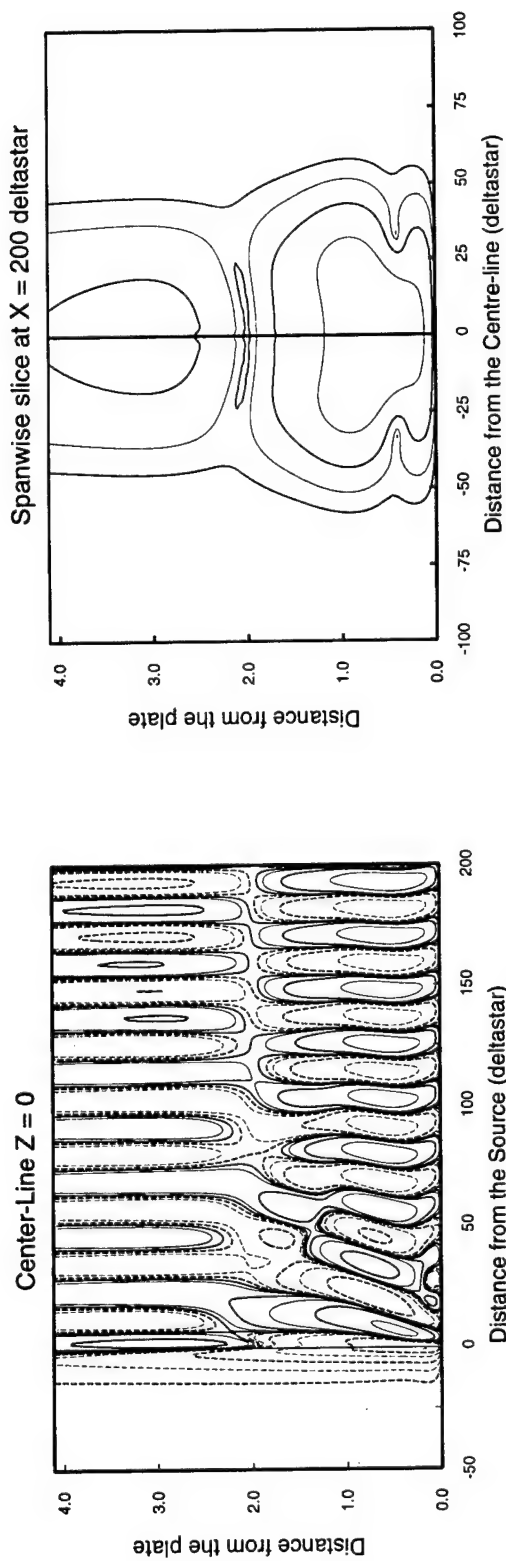
Figure 3.2(iv) Influence of Fnumber on Response

Spanwise slice at X = 200 deltastar

Center-Line Z = 0

Slice at Y = 0.5 deltastar

Excitation by a periodic v component

Reynolds number (deltastar) = 1000.0

Fnumber = 125E-6

Falkner-Skan parameter = 0.0
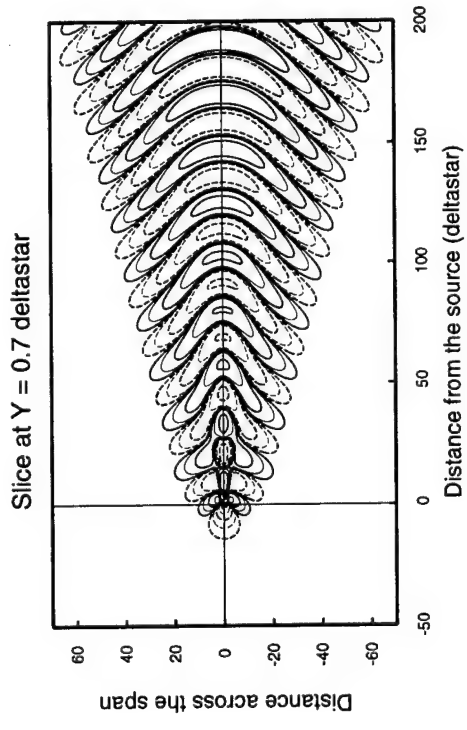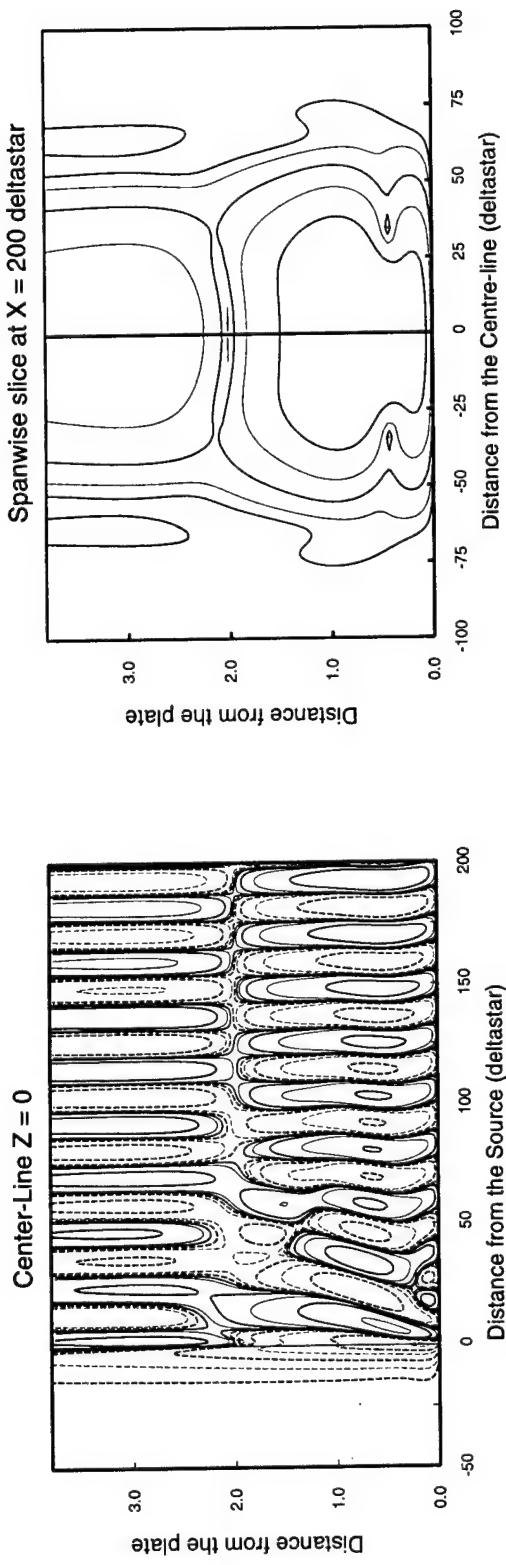
Figure 3.2(v) Influence of Fnumber on Response

Spanwise slice at X = 100 deltastar

Center-Line Z = 0

Slice at Y = 0.5 deltastar
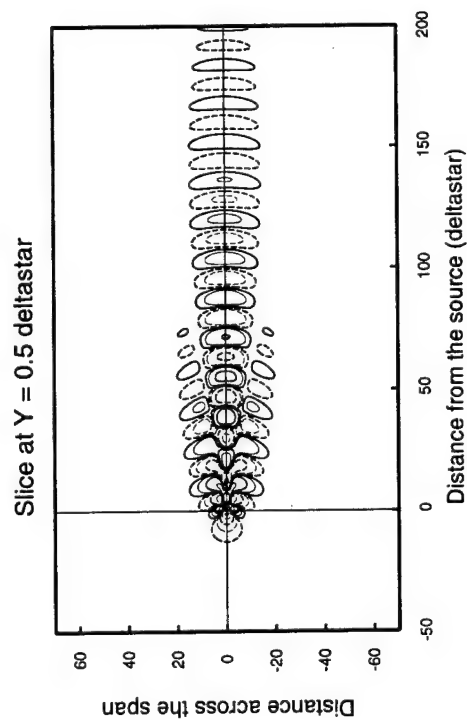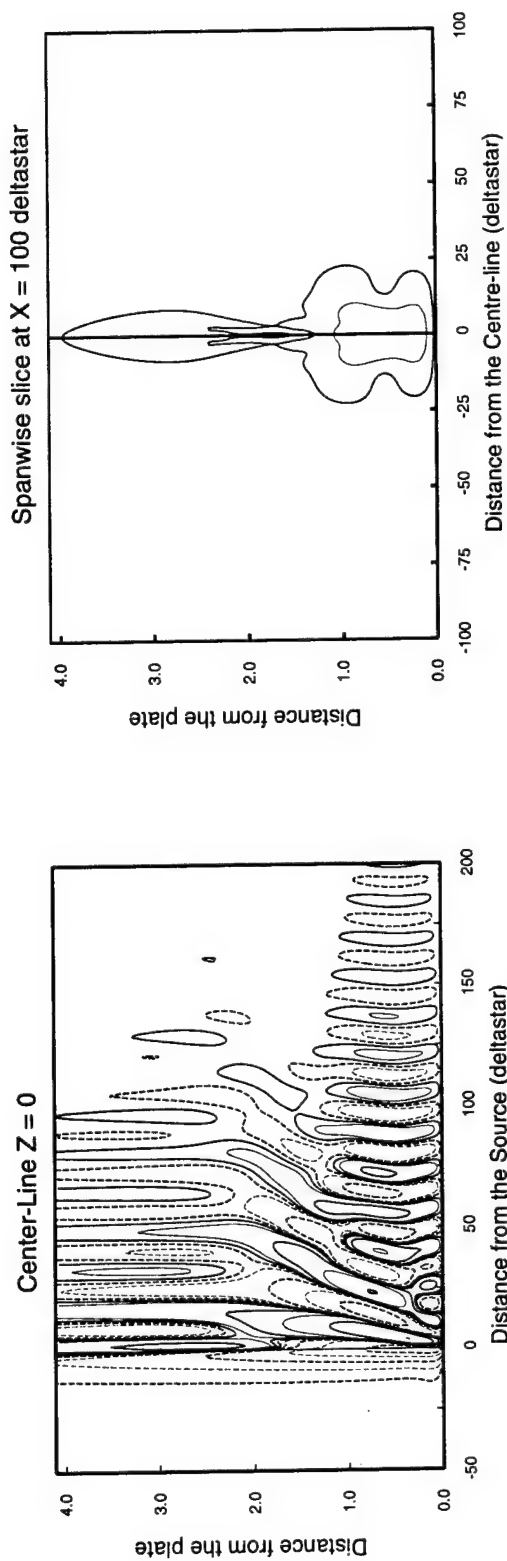
Excitation by a periodic v component

Reynolds number (deltastar) = 1000.0

Fnumber = 150E-6

Falkner-Skan parameter = 0.0

Figure 3.2(vi)Influence of Fnumber on Response

85

Spanwise slice at X = 100 deltastar

Distance from the plate

Distance from the Centre-line (deltastar)

Center-Line Z = 0

Distance from the plate

Distance from the Source (deltastar)

Slice at Y = 0.4 deltastar

Distance across the span

Distance from the source (deltastar)

Excitation by a periodic v component

Reynolds number (deltastar) = 1000.0

Fnumber = 100E-6

Falkner-Skan parameter = 0.75
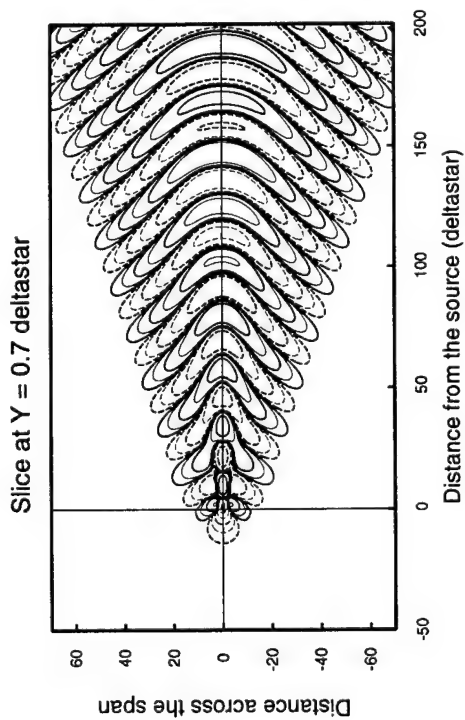
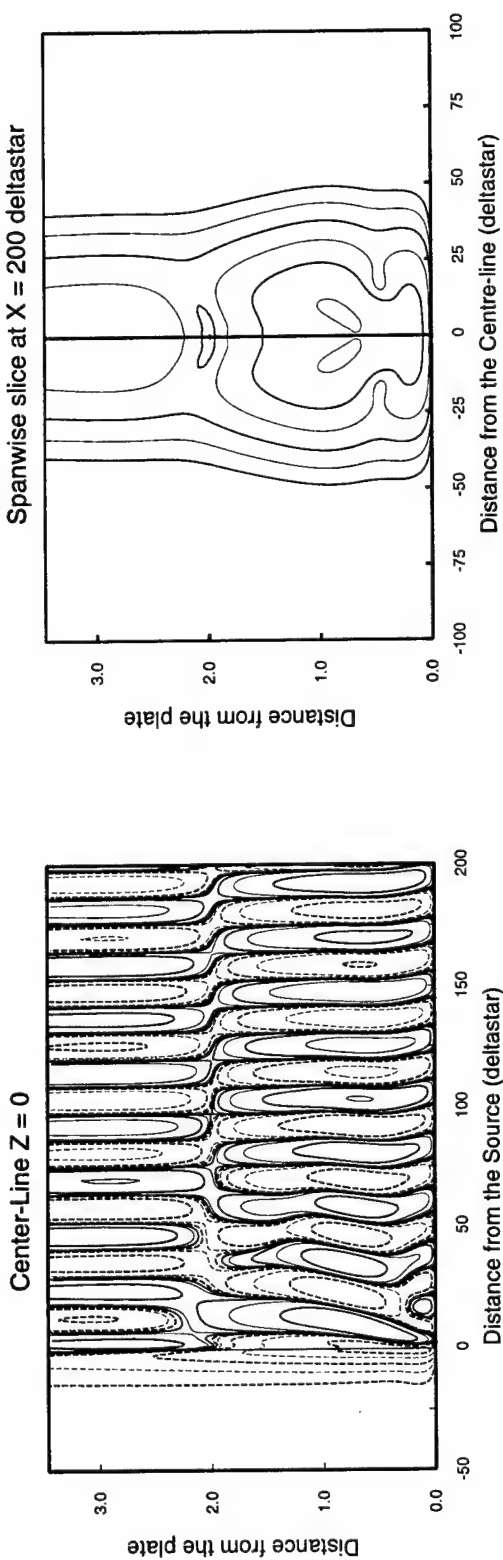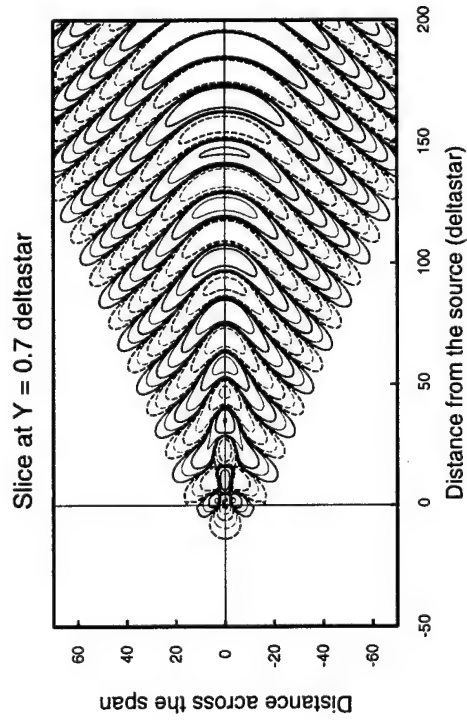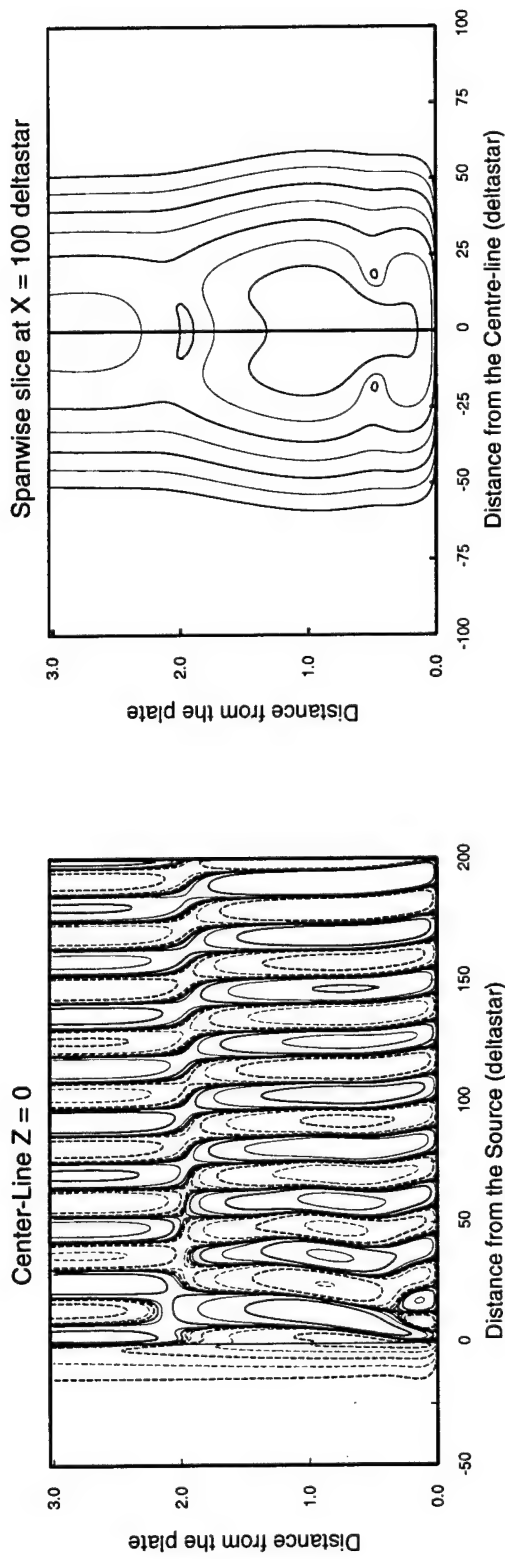Figure 3.3(i) Influence of Pressure Gradient

Figure 3.3(ii)

Spanwise slice at X = 100 deltastar

Distance from the Centre-line (deltastar)

Distance from the plate

Excitation by a periodic v component

Reynolds number (deltastar) = 1000.0

Fnumber = 100E-6

Falkner-Skan parameter = 0.15

Center-Line Z = 0

Distance from the Source (deltastar)

Distance from the plate

Slice at Y = 0.6 deltastar

Distance from the source (deltastar)

Distance across the span

Spanwise slice at X = 200 deltastar

Distance from the Centre-line (deltastar)

Distance from the plate

Excitation by a periodic v component
Reynolds number (deltastar) = 1000.0
Fnumber = 100E-6
Falkner-Skan parameter = -0.05

Center-Line Z = 0

Distance from the Source (deltastar)

Distance from the plate

Slice at Y = 0.7 deltastar

Distance from the source (deltastar)

Distance across the span

Figure 3.3(iii) Influence of Pressure Gradient

88

Spanwise slice at X = 200 deltastar

Center-Line Z = 0

Slice at Y = 0.7 deltastar

Excitation by a periodic v component
Reynolds number (deltastar) = 1000.0
Fnumber = 100E-6
Falkner-Skan parameter = -0.1

Figure 3.3(iv) Influence of Pressure Gradient
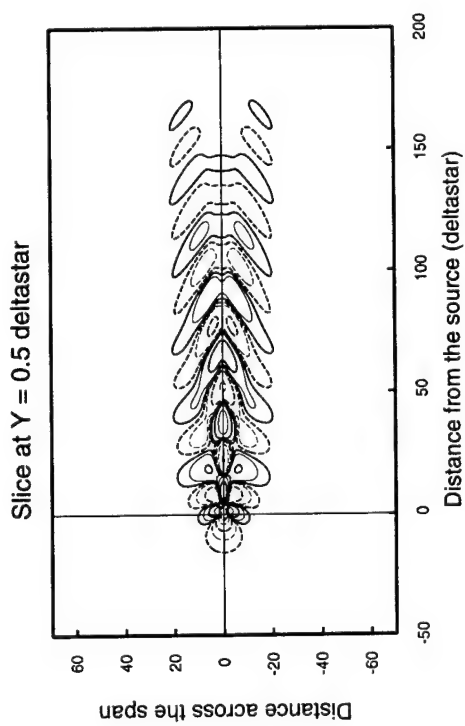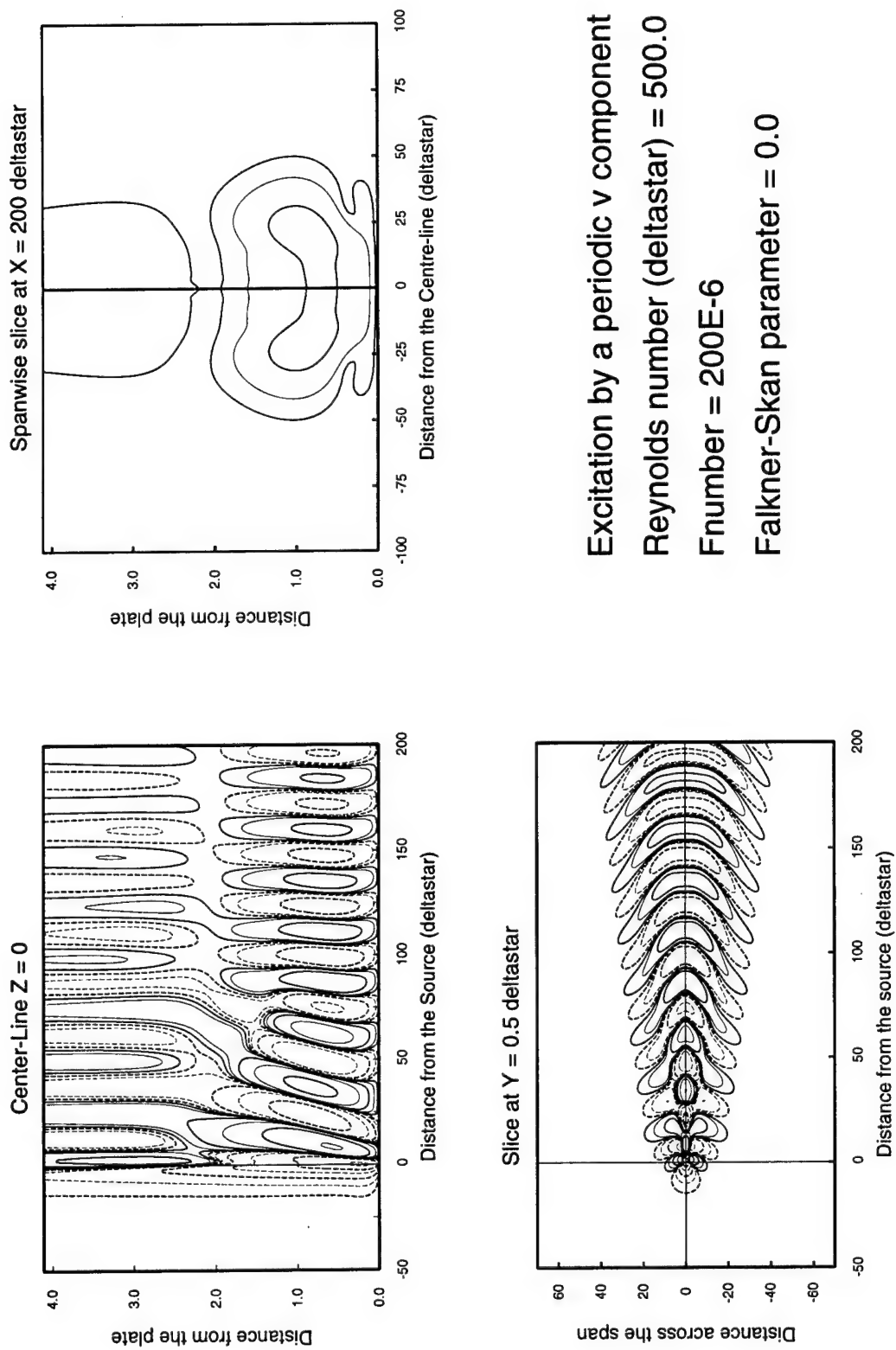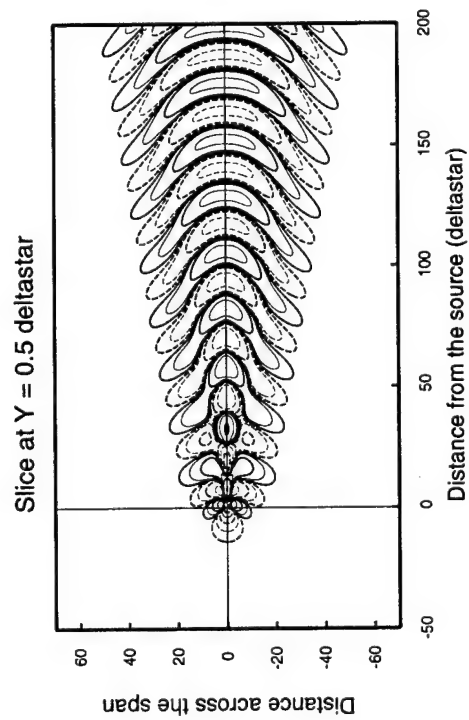
Spanwise slice at X = 100 deltastar

Excitation by a periodic v component

Reynolds number (deltastar) = 1000.0

Fnumber = 100E-6

Falkner-Skan parameter = -0.15

Center-Line Z = 0

Slice at Y = 0.7 deltastar

Figure 3.3(v) Influence of Pressure Gradient

Spanwise slice at X = 100 deltastar
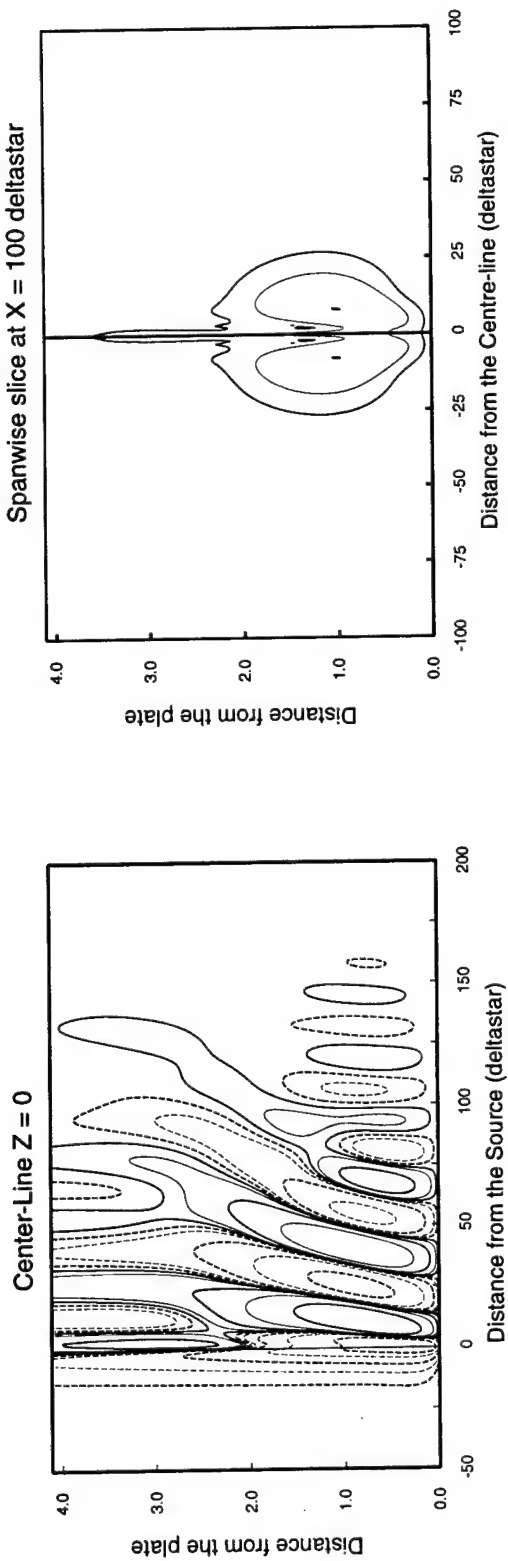
Excitation by a periodic v component
Reynolds number (deltastar) = 250.0
Fnumber = 400E-6
Falkner-Skan parameter = 0.0

Center-Line Z = 0

Slice at Y = 0.5 deltastar

Figure 3.4(i) Influence of Reynolds number

91

Spanwise slice at X = 200 deltastar

Center-Line Z = 0

Slice at Y = 0.5 deltastar

Excitation by a periodic v component
Reynolds number (deltastar) = 500.0
Fnumber = 200E-6
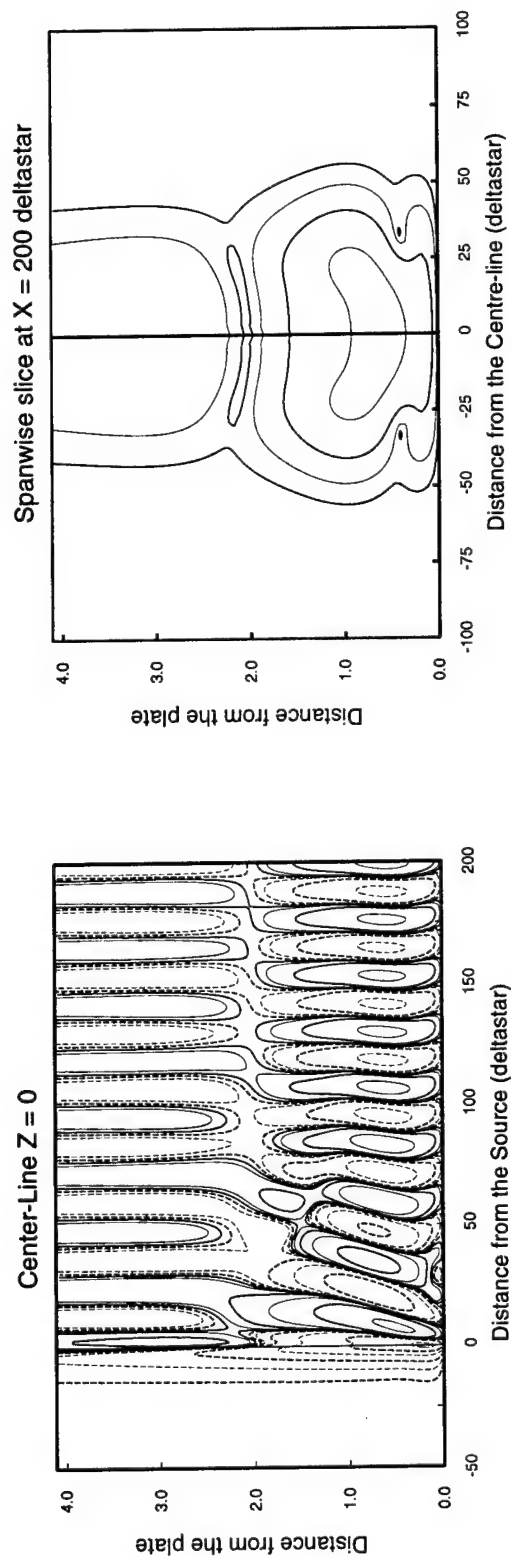Falkner-Skan parameter = 0.0

Figure 3.4(ii) Influence of Reynolds number

Spanwise slice at X = 200 deltastar

Center-Line Z = 0

Slice at Y = 0.5 deltastar

Excitation by a periodic v component
Reynolds number (deltastar) = 750.0
Fnumber = 133.3E-6
Falkner-Skan parameter = 0.0

Figure 3.4(iii) Influence of Reynolds number

93

Spanwise slice at X = 200 deltastar

Center-Line Z = 0

Slice at Y = 0.5 deltastar
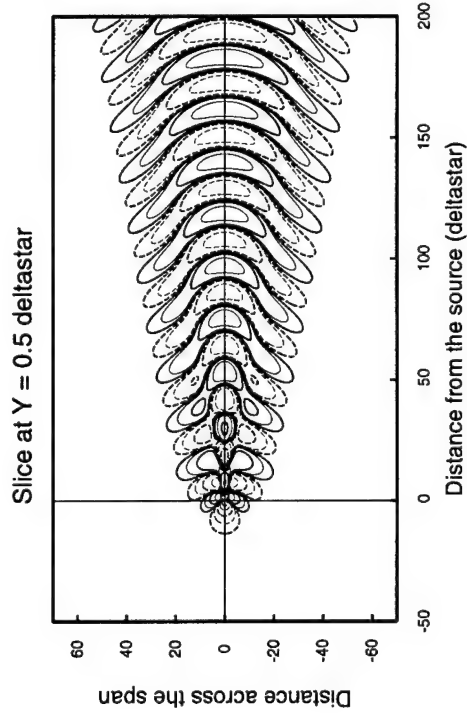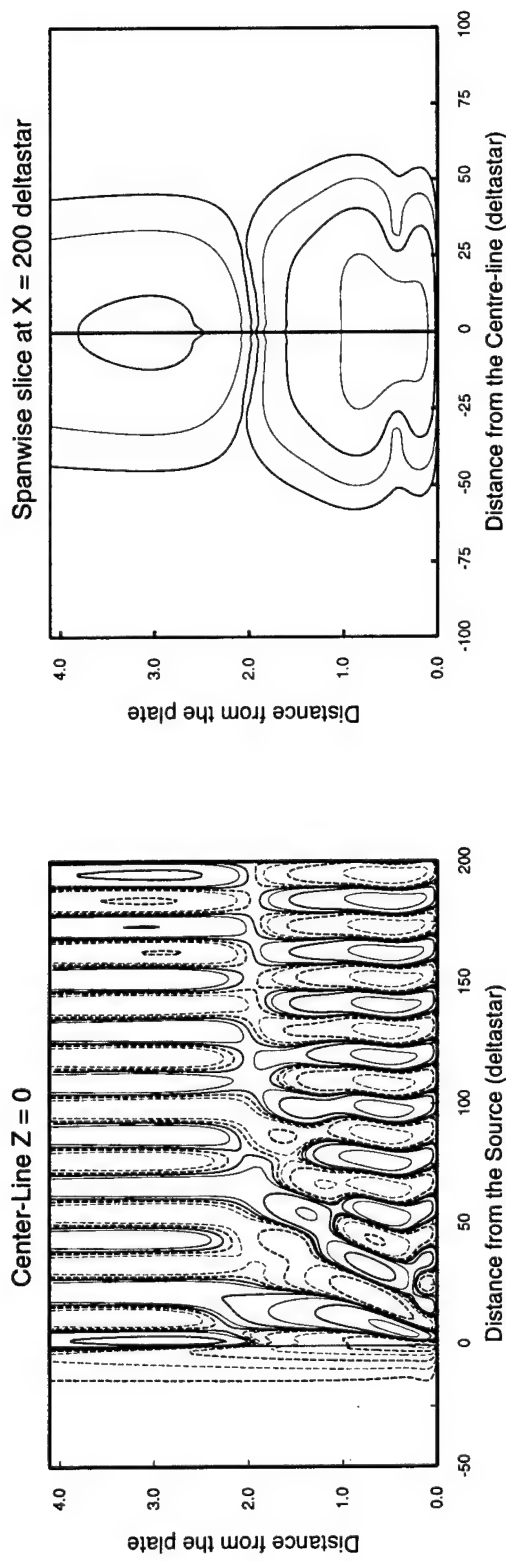
Excitation by a periodic v component
Reynolds number (deltastar) = 1500.0
Fnumber = 66.7E-6
Falkner-Skan parameter = 0.0

Figure 3.4(iv) Influence of Reynolds number

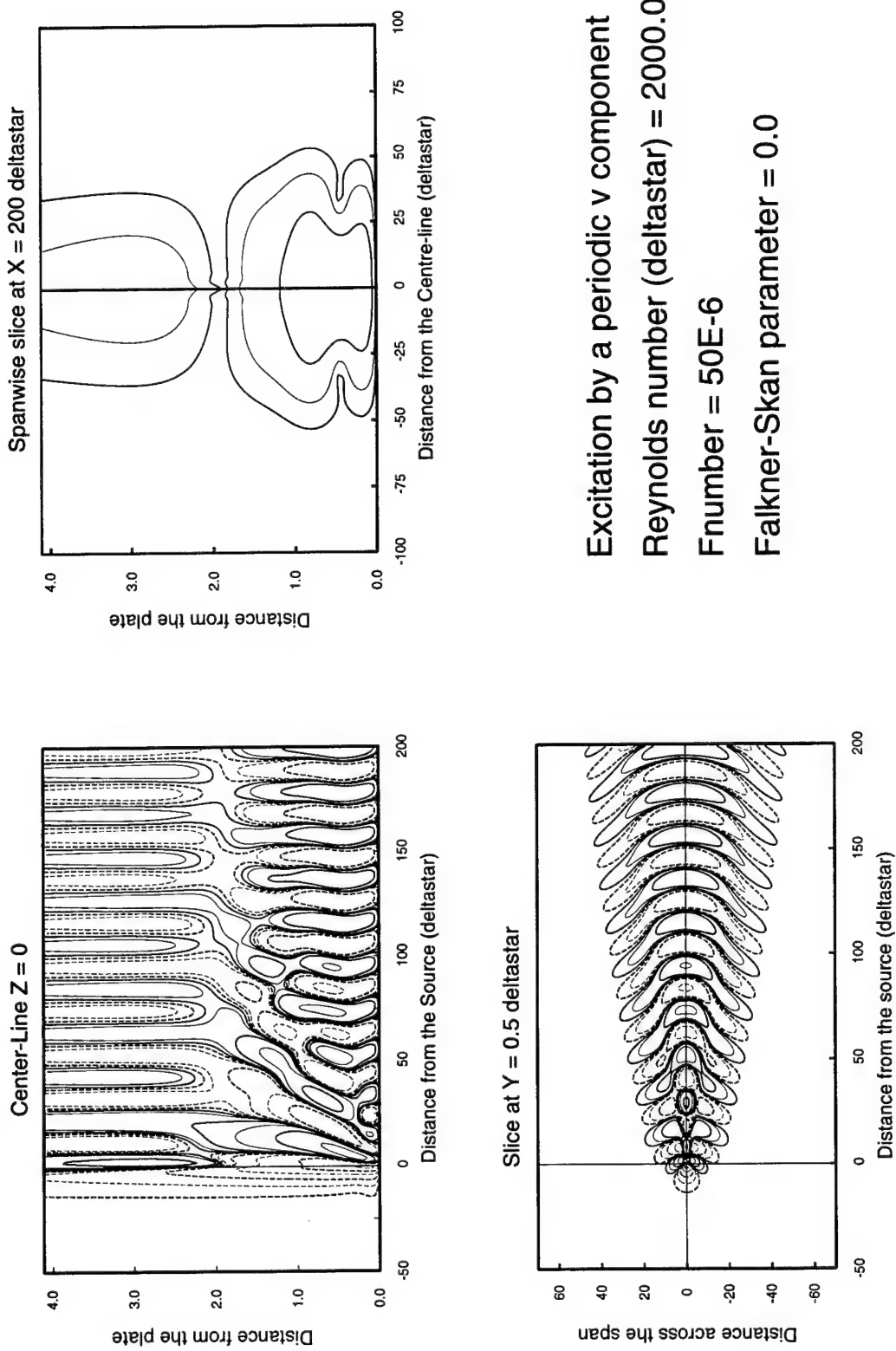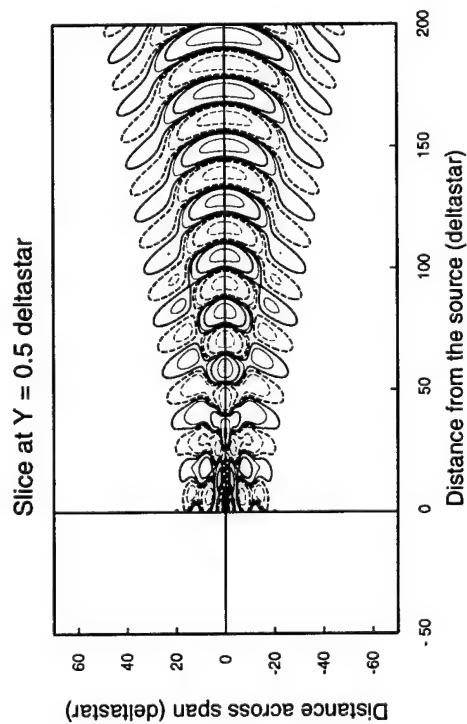Spanwise slice at X = 200 deltastar

Center-Line Z = 0

Slice at Y = 0.5 deltastar

Excitation by a periodic v component
Reynolds number (deltastar) = 2000.0
Fnumber = 50E-6
Falkner-Skan parameter = 0.0

Figure 3.4(v) Influence of Reynolds number

95

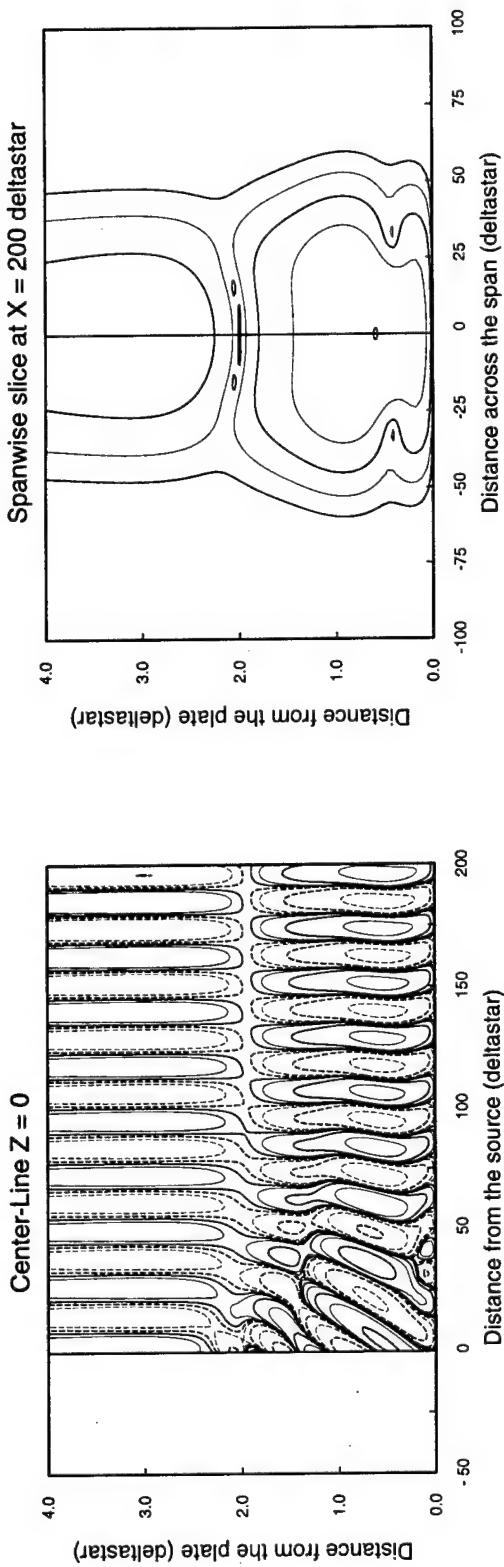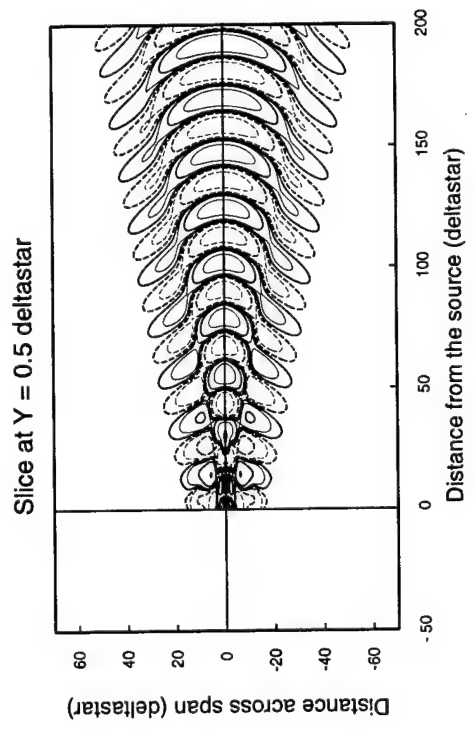Spanwise slice at X = 200 deltastar

Distance from the plate (deltastar)

Distance across the span (deltastar)

Excitation by a periodic u component

Reynolds number (deltastar) = 1000.0

Fnumber = 100E-6

Falkner-Skan parameter = 0.0

Lowest Contour = 0.001

Center-Line Z = 0

Distance from the plate (deltastar)

Distance from the source (deltastar)

Slice at Y = 0.5 deltastar

Distance across span (deltastar)

Distance from the source (deltastar)

Figure 4.0(i) Asymptotic Behaviour of the u Component
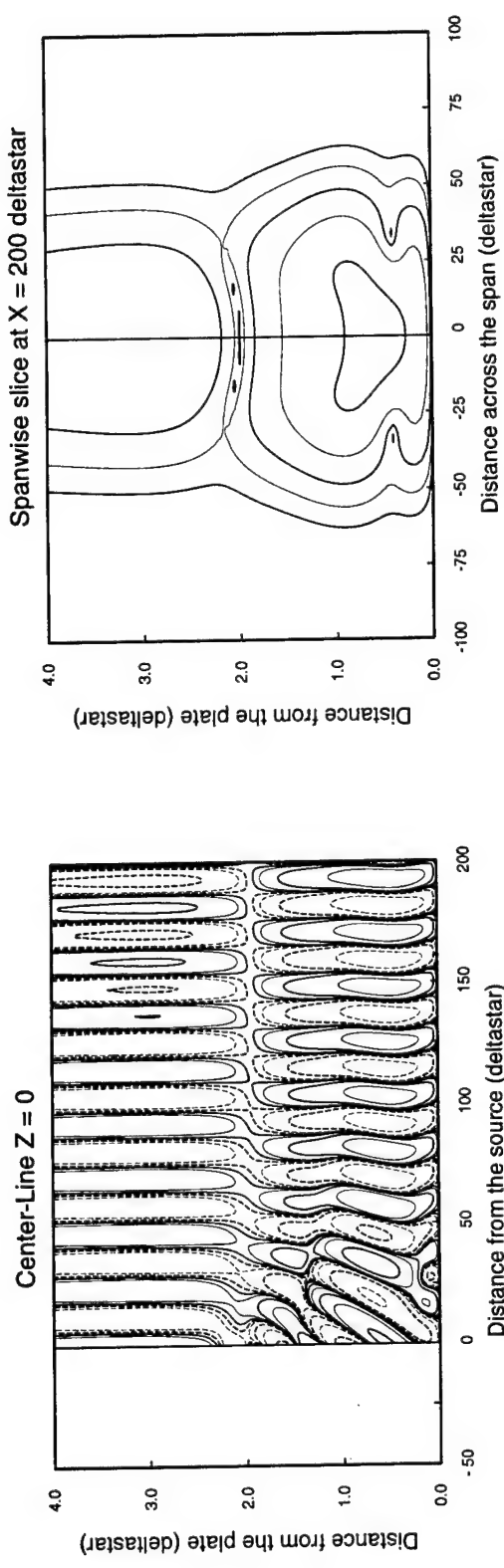
Spanwise slice at X = 200 deltastar

Distance across the span (deltastar)

Distance from the plate (deltastar)

Center-Line Z = 0

Distance from source (deltastar)

Distance from the plate (deltastar)

Slice at Y = 0.5 deltastar

Distance from the source (deltastar)

Distance across span (deltastar)

Excitation by a periodic v component

Reynolds number (deltastar) = 1000.0

Fnumber = 100E-6

Falkner-Skan parameter = 0.0

Lowest Contour = 0.001

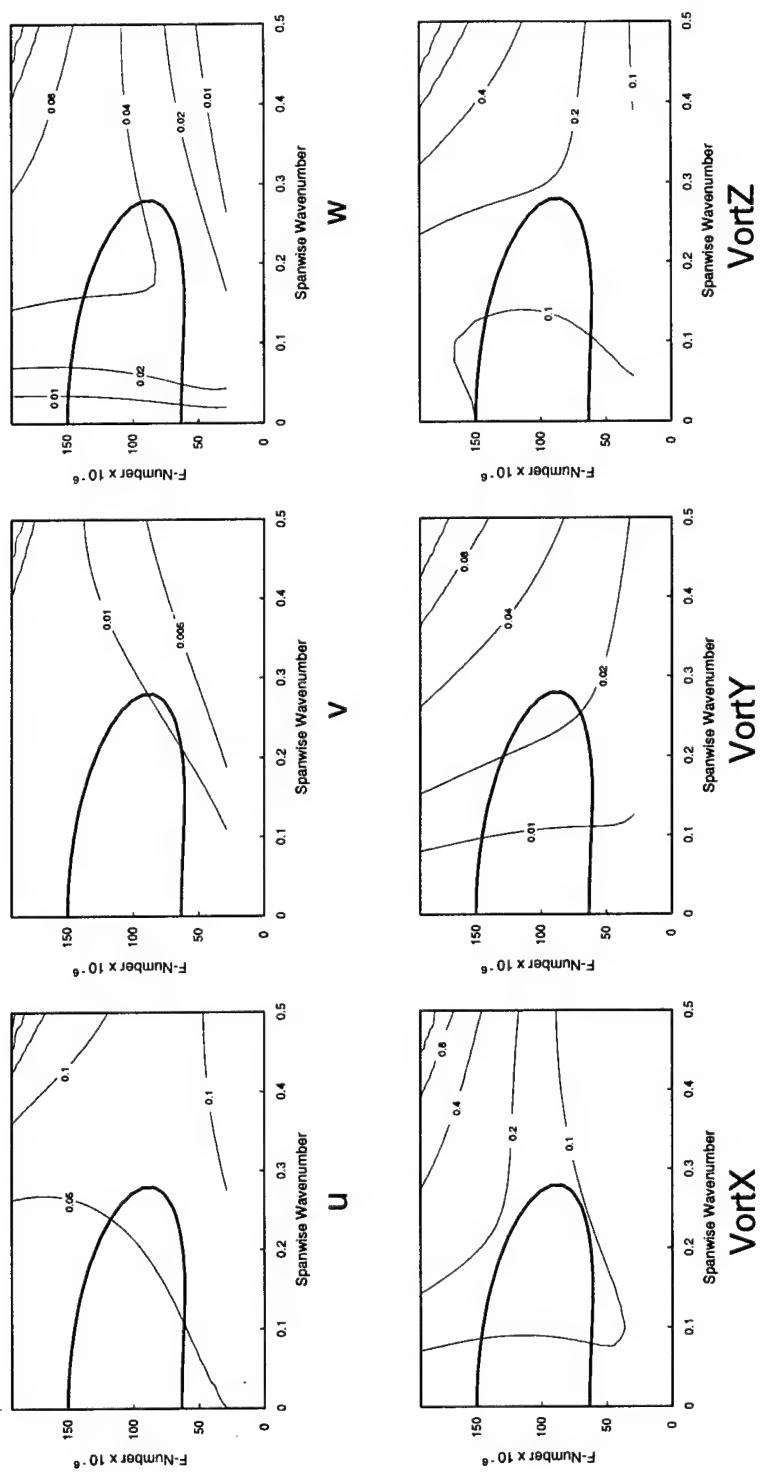Figure 4.0(ii) Asymptotic Response to a v Excitation
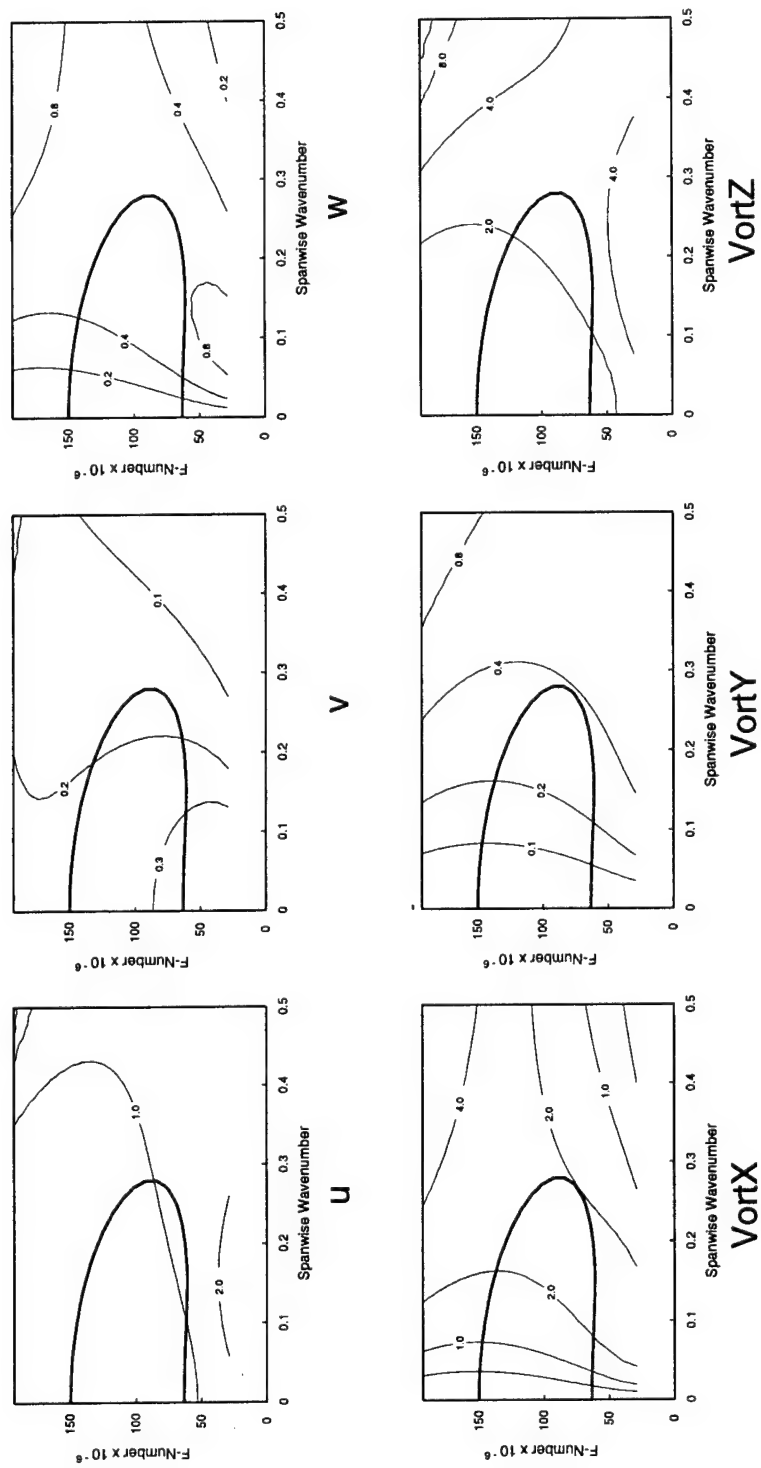
97

Figure 5.0(i) Receptivity to u excitation
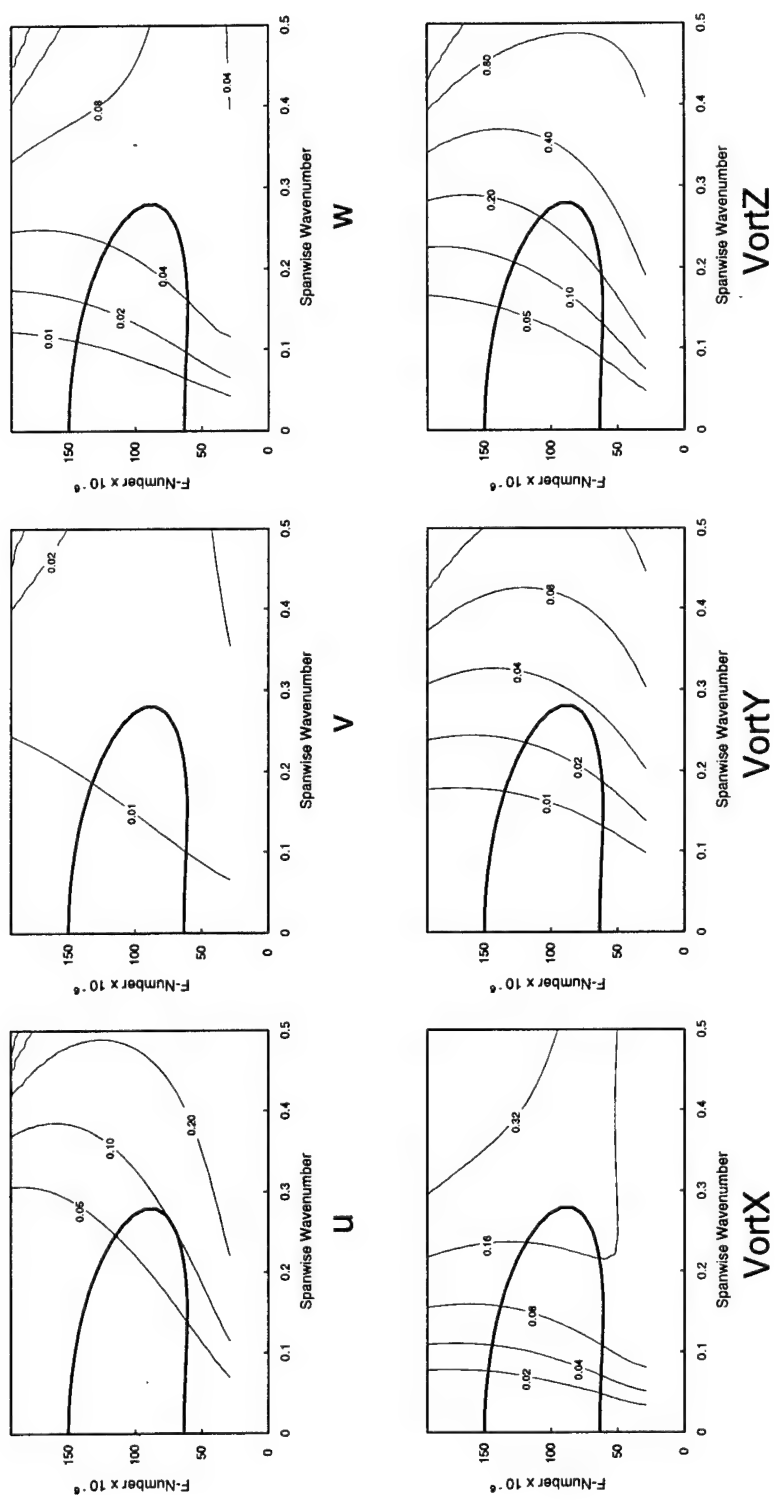
98

Figure 5.0(ii) Receptivity to v excitation
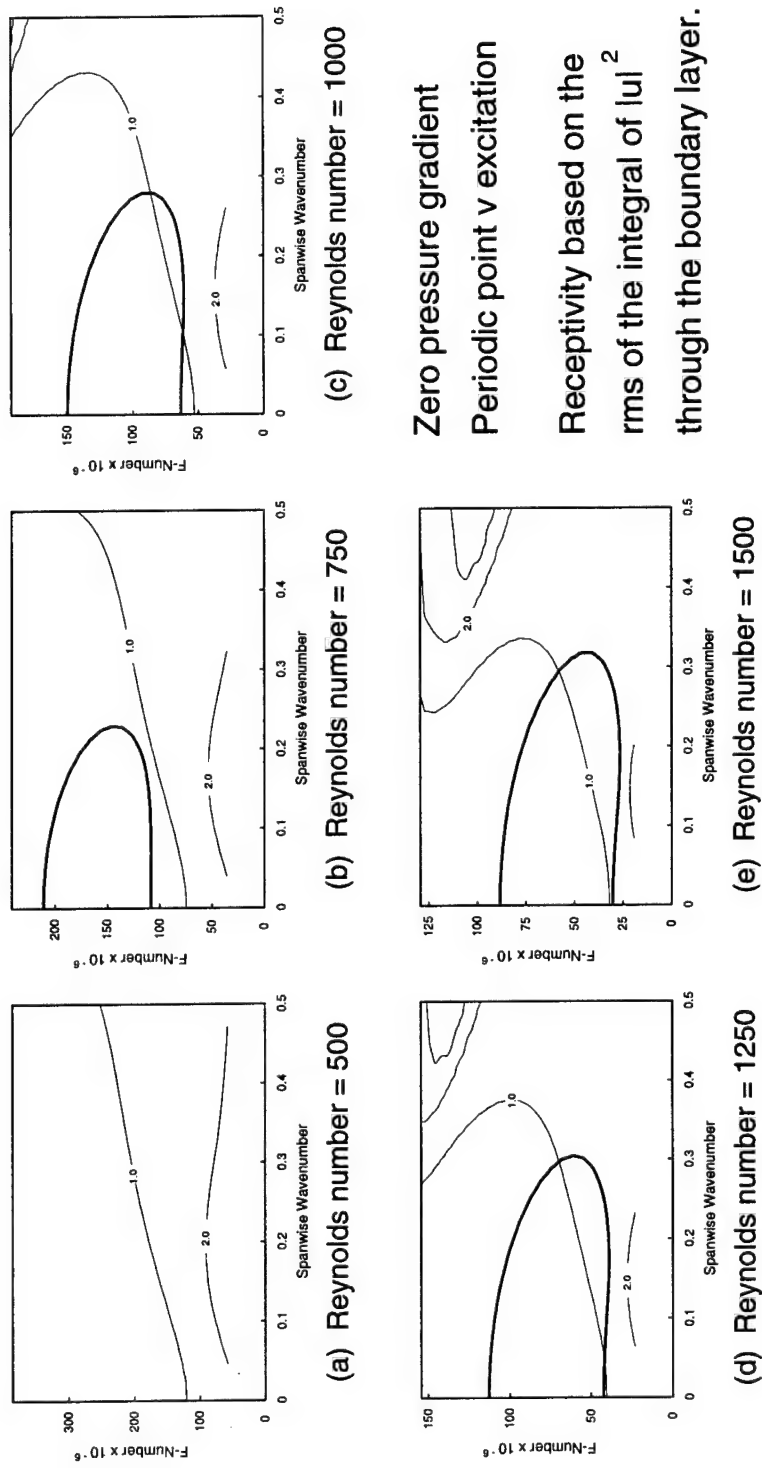
99

Figure 5.0(iii) Receptivity to w excitation

(a) Reynolds number = 500

(b) Reynolds number = 750

(c) Reynolds number = 1000

(d) Reynolds number = 1250

(e) Reynolds number = 1500

Zero pressure gradient
Periodic point v excitation

Receptivity based on the
rms of the integral of $|u|^2$
through the boundary layer.

Figure 5.2 Influence of Reynolds Number on Receptivity

(a) $\beta = 0.1$

(b) $\beta = 0.05$

(c) $\beta = 0.0$

(d) $\beta = -0.05$

(e) $\beta = -0.1$

Reynolds number = 1000.0
Periodic point v excitation

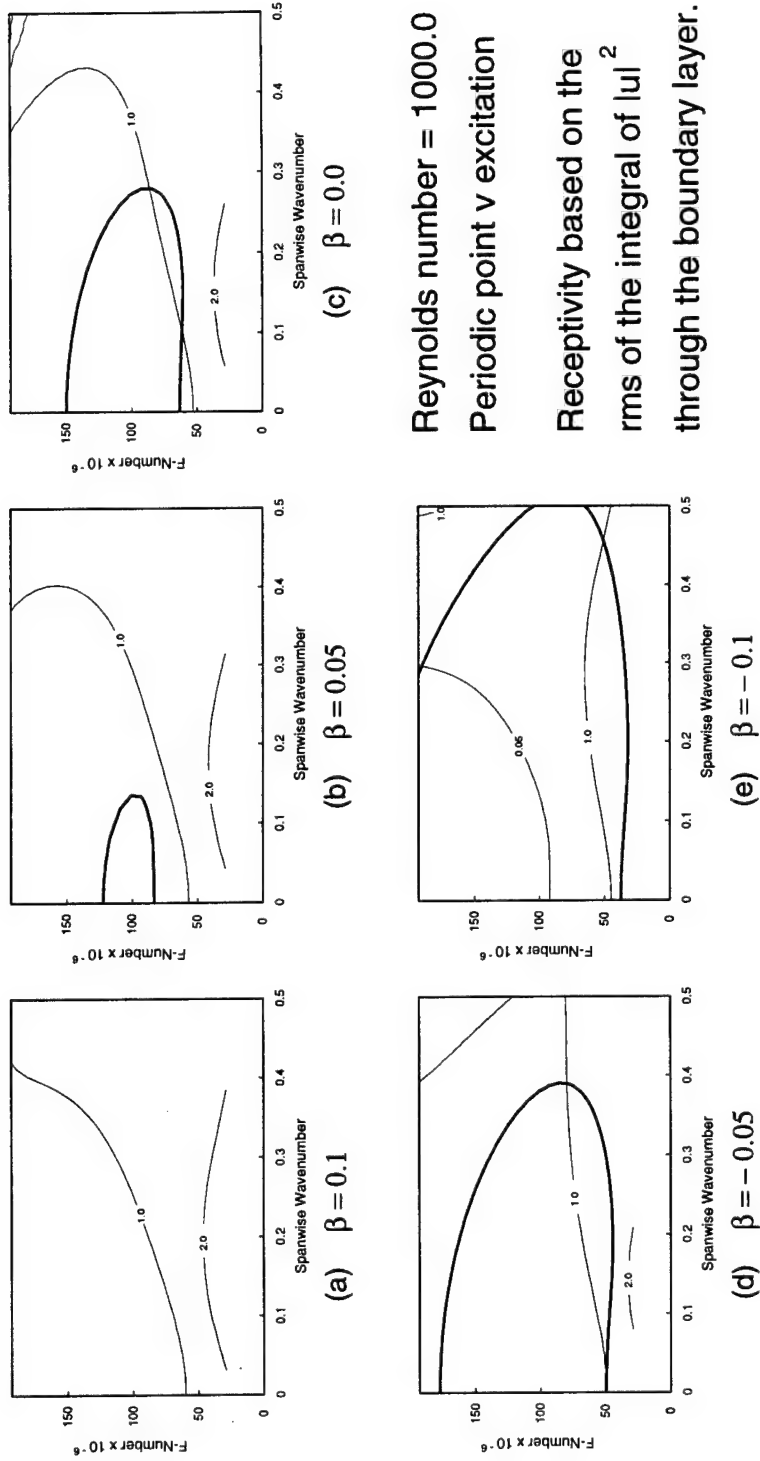Receptivity based on the
rms of the integral of $|u|^2$
through the boundary layer.

Figure 5.3 Influence of Pressure Gradient on Receptivity

v excitation

u excitation

Combined excitation

Excitation by a periodic bump of area deltastar squared and height deltastar/100 at 200 deltastar downstream

Reynolds number (deltastar) = 1000.0

Fnumber = 25E-6

Falkner-Skan parameter = 0.0
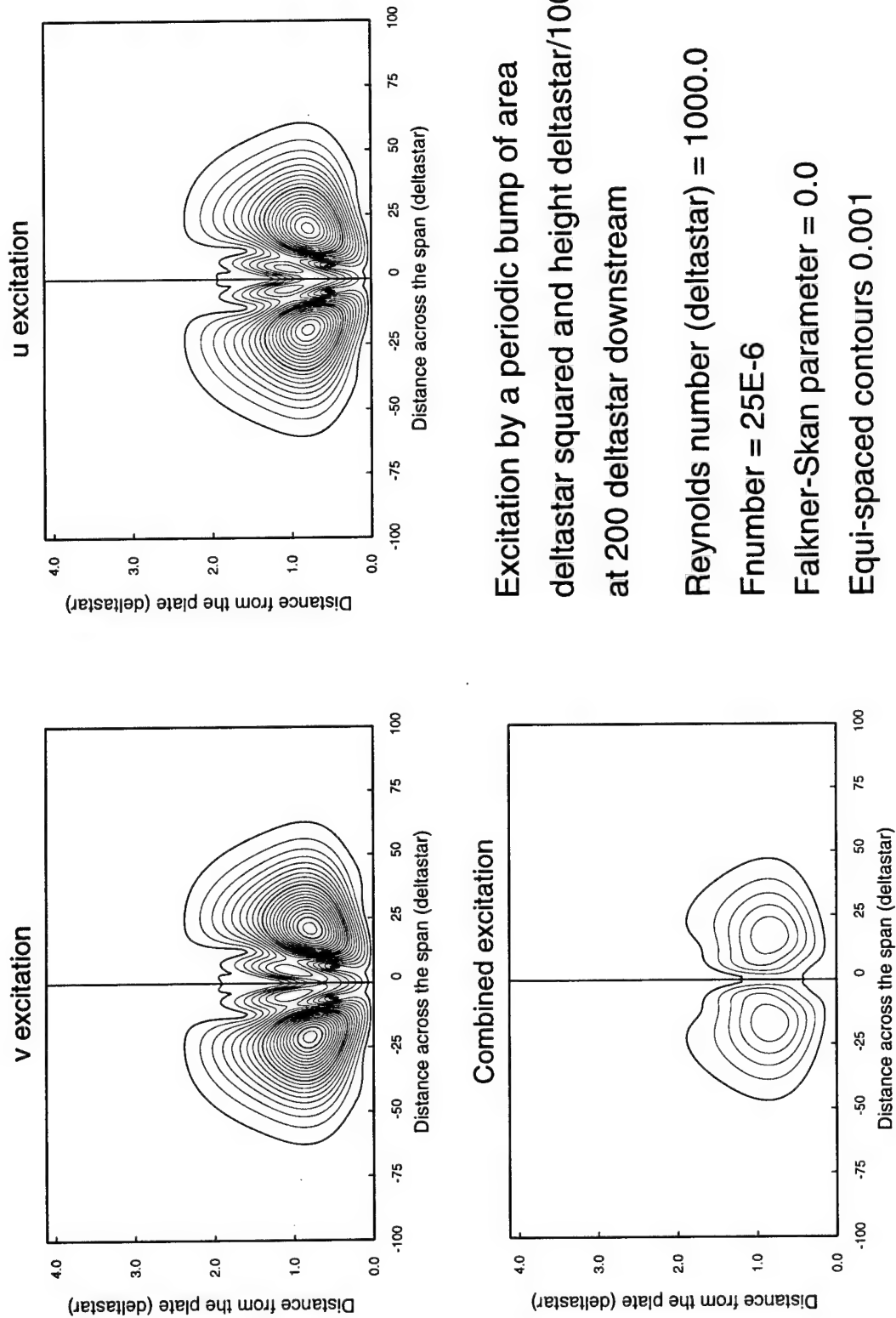
Equi-spaced contours 0.001

Figure 6.0 Asymptotic form of |u| from a Periodic Bump

103
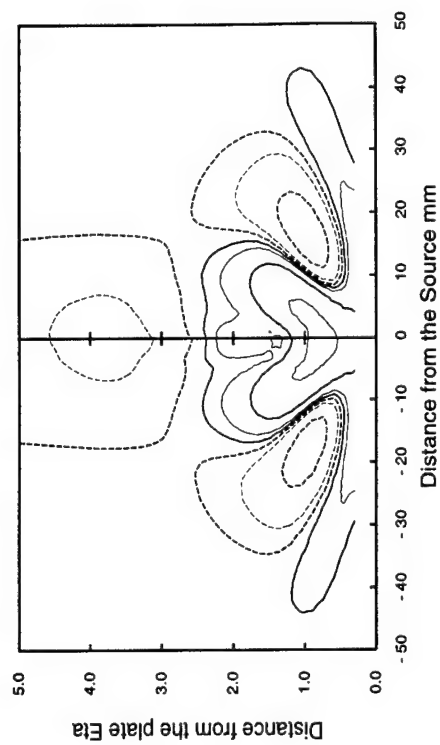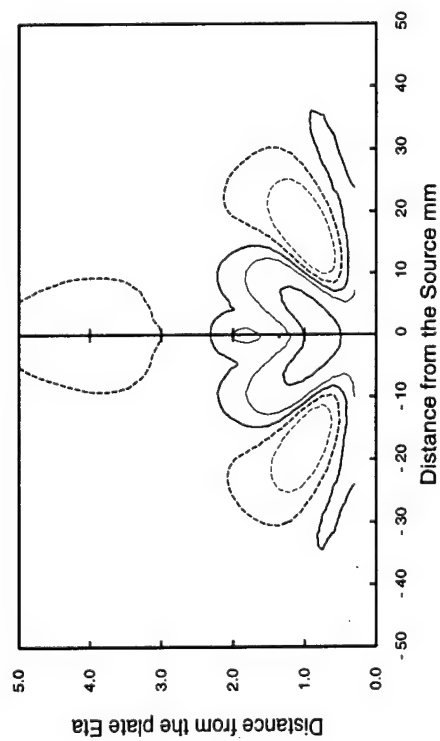
Jet velocity 0.27 m/s

Jet velocity 0.10 m/s

Jet velocity 0.93 m/s
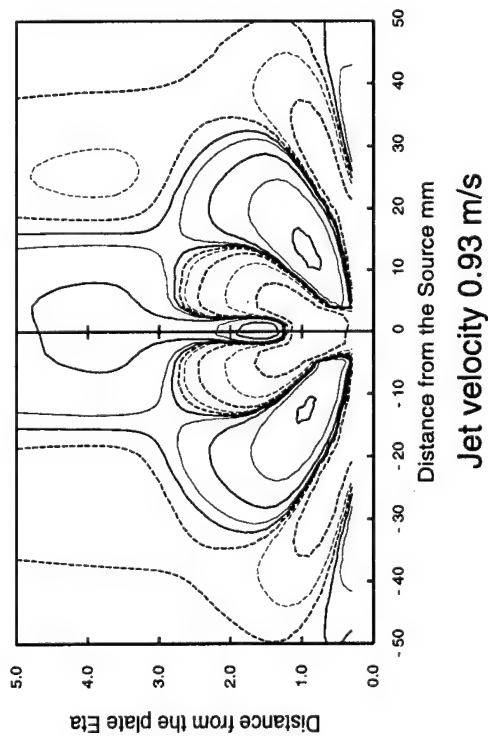
Excitation frequency = 96Hz

Jet diameter = 2mm

Free-Stream velocity = 10.0m/s

Spanwise traverse 100mm downstream

Lowest contour 0.001% Uinf

Figure 7.0.1   Effect of Jet Amplitude

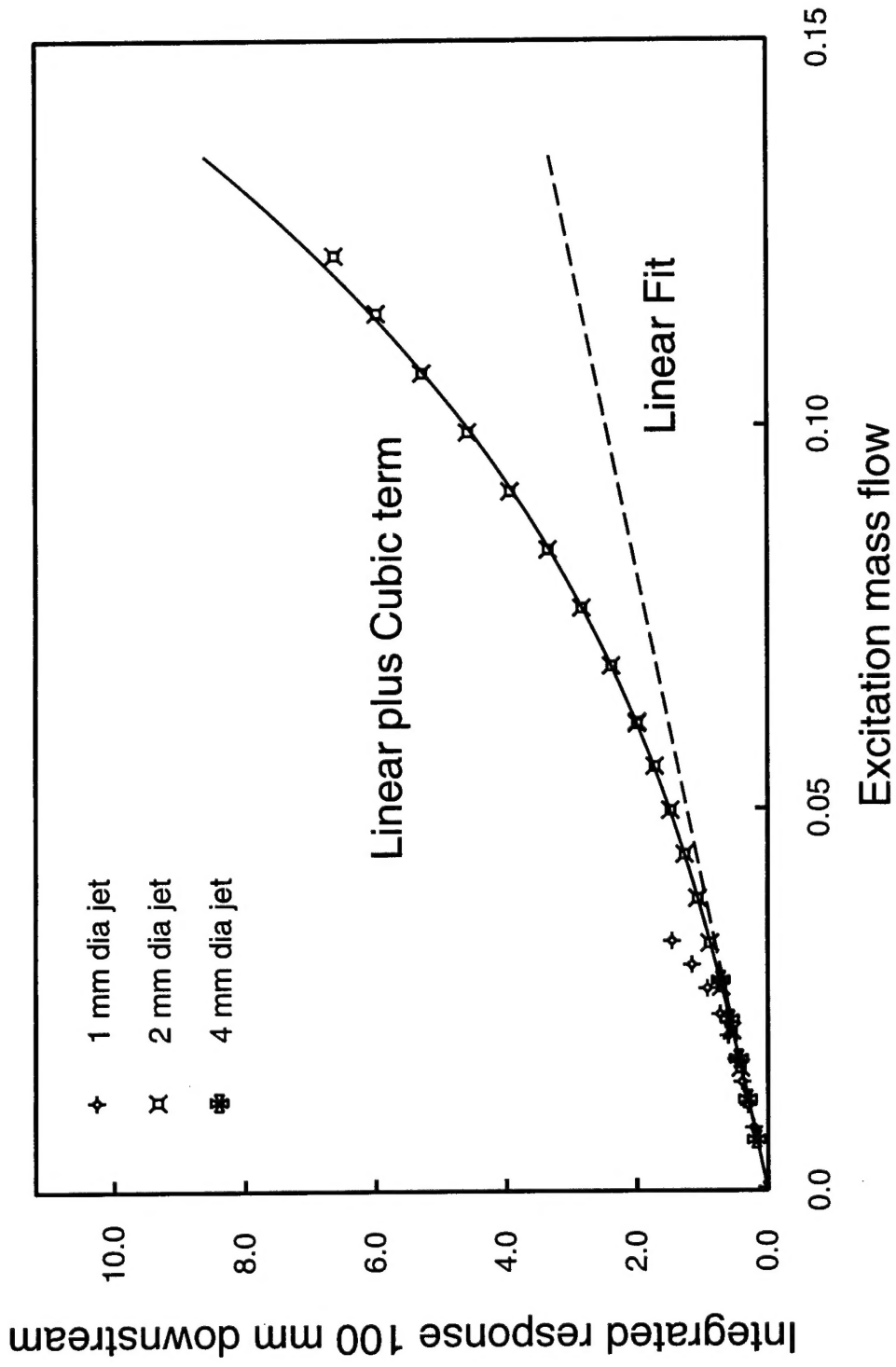Fundamental RMS u perturbation integrated over a spanwise plane

Fig 7.0.2 Influence of Excitation Level

Fig 7.0.3   Influence of Excitation Level

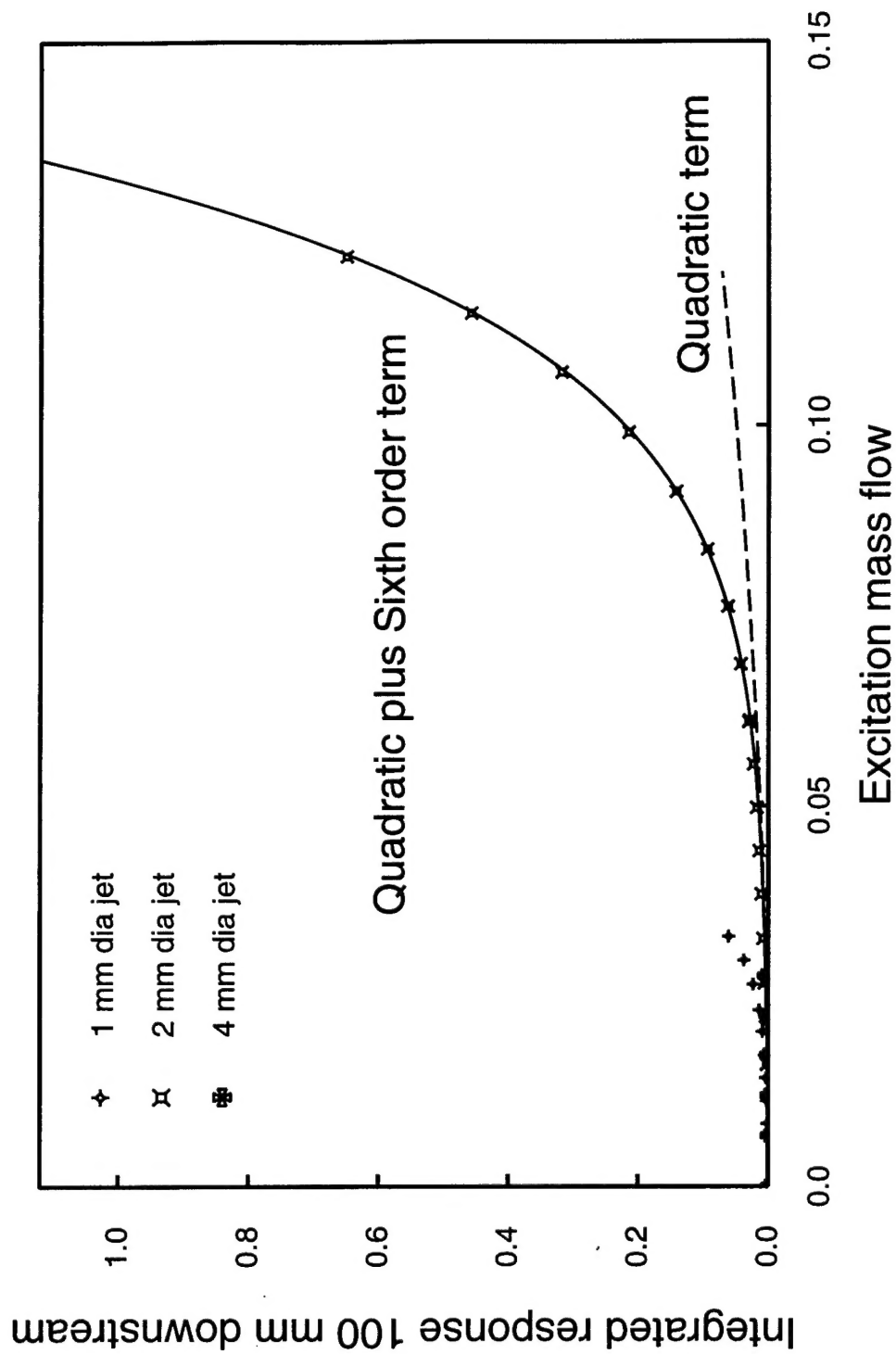First Harmonic RMS u perturbation integrated over a spanwise plane

Integrated response 100 mm downstream

Excitation mass flow

+   1 mm dia jet
¤   2 mm dia jet
✳   4 mm dia jet

Quadratic plus Sixth order term

Quadratic term

12   References

References

CARLSON, H.A., AND LUMLEY, J.L., 1996. Flow over an Obstacle Emerging from the Wall of a Channel. *AIAA Journal* Vol **34**, No. 5, 924–931.

CARLSON, H.A., BERKOOZ, G., AND LUMLEY, J.L., 1995. Direct Numerical Simulation of Flow in a Channel with Complex, Time-Dependent Wall Geometries: A Pseudospectral Method. *Journal of Computational Physics* Vol **121**, 155–175.

DANABASOGLU, G., BIRINGEN, S., AND STREETT, C.L., 1991. Spatial simulation of instability control by periodic suction blowing. *Physics of Fluids A* Vol **3**, No. 9, 2138–2147.

GOLDSTEIN, D., HANDLER, R., AND SIROVICH, L., 1993. Modeling a no-slip flow boundary with an external force field. *Journal of Computational Physics* **105**, 354–366.

LELE, S.K., 1992. Compact Finite Difference Schemes with Spectral-like Resolution. *Journal of Computational Physics* **103**, 16–42.

MACK, L.M., 1984. Boundary-layer linear stability theory. *AGARD Report No. 709*, "Special Course on Stability and Transition of Laminar Flows".

Meitz, H.L. and Fasel, H.F., "A Compact-Difference Scheme for the Navier-Stokes Equations in Vorticity-Velocity Formulation", Journal of Computational Physics, vol. 157, pp. 371-403, 2000

SCHLICHTING,H., 1987. Boundary Layer Theory, 7th edition. New York: McGraw-Hill, Inc.

SCHUBAUER, G.B., AND SKRAMSTAD, H.K., 1943. Laminar-boundary-layer oscillations and transition on a flat plate. *NACA Advanced Confidential Report*.

VIECELLI, J. A., 1969. A method for including arbitrary external boundaries in the MAC incompressible fluid computing technique. *Journal of Computational Physics* **4**, 543–551.

VIECELLI, J. A., 1971. A computing method for incompressible flows bounded by moving walls. *Journal of Computational Physics* **8**, 119–143.

von Terzi, D.A., Linnick, M.N., Seidel, J., and Fasel, H.F., 2001. Immersed Boundary Techniques for High-Order Finite-Difference Methods *AIAA Paper 2001-2918*, June 2001.

WYGNANSKI, I., 1997 Boundary layer and flow control by periodic addition of momentum. *AIAA*, paper 97-2117.